UNIVERSITY OF SOUTHAMPTON

FACULTY OF PHYSICAL AND APPLIED SCIENCES

Physics

Ultrafast Mode-locked Semiconductor Disk Lasers for Frequency Domain Measurement Systems

by

Theo Chen Sverre

Thesis for the degree of Doctor of Philosophy

June 2017

UNIVERSITY OF SOUTHAMPTON

ABSTRACT

FACULTY OF PHYSICAL AND APPLIED SCIENCES
Physics

Doctor of Philosophy

ULTRAFAST MODE-LOCKED SEMICONDUCTOR DISK LASERS FOR FREQUENCY DOMAIN MEASUREMENT SYSTEMS

by Theo Chen Sverre

Ultrafast pulses can now be generated in mode-locked vertical external-cavity surface-emitting lasers (ML-VECSELs) at high powers and GHz repetition rates. This laser platform has also demonstrated the addition of intracavity elements and flexibility of cavity geometries. In this thesis, we report the demonstration of two versions of repetition rate tunable VECSELs. The first, produced 215-fs pulse trains of up to 20 mW for a continuously tunable repetition rate between 0.880-1.880 GHz, directly emitted by the VECSEL. The second, produced 300-fs pulses at average powers of 50 mW, and able to tune the pulse repetition rate from 0.960-1.720 GHz. These VECSELs pave the way to performing frequency domain analysis in the GHz by resonantly exciting a sample under study. Here we have designed time-domain and frequency-domain experiments to characterise the acoustic behaviour of mechanically responsive nanostructures. The VECSEL also provides a stable platform for fs pulse generation, with a high Q-factor cavity making it possible to harness the large intracavity power. In this thesis we describe the first demonstration of a semiconductor saturable absorbing mirror (SESAM) coated with a patterned mask addition of an intracavity photoconductive antenna (PCA).

Contents

List of Figures

List of Tables

Declaration of Authorship

I, Theo Chen Sverre, declare that the thesis entitled *Ultrafast Mode-locked Semiconductor Disk Lasers for Frequency Domain Measurement Systems* and the work presented in the thesis are both my own, and have been generated by me as the result of my own original research. I confirm that:

- this work was done wholly or mainly while in candidature for a research degree at this University;
- where any part of this thesis has previously been submitted for a degree or any other qualification at this University or any other institution, this has been clearly stated;
- where I have consulted the published work of others, this is always clearly attributed;
- where I have quoted from the work of others, the source is always given. With the exception of such quotations, this thesis is entirely my own work;
- I have acknowledged all main sources of help;
- where the thesis is based on work done by myself jointly with others, I have made clear exactly what was done by others and what I have contributed myself;
- parts of this work have been published as: Chen Sverre, T. *et al.* Proc. SPIE (2016), Chen Sverre, T. *et al.* Proc. SPIE (2017)

Signed:.....

Date:.....

Acknowledgements

First of all I would like to thank my supervisors, Otto Muskens and Anne Tropper, you have both provided unparalleled support to my PhD research. Many thanks to past and present group members I have had the pleasure of spending my time as a post graduate student. In particular, the members of the VECSEL group. First, Robin Head, as the long suffering post-doc for most of my time in VECSELs you have provided superb advice. Andy Turnbull, you are responsible for how terrifying I am as a demonstrator, telling me to go home when I'm ill and going above and beyond to help me. Jonathan Woods, though a recent addition to the VECSEL group I must thank you for making labwork an absolute delight. Ed Shaw and Ollie Morris, thank you for your expertise and providing a VECSELent atmosphere both in our office and while we were away on conferences.

Thanks to all of the researchers I collaborated with over my postgraduate studies. In particular, those who provided our excellent VECSEL structures, Dr Ian Farrer, Dr Harvey Beere and Alex Hein, and special thanks to Oleksandr Buchnev and Bruce Ou for fabricating the nanostructures and providing me with vacuum components to analyse them. I must also thank the department technical staff for their support, from borrowing to building components essential to my research.

Thanks you all of my friends, in my department and otherwise, you have all been sources of teas, coffees, late nights, advice and friendship.

To my family, I am ever grateful for everything you have done over my undergraduate and PhD life to make sure I stay sane.

Finally, to Jo and Ping who have put up with me through the final stages of my PhD, without you there the prospect of finishing my PhD would have been much more daunting and gruelling one, and was made much easier with you there.

To you all, thank you.

Nomenclature

VECSEL	Vertical External-Cavity Semiconductor Laser
SESAM	Semiconductor Saturable Absorbing Mirror
ML	Mode-locked
CW	Continuous wave
f_{Rep}	Pulse repetition frequency
λ	Wavelength
λ_{FWHM}	Wavelength full-width-half-maximum
P_{avg}	Average Power
τ_{FWHM}	Pulse duration full-width-half-maximum
ΔR	Modulation depth
F_{sat}	Saturation fluence
L_{nonsat}	Non-saturable losses
τ_{slow}	Slow decay constant
τ_{gain}	Fast decay constant
M_i	Ray matrix of cavity element i
$F_{satgain}$	Saturable gain fluence
AR	Anti-resonant
CVD	Chemical vapor deposition
DBR	Distributed Bragg reflector
V628	1-μm gain structure
V629	1-μm SESAM
H29	1035-nm gain structure
V623	1035-nm SESAM

Chapter 1

Introduction

Regularly spaced optical pulses of around 100 fs duration can be generated by a variety of ultrafast laser sources (Fermann et al. (2005)). These sources have enabled important new techniques in technology and science, including materials processing, biomedical applications, optical communications, microwave photonics and metrology (Keller (2010)). Commercial ultrafast lasers offer turn-key operation, directly emitting reliable sub-300-fs pulse trains with pulse energies up to many nJ. Glass fibre or titanium-doped sapphire (Ti:Sapphire) lasers are restricted to direct emission around three spectral regions: 850 nm, $1\mu m$ and 1.55 μm, though this may be extended with the use of OPOs. In addition, they typically operate at a fixed repetition frequency around 100 MHz corresponding to a laser cavity more than a metre in length. The repetition frequency may also be reduced to a sub-harmonic, step-wise, by using a pulse-picker. Finally, these laser cavities are typically designed with sensitivity to alignment.

The limitations of conventional systems motivated the development of an all-semiconductor alternative, the Mode Locked Vertical External Cavity Surface Emitting Laser (ML-VECSEL) (Keller and Tropper (2006)). The VECSEL is an external-cavity semiconductor disk laser (SDL) which is usually pumped optically, The semiconductor microcavity contains several quantum wells (QWs) engineered by selectively growing with different materials and arranged at specific points in the microcavity to provide gain. Futhermore, the emission wavelength can be tuned by selection of QW materials and spacing. Fine-tuned semiconductor design allows the VECSEL to combine the large active area,

good beam quality and power scaling capability of a diode-pumped solid state laser with the bandwidth engineering potential of a semiconductor laser. VECSELs readily exhibit passive mode-locking, usually by means of a semiconductor saturable absorber mirror (SESAM) used as an optical element in the external cavity.

SESAM ML-VECSELs have passed a number of key milestones for ultrafast laser performance, including multi-watt average power (Heinen et al. (2012)), peak power exceeding 1 kW (Scheller et al. (2012), Head et al. (2016)) and sub-200-fs pulse formation (Klopp et al. (2011), Waldburger et al. (2016), Head et al. (2016)). The carrier lifetime and saturation fluence of the surface emitting semiconductor gain-structure are consistent with pulse repetition frequencies in mode-locked operation in the range ≈ 500 MHz - 50 GHz, corresponding to cavity lengths in the range 30 cm - 3 mm. In this respect they are quite unlike mode-locked solid state lasers, which typically operate at 80 -100 MHz, corresponding to 1.8 - 1.5 m. Moreover, it has been shown that it is possible to tune the cavity length, and the pulse repetition frequency continuously over a broad range without losing the mode-locking of a ML-VECSEL: sub-500 fs 8% near 1 GHz Wilcox and Quarterman (2011), 2.78-7.87 GHz (with two pulsed regimes: ≈450 fs and ≈2.5 ps separated at 6 GHz) Wilcox et al. (2011) and ≈625 fs 6.5-11.3 GHz Sieber et al. (2011).

The aim of this thesis was to explore the application of ML-VECSELs for novel spectroscopic measurements which could benefit from the GHz repetition frequencies and in particular from the tuning capability. To this end, the thesis was divided into three major areas. First Chapter.2 describes the development of a stable and high power, close-to-100-fs ML-VECSEL with continuous repetition frequency tuning around a GHz. Next Chapters 3, 4 and 5 concentrate on applying this VECSEL to the excitation of suitable nanostructures. Finally, Chapter.6 reports the development of an intracavity element for direct pulsed-THz generation.

1.1 VECSELs

VECSELs, otherwise known as optically-pumped external-cavity Semiconductor Disc Lasers (SDLs), are semiconductor based lasers based on micro-structured semiconductor

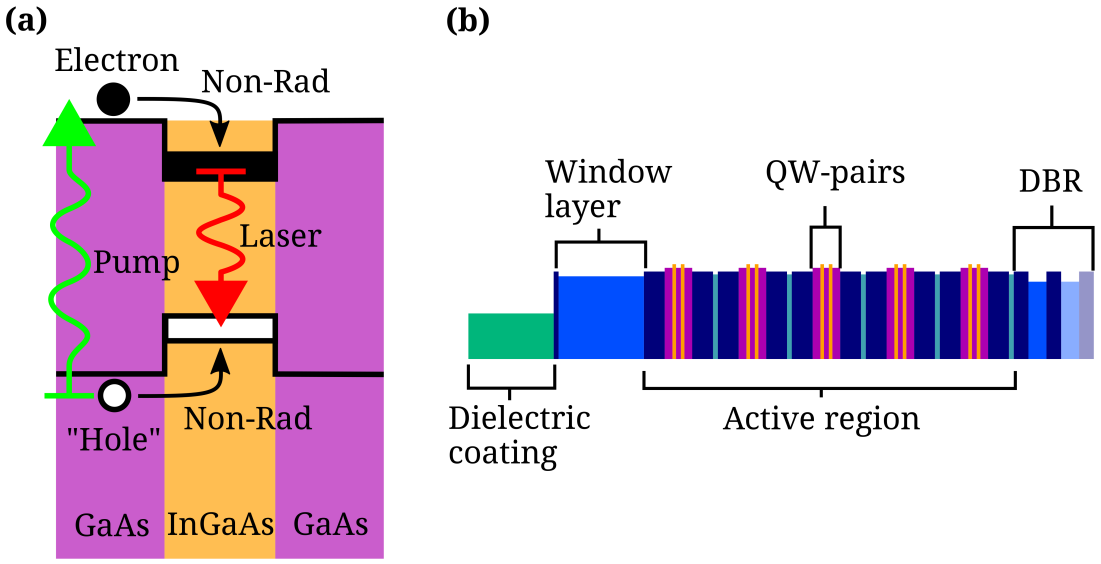

Figure 1.1: *(a) A schematic diagram of the pumping and lasing scheme in a QW VECSEL. Electron-hole pairs are generated in the GaAs barriers by incident pump radiation at 808 nm. The carriers non-radiatively decay to the InGaAs and lase at 1 μm - 1035 nm. (b) A schematic diagram of the VECSEL gain-structure (based on the 1035 nm gain-structure in Fig.2.3(a)), (above) showing the dielectric coating, window layer, active region approximately 1 μm thick, and the first 2.5 pairs of 27 DBR pairs.*

epilayers with QW or quantum dot (QD) active regions. Both optical pumping and epilayer design provide the VECSEL with properties unseen in other lasers.

The advantage of optical pumping is that it avoids the problems incurred in electrical pumping. It is easy to achieve uniform excitation across a large area laser mode, it avoids current filamentation, and the structure can be insulating since it does not need a p-type distributed Bragg reflector (DBR), with lower reflectivity and free carrier losses. The optical pump may also be focused to a desired spot-size or shape, to match the laser mode on the gain, meaning that larger mode areas may be used to increase the damage threshold and increase the operational output power. Large mode area on the gain may increase the likelihood of high-order mode lasing, but the external cavity imposes a TEM_{00} mode even for a large gain spot. The external cavity also allows the inclusion of intracavity elements such as etalons, birefringent filters, nonlinear crystals and, for mode-locking, saturable absorbers.

The essential features of the epilayer design of QW VECSEL gain-structures are displayed in Fig.1.1. Fig.1.1(a) shows the band structure in the VECSEL QW gain-structure in the 1-μm regime. The QW is formed by incorporating In into the GaAs. Electron-hole pairs are excited by pump radiation in the GaAs barrier layers either side of the QW layer. The carriers non-radiatively decay to the QW where they may radiatively decay. The remaining material in the active region is used to ensure that carriers decay into the QWs only, in addition a window layer separates the topmost QW from the surface stopping surface recombination. As shown in Fig.1.1(a) QWs are spaced throughout the microcavity active region. The spacing can be varied to tune the E-field enhancement at specific wavelengths.

1.1.1 Mode-locking

Mode-locking is a technique used to generate very short pulses of light consisting of, in the frequency-domain, imposing a fixed-phase relationship to axial resonator modes. As long as a high number of modes can be locked in phase to each other then the laser cavity will emit a pulse train at a frequency corresponding to the cavity round-trip. Phase synchronous operation is achieved by imposing a gain or loss modulation at the round-trip frequency. Depending on the way in which modulation of the gain or loss is introduced to the laser cavity, mode-locking mechanisms are classified as either active or passive.

Active mode-locking can be produced by actively modulating the gain. This type of mode-locking is present in some electrically-pumped semiconductor lasers, where the electrical driving current can be modulated. Another mechanism for active mode-locking is loss modulation, which may be achieved with fast loss-modulation using an Acousto-Optic Modulator (AOM) or an Electro-Optic Modulator (EOM). For both cases, the gain or loss must be modulated at a cavity frequency for stable mode-locking, which may require complex electronics to produce a stable modulation source. Pulse formation and shaping in an actively mode-locked laser is typically limited to ps pulse durations due to the slow rate of change of the net gain.

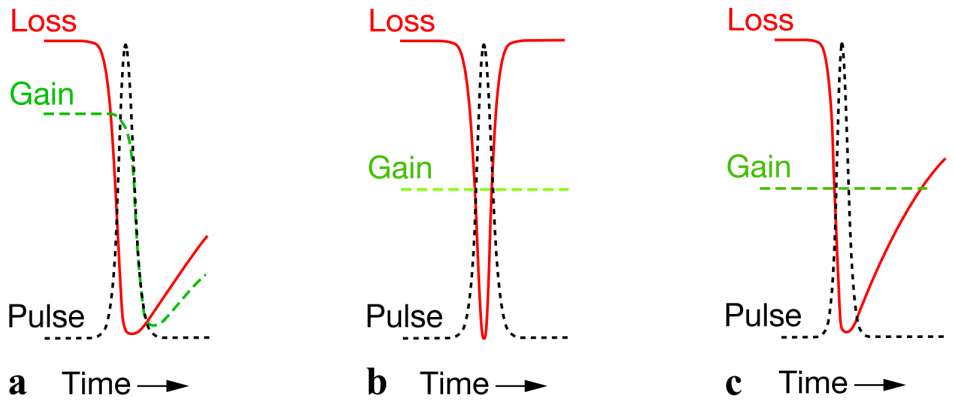

Figure 1.2: *Diagrams for gain and loss changes in passive mode-locking for (a) slow saturable absorber and gain saturation (ML-VECSEL with a SESAM); (b) fast saturable absorber (KLM) (c) slow saturable absorber without gain saturation. Figure from Keller (2010).*

Passive mode-locking relies on an intracavity element which provides intensity-dependent loss. In the time-domain, the pulse produces a net-gain window, into which the light circulating in the cavity is localised. Passive mode-locking can produce a net gain window much shorter than can be achieved with active mode-locking. Passive mode-locking is also subdivided into two categories based on the modulation-element: fast saturable-absorber and slow saturable-absorber.

Fast saturable absorption is most commonly applied using Kerr Lens Mode-Locking (KLM), typically in ML Ti:Sapphire lasers. Kerr lensing is an effect displayed by some materials where $\chi^{(3)}$ refractive index changes can be induced under high enough optical intensities. Intensity dependent refractive index can be used to self-focus the intracavity mode and, in conjuction with an intracavity iris, high intensities will see less loss in the laser cavity, promoting pulsed operation. KLM Ti:Sapphire lasers have achieved pulses down to 5-fs duration (Steinmeyer et al. (1999)). The key advantage of fast saturable-absorber mode-locking is that the net gain window may be as short as the pulse itself, enabling much shorter pulses than active mode-locking, it also self-centres the pulse in the cavity resulting in low noise outside the pulse. The disadvantage of KLM-Ti:Sapphire lasers is that the cavity must operate very close to the limit on cavity stability, causing low flexibility in the design.

Slow saturable-absorbers most frequently take the form of SESAMs. These structures

are typically composed of: a Distributed Bragg Reflector (DBR) engineered for the design wavelength, and an absorber layer, which is QW or QD based. The SESAM design, materials and thickness, are used to control the chromatic dispersion, bandwidth, modulation depth, recombination time, among other factors that influence pulse formation and shaping; the SESAM can also be engineered to balance these factors introduced by the gain-structure. The recovery time of the SESAM occurs over ps timescales, mediated in high quality semiconductor by: photon emission and Auger recombination. Fast surface recombination SESAMs are grown at standard growth temperatures, with the absorbing well positioned a few nm below the air-surface interface. Recovery on a timescale of 10-ps occurs as carriers tunnel out of the QW to the air-surface interface where microscopic surface defects act as carrier traps. As shown in Fig.1.2(a) the gain saturation closes the net gain window reducing it to 100-fs scales. This differs from Fig.1.2(c), where the net gain window is approximately as long as the recovery time of the saturable absorber.

Fine tuning of the semiconductor structures can be readily applied to extend the gain bandwidth and control dispersion, making the VECSEL a suitable platform for ultrafast pulse generation. Furthermore, the most commonly applied mode-locking scheme is based on SESAMs, slow saturable absorber mode-locking is capable of producing 100-fs pulses without the laser cavity operating at the limit of stability, as in the case of KLM.

1.1.2 ML-VECSEL Design

In the ML-VECSELs presented in this thesis, pulse formation and mode-locking is induced passively by a GaAs-based surface-recombination SESAM. SESAMs, while originally designed for use with solid-state lasers, can also be used in VECSELs as long as the mode area ratio between the laser mode on the gain and SESAM are controlled as a function of the modulation depth (ΔR) and saturation fluence (F_{sat}) of the SESAM.

The mode-locking mechanism in ML-VECSELs used in this research is passive, with a slow saturable-absorber, where the leading edge of the pulse is shortened by the SESAM saturation and the trailing edge is shortened by the gain saturation. Dispersion in the laser cavity is comparatively small due to the thinness of the structures, but the

small amount is given by microcavity index changes of the gain and SESAM structures. As such dispersion management can be applied to the structures by adding dielectric coatings, which also contributes to suppressing the interaction of the QWs with the microcavity antinodes.

To achieve mode-locking with ultrafast pulses the VECSEL gain-structure must be able to support a large number of modes, which means being designed for broad gain-bandwidth. In addition, the structure must have a low GDD. Two types of gain-structure design optimised for mode-locking were used in this thesis, anti-resonant (AR) and "flip-chip" with Double Quantum-Wells (DQWs).

AR gain-structure designs were first described by Garnache et al. (2002). AR structures are characterised by a capping layer of $\approx \lambda/4$ thickness which displaces the standing wave so that a node is formed at the window/air interface for a design wavelength; this reduces the intensity of antinodes in the microcavity, typically to 1/10 at the design wavelength relative to a resonant sample. The reduction in intensity, causes it to peak either side of the design wavelength, broadening the gain bandwidth.

The "flip-chip" method, produces a gain-structure with enhanced thermal management Kuznetsov et al. (1999). Flip-chip fabrication method grows the structure epilayers starting from the window layer and ending after the DBR, leaving the GaAs substrate attached to the window layer. The substrate is then etched away, leaving a small amount $\approx$7 nm thick, which does not interfere with the microcavity. The resulting chip can then be attached to a Chemical Vapor Deposition (CVD) diamond heat-spreader of approximately 300 μm, in place of the GaAs substrate that would be present in a traditional growth structure. This extra-cavity diamond heat spreader increases the power handling of the VECSEL thanks to the increase in thermal conductivity of the material between the copper heatsink and the DBR. In a traditional sample there is $\approx$300 μm of GaAs between the DBR and the copper, thermal conductivity(at 300K)= 52 W/mK; whereas, for a "flip-chip" structure, this GaAs layer, is replaced by CVD diamond, thermal conductivity (at 300K)= 1800 W/mK. However, an intra-cavity diamond heat spreader would mean that the thermal extraction can be performed without being obstructed by the DBR, further enhancing the thermal management, but this case relies on high

optical quality anti-reflection coated diamond and adequate dispersion management to minimise the impact on intracavity pulses, and a wedged surface to eliminate etalon effects. An important new advancement is the demonstration of the Membrane External Cavity Semiconductor Laser (MECSEL) by Kahle et al. (2016) that SDL active regions can be lifted off the substrate and used as independent gain membranes, with great potential benefits for thermal management, power scaling, wavelength flexibility and broadband ultrafast operation.

Using the structures, the design feature of ML-VECSELs investigated in this thesis was the use of the external cavity for tuning the pulse train repetition frequency. As long as the cavity length of the VECSEL can change, the repetition frequency f_{Rep} will depend on the cavity round-trip length L_{cav} as shown in,

$$F_{rep} = \frac{c}{2nL_{cav}} \tag{1.1}$$

where c is the speed of light and n is the refractive index of the cavity. A repetition-rate based measurement requires continuous tuning of L_{cav}, making the VECSEL ideally suited to develop this measurement system, since a VECSEL may be built to maintain mode-locking conditions over a continuous range of cavity lengths.

Therefore, the aim of the project is to design a laser source that will excite a vibrational mode in a nanostructure with GHz resonances, by repeated small impacts, in phase, with the resonance under study. If the vibrational resonance is lightly damped, the amplitude of the vibration will grow over many cycles. The design challenges of producing this laser source stem from translating the output coupler (OC) mirror. Changing OC position causes changes to mode size on the gain-structure, which is potentially detrimental to the gain-mode/pump-spot overlap. The mode size on the SESAM also changes as the OC is translated. The changes in gain-mode and SESAM-mode result in area-ratio changes, and as the cavity length changes the pulse energy varies in proportion. Both these effects change the saturation conditions of the gain and SESAM, which may compromise mode-locked output. The process to identify a cavity design which could mitigate these effects it described in Sec.2.3.

In Chapter.2 the VECSEL design stages are described, including semiconductor structures and laser cavity design. Mode-locked VECSEL characterisations are also shown displaying the first sub-400-fs broadly repetition frequency tunable VECSEL.

1.2 Acoustic Nanostructures

Nanostructures have been of great interest to a large number of scientific disciplines due to their unusual properties. At this scale unexpected effects may arise from the size of the structures that differ from bulk interactions and effects. The large surface area and reduced size results in effects such as high electron-confinement, tunnelling and surface-enhanced absorption/emission. For dielectric nanostructures, scattering of light may be many times higher than of bulk material. For metallic nanostructures, surface oscillations of electrons mediate the observed effects from nanoscale structures, known as localised surface plasmons polaritons (LSPP).

LSPPs are formed by the oscillation of induced charges close to the surface of a material structure's lattice. The plasmonic response of a nanostructure depend strongly on the material, geometry and size. These properties can be further developed into dynamic or coherently controlled properties by making use of the mechanical response of the nanostructure, by producing Micro-Electro Mechanical Systems (MEMS) or Nano-Electro Mechanical Systems (NEMS) (Ekinci and Roukes (2005)).

MEMS and NEMS have been proposed as components for sensing in applications from pressure sensors, mass sensors or to investigate mechanical effects on the nanoscale. Fully characterising the acousto-optic interaction and response, and the heat capacity of the structures is of interest to design nanostructures for applications.

Structures that have been demonstrated to respond acoustically to optical driving are: metallic nanoparticles (Del Fatti et al. (1999), Hartland (2002), Hartland (2006), Arbouet et al. (2006), Pelton et al. (2009),Guillet et al. (2012)) semiconductor nanowires (Kolomenskii et al. (2010), Mariager et al. (2010), Mante et al. (2012)), semiconductor superlattices (Dekorsy et al. (2008)), individual nanodisks (Tachizaki et al. (2010), Ding et al. (2011), Sun et al. (2012)), photonic crystal fibre (Wiederhecker et al. (2008), Kang

et al. (2009), Stiller (2011), Beugnot and Laude (2012)), nano-cantilevers (Babaei Gavan et al. (2009), Sadeghian et al. (2010)) and plasmonic nanostructures (O'Brien et al. (2014)).

In the nanostructures described previously there are several routes to driving mechanical oscillations depending on the material under study, and more than one may be present in the selected nanostructure. For metallic structures the mechanisms are primarily photo-thermal (Hartland (2006), Pelton et al. (2009), O'Brien et al. (2014)), hot-carrier relaxation (Del Fatti et al. (1999), Hartland (2002), Arbouet et al. (2006)) and stimulated Raman or Brillouin scattering (Kolomenskii et al. (2010)). For semiconductor and dielectric structures the mechanisms may be thermal (Babaei Gavan et al. (2009), Guillet et al. (2012), Sadeghian et al. (2010)), carrier relaxation may transfer energy to the structure (Mariager et al. (2010), Dekorsy et al. (2008)), deformation potential (Mante et al. (2012)), and electrostriction (Wiederhecker et al. (2008), Stiller (2011), Beugnot and Laude (2012)).

The ability to drive the structures at resonance provides a more efficient way of transferring energy into the system and selectively enhance modes that would be otherwise suppressed. This is a key result of previous research by Hartland (2006), Arbouet et al. (2006) and O'Brien et al. (2014): they have demonstrated coherent control of the mechanical resonances, by generating resonant and anti-resonant pulse trains. These techniques have demonstrated the potential of selective excitation of mechanical resonances which is proposed in this research as a route to driving nanostructures with GHz resonances into highly excited regimes at resonance frequencies that may not be visible under thermal excitation.

1.2.1 Resonant Periodic Impact Excitation

Vibrational resonances of nanostructures are of interest for study with a VECSEL because the repetition frequencies lie within the range 1-10 GHz. They have been intensively studied by various pump-probe techniques, able to extract the material properties

of the nanostructures and determine differences with bulk material. Interest in light interactions with mechanical oscillators extends from coherent excitation to fundamental interactions.

The starting point for the work described in Chapter.5 of this thesis was the drive to revolutionise the way temporal response of nanostructures is performed. Currently, time-domain analysis can be performed by time resolved SEM (Hasheminejad and Gheshlaghi (2010)), TEM (Nam et al. (2006)) or AFM (Wong (1997)) for μm length structures. Alternatively, most methods for measuring temporal response rely on pump-probe spectroscopy, to obtain transient absorption or scattering. However, time-domain pump-probe spectroscopy is limited by the speed and stability of the temporal delay line, and requires bulky lasers and metre-long delay lines for GHz analysis.

In the frequency-domain, detection has been performed with non-resonant excitation of the nanostructure under study, which relies on the passive thermal or induced excitation of acoustic modes. Difference frequency measurements have also been demonstrated showing that Q-factor limited measurement of resonances can be performed (Kang et al. (2009), Wiederhecker et al. (2008)). Frequency-domain measurement has also been reported in Karvounis et al. (2015), where a CW laser was modulated with an EOM to resonate the acoustic mode up to 200 MHz. We have proposed measuring instead in the frequency domain with a tunable repetition frequency source, combining the mode selectivity demonstrated by coherent control and the speed of frequency-domain measurement compared to time-domain. The technique also presents the opportunity to excite the nanostructures into regimes otherwise unreachable with single intense pulses or resonantly modulated CW, as it will provide a resonant buildup of excitation with high peak power.

The ML-VECSEL provides a compact fs-pulse source, which can be designed for continuously tunable repetition-rate. Therefore the measurement we have proposed would reduce the footprint of the laser, and the length of delay lines from metres to centimetres. The distinctive characteristics of the mode-locked VECSEL make it suitable as a pump laser for this application. Tunability of the repetition frequency is achievable as it is not a Kerr lens mode-locked laser, like a Ti:Sapphire, and does not require a cavity

operating near a stability limit. VECSELs can be readily operated at GHz repetition frequencies matching nanostructure resonance frequencies. Therefore, we have aimed to demonstrate coherent excitation of GHz resonances in nanostructures for a frequency domain approach to acoustic nanostructure characterisation. This new approach needed to answer two questions: Under what conditions can a measurable signal be detected? Can periodic impact excitation of a high-Q-factor resonance create more highly excited modes than intense isolated pulses? To answer these questions this thesis first reports efforts to measure the acoustic response in the time-domain.

1.2.1.1 Time-Domain Pump-Probe Spectroscopy

Radiation incident on the nanowire samples alter the position of atoms in the structures resulting in acoustic vibrations (Mante et al. (2012)). The processes that govern the acousto-optic transfer are known as: displasive mechanism, deformation potential generation, or electrostriction (applicable to dielectric materials) (Gauster and Habing (1967)). Acoustic response on semiconductor nanostructures can be observed by measuring the effect using a pump probe setup on optical transients (Kolomenskii et al. (2010) Dekorsy et al. (2008)). Pump-probe is a technique that excites the sample with

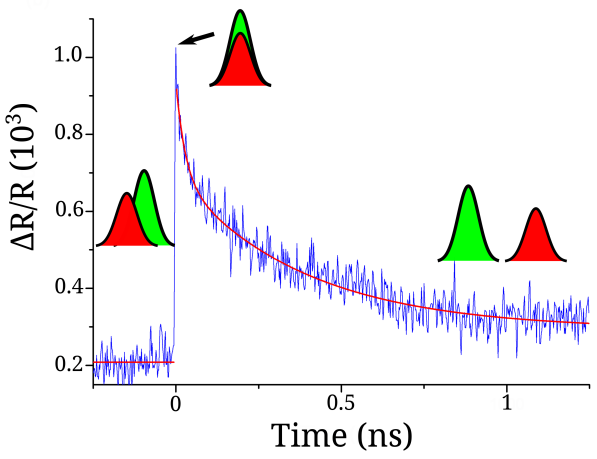

Figure 1.3: *Typical optical transient for a pump-probe experiment. Pump pulse (green) and probe pulse (red), indicate the order of arrival at the sample. When probe arrives before the pump no carriers are produced so the response is flat (red trendline left), a peak occurs when both arrive simultaneously and decays exponentially (red trendline right) as the probe arrives long after the pump (relative to pulse duration).*

one pulse and measures the response with another pulse. Modulating the difference in arrival time of the two pulses is used to measure the changes in reflectivity and transmission that result from the vibrations of the structure. Acoustic vibrations will modulate these changes and can be observed as an oscillatory component on typical pump-probe traces.

1.2.2 Nanostructure Selection

To be considered viable candidates for periodic impact excitation spectroscopy, nanostructures had to fulfil a number of criteria. They had to exhibit vibrational resonances near 1 GHz, where the tZ-VECSEL was capable of high pulse quality and broad tunability. The Q-factor of the resonance had to be at least ≈30, to see a ten-fold enhancement in amplitude over that driven by a low repetition frequency laser of the same average power (See Appendix.E for derivation).

This research focuses on nanowires and nano-cantilevers. The structures have been selected by a combination of factors: resonance frequency, detection mechanism and availability. Resonance frequencies that can be targeted by the VECSEL, are approximately GHz, which restricts the nanostructures available for direct excitation. The detection of sample resonance is performed by making a time or frequency domain measurement of reflectivity/transmittivity. Therefore, it is required that the selected sample display a reflectivity/transmittivity that is structurally dependent. Finally, the nanowires were selected from available samples in the group from Muskens et al. (2009), and the nano-cantilevers were designed specifically for this research and fabricated by O. Buchnev.

1.2.3 FEM Modelling

To predict the mechanical resonances of the nanostructures a finite element method (FEM) simulation in COMSOL Multiphysics was developed. The model has been tested by simulating acoustic modes of GaP nanowires and showed strong agreement with experimental results for acoustic resonances presented in the work of Mante et al. (2012).

Subsequently the model has been applied to the nanostructure geometry and materials, to find a sample and design with a suitable vibrational resonance.

The software for modelling used the Finite Element Method (FEM) for acoustic mode prediction, and successfully predicted GHz acoustic resonances for nanostructures showing dependence of magnitude and frequency primarily on the shape and material parameters. The model was then applied to compare to existing data presented in Mante et al. (2012). The model was applied to simulate structures previously documented with both experimentation and modelling, that are similar to the proposed samples for my research. Finally managing to improve upon the correlation between theory and experiment. This was achieved by adjusting the structure geometry in the model to include an observed tapering; matching the simulated modes frequency to measured peaks more accurately than presented research.

The model was used in conjunction with SEM analysis of nanostructure samples. Efforts were also made to model the Q-factor of the resonance under study. The model to calculate the Q-factor takes the calculated eigenfrequencies of the structure, combines this with the excitation of the structure (e.g. thermal expansion or electrostriction) and finally uses material losses to show the time domain behaviour of the structure under study, this model ultimately gave values that were unreasonably high for Q-factor due to lack of considerations of: surrounding air and full consideration of material losses, which are expanded upon by the analysis performed by Babaei Gavan et al. (2009).

The research to characterise nanostructure samples is described in Chapters 3 and 4 for nanowires and nanocantilevers respectively. First the linear spectra of the proposed samples were found, and then the samples were tested using a time domain pump probe measurement.

Finally, in Chapter.5, the nanostructures were used in a new frequency domain spectroscopy technique using the laser described in Chapter.2.

1.3 Intracavity Generation of Broadband Terahertz Pulses Using a Mode-Locked-VECSEL

The third topic investigated in this research is the application of fs laser sources to compact THz time-domain spectroscopy (THz-TDS).

THz-TDS is a pump-probe technique that can characterise absorption and time of flight of pulsed electromagnetic radiation within the THz band, between infrared and microwave. This region of frequencies has been of particular interest for applications such as molecular identification, by detecting the fingerprint spectra of the molecules in the sample under study, and also the structural analysis of thin films, for which THz wavelength is ideal for assessing thickness and refractive index via time of flight measurements (Beard et al. (2002), Ferguson and Zhang (2002), Lewis (2014)). A major drawback of performing this analysis is the long time it takes to perform a scan, acquisition may take 1/2 hour per scan. This is a fatal obstacle for 2D imaging in real time with THz. In addition, driving THz emission requires fs pulses, which are typically provided by a large laser system, making the technique not very compact.

To address the limitations of conventional THz generation and detection we have proposed the VECSEL to provide the THz seed-pulse. VECSELs can provide a fs-pulse train with a GHz repetition-rate, a ten-fold increase over conventional fs sources that can translate directly to reducing acquisition time. The VECSEL also provides a very compact fs source to drive the THz emission. Another advantage of the VECSEL makes use of the first avenue of research, repetition-rate tuning. The tuning of repetition frequency can be harnessed to make an Optical Sampling by Cavity Tuning (OSCAT) measurement to even further improve scan rates (Wilk et al. (2011)).

Not only can THz-TDS be improved with the use of a VECSEL, to pump broadband THz-pulses, but the VECSEL also provides a platform for developing intracavity generation of THz-pulses. Thanks to the external cavity it is possible to include nonlinear intracavity elements, and the high intracavity power present in the VECSEL takes full advantage of their inclusion. VECSEL nonlinear intracavity conversion benefits from key features of the laser: low gain, high-Q cavity, large intracavity optical field, fast gain

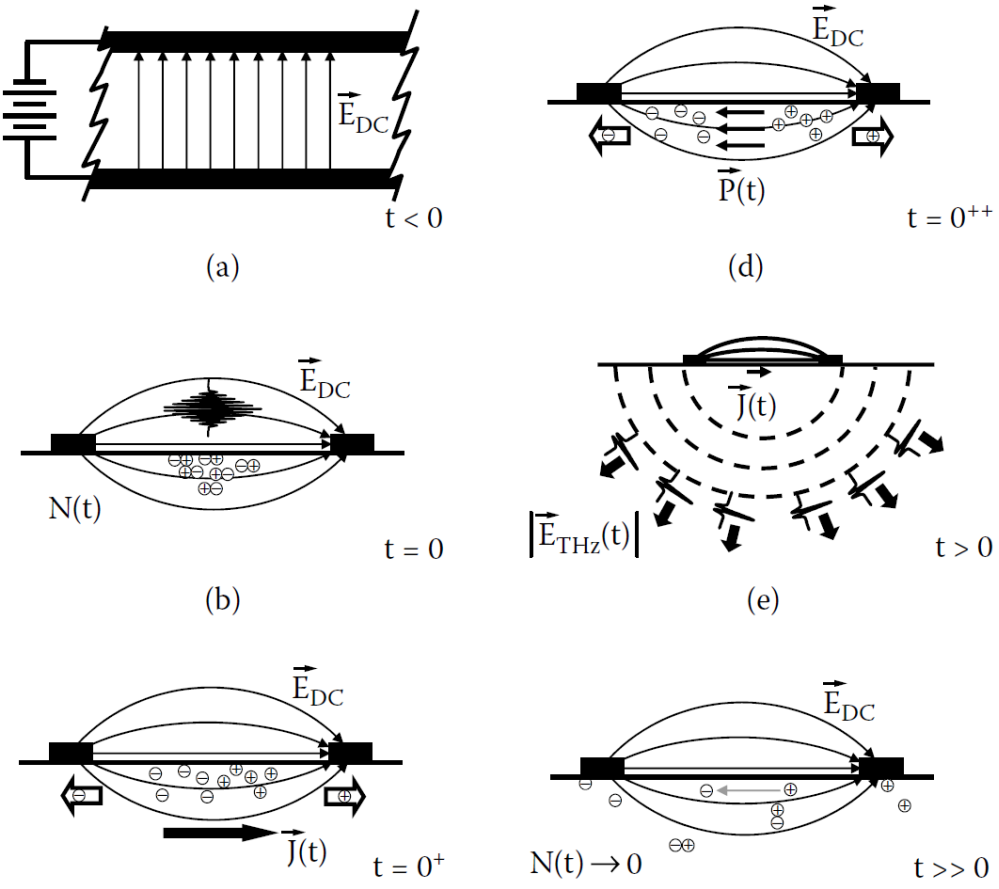

Figure 1.4: *A schematic diagram of the operation of a strip-line photoconductive antenna for THz emission (a) Two metallic strips fabricated in parallel onto a high-mobility semiconductor material are biased with a voltage E_{DC}. (b) An optical pulse is used to excite charge carriers in the semiconductor material. (c) The field E_{DC} accelerates the charge carriers. (d) An opposing field $\vec{P}(t)$ is generated by the increased separation of electrons and holes. (e) The induced polarisation creates a transient current, which causes the THz-emission. (f) finally carriers recombine. Figure from Dexheimer (2008).*

recovery time (100 ps - 1 ns) even with nonlinear loss present in the cavity. As such, VECSEL nonlinear conversion has been investigated for a number of conversion mechanisms: Second Harmonic Generation (SHG) in CW is now a standard commercial route, Optical Parametric Oscillator (OPOs) and Raman lasers and intracavity CW THz by Dual Frequency Generation (DFG) with intracavity Periodically Poled Lithium Niobate (PPLN).

Therefore, to harness the compactness and the readiness for intracavity elements of the VECSEL, we propose intracavity generation of pulsed-THz. To produce pulsed THz a flow of charge is required, experimentally this takes the form of a transient current

of photocarriers. The emission from the flow of these photocarriers may be described by Maxwell's equations. As shown in the expressions Eqn.1.2 and Eqn.1.3, where the current density magnetic flux and electric displacement are given by Eqn.1.2. As long as it is possible to induce a change over time in one of the terms: permeability $\mu(t)$, emissivity $\varepsilon(t)$ or conductivity $\sigma(t)$ a material can be used for electromagnetic (EM) emission according to the Maxwell equations,

$$\nabla \times \vec{E}_{THz}(t) = -\frac{\partial \mu(t)\vec{H}_{THz}(t)}{\partial t} \tag{1.2}$$

and,

$$\nabla \times \vec{H}_{THz}(t) = \sigma(t)\vec{E}(t) + \frac{\partial \varepsilon(t)\vec{E}_{THz}(t)}{\partial t} \tag{1.3}$$

where $\mu(t)H(t) = B(t)$ is magnetic flux density, $J(t) = \sigma(t)E(t)$ is current density and $\varepsilon(t)E(t) = D(t)$ is electric displacement (Dexheimer (2008)). The mechanism used experimentally for emission is to cause a change in conductivity $\sigma(t)$ by using an intense ultrashort pulse to induce rapid transient changes through photoconduction. The changes induced by fs-scale optical pulses and acceleration of carriers results in THz emission.

For the case of bulk GaAs, it has been reported Mihoubi et al. (2008) that photoconduction may be induced by resonant or non-resonant excitation. This means that carriers may be generated by photon absorption or by nonlinear optical frequency difference generation. In the fs ML-VECSEL, photocarriers are already present in the SESAM when it saturates under the intracavity pulse. Once the carriers are excited by the pulse, a voltage is needed to produce the transient current. To make this addition to a VECSEL a stripline antenna is patterned onto the SESAM surface, to which a DC or AC voltage can be applied.

The stripline Photoconductive Antenna (PCA) consists of two metallic strips, typically gold of ≈100-nm thickness. This antenna is patterned onto a semiconductor substrate Auston et al. (1984). The mechanism to produce THz with a PCA is shown in Fig.1.4.

First, an intense ≈100-fs optical pulse ($I(t)$) is used to excite charge carriers in the semiconductor. Next a bias voltage E_{DC} causes the carriers to accelerate (electrons to cathode and holes to anode). The separation of the carriers produces an opposing field $\vec{P}(t)$ which creates a transient current, causing THz emission.

Therefore, for a standard PCA, the THz emission depends on carrier population and acceleration field, which relate to optical pulse intensity and bias voltage respectively. In addition, it has been reported that proximity of the excitation spot to the cathode enhances THz emission Ralph and Grischkowsky (1991). This effect is observed due to the increased difference in carrier acceleration between the electrons and holes which breaks the dipole symmetry which would otherwise cancel out the emission.

In Chapter.6 the design process for producing a photoconductive-antennna semiconductor saturable absorbing mirror (PCA-SESAM) is described. This intracavity element was built with dual function as a standard intracavity SESAM, while being able to use the intracavity pulse to drive THz emission. The PCA-SESAM was applied to mode-lock a VECSEL cavity, with an applied bias voltage necessary for THz emission. The PCA-SESAM was also characterised with a standard THz time domain spectroscopy experiment (THz-TDS) to detect the THz emission of the device.

Chapter 2

Broadly Repetition-Rate Tunable Laser

This chapter describes the construction and characterisation of a mode-locked VECSEL designed for resonantly driving a target nanostructure at GHz frequencies. The resulting device emitted up to 230-fs pulses at a centre wavelength of 1035 nm, with an average power of up to 50 mW. The tuning range achieved by this laser was 960 MHz - 1.72 GHz, or a centre tuning frequency of 1.34 GHz with ±28%. A lower power version of the laser with a larger tuning range is also presented, which produced an average output power of 20 mW with 230-fs at a repetition frequency tuning range of 880 MHz - 1.88 GHz, or a centre tuning frequency of 1.38 GHz ±36%. The VECSEL performance presented here is the first report of a VECSEL tunable over such a large range close to 1 GHz while being able to produce sub-300-fs pulses for the majority of it's tuning range.

In the following sections an introduction to VECSEL design is presented, including aspects of VECSEL cavity design that will directly affect mode-locking performance. This is followed by an account of using 1-μm anti-resonant (AR) gain-structures for a mode-locked Z-cavity at GHz repetition-rate. Finally, the characterisation of a tunable-Z-cavity (tZ-cavity) VECSEL, using 1035-nm flip-chip resonant samples, is reported. This includes a model I developed for optical cavity design, the model was used to predict the cavity design lengths and optics required for stable cavity length tuning.

2.1 VECSEL Semiconductor Structures

For this research, two sets of VECSEL structures were used, each set being a gain structure and SESAM. The first set were standard GaAs wafers grown via MBE at University of Cambridge for operation near 1 μm. The second set consisted of a standard GaAs SESAM both designed for operation close to 1035 nm, also grown at University of Cambridge, and a flip chip fabrication GaAs gain-structure grown by MBE at UULM university. Here the composition and calculated properties are presented and discussed.

2.1.1 1-μm Structures

An anti-resonant GaAs gain-structure (known as V629), designed for operation at 1 μm, was used in this research in the first iteration of VECSEL designs. This structure was selected for its broad gain bandwidth, and compatible SESAM availability essential for mode-locking. The gain-structure design is shown in Fig.2.1(a), the microcavity $|E_{field}|^2$ at the design wavelength (997 nm) is overlaid onto the structure design. The structure contains 6 $In_{0.26}Ga_{0.74}As$ QWs arranged to align 4 with the microcavity anti-nodes (RHS) with a gap between the two deepest QWs leaving an anti-node un-enhanced, and two QWs arranged in closer proximity (LHS). This layout has been selected to result in the anti-resonant profile displayed in Fig.2.2(b).

The structure design can be used to calculate the GDD, the reflectivity and the $|E_{field}|^2$ enhancement profile (Fig.2.2(a & c)). The $|E_{field}|^2$ profile as a function of wavelength (Fig.2.2(c black)) displays the characteristic AR enhancement profile peaking either side of the design wavelength, at 968 and 1041 nm (shown in Fig.2.2(c black)), resulting in a broader gain profile than a traditional resonant structure. The broad gain-bandwidth enhances wavelength-tunability, typical of anti-resonant samples, this allows greater adjustability of the gain profile than single-QW resonant structures, which can be critical for mode-locking. Structure reflectivity is shown in Fig.2.2(c green), the high reflectivity of the sample is engineered with a 27.5-pair $AlGa_{0.3}As$/GaAs DBR (Distributed Bragg Reflector) with a stop-band from 950-1050 nm. Finally, GDD of the structure can be

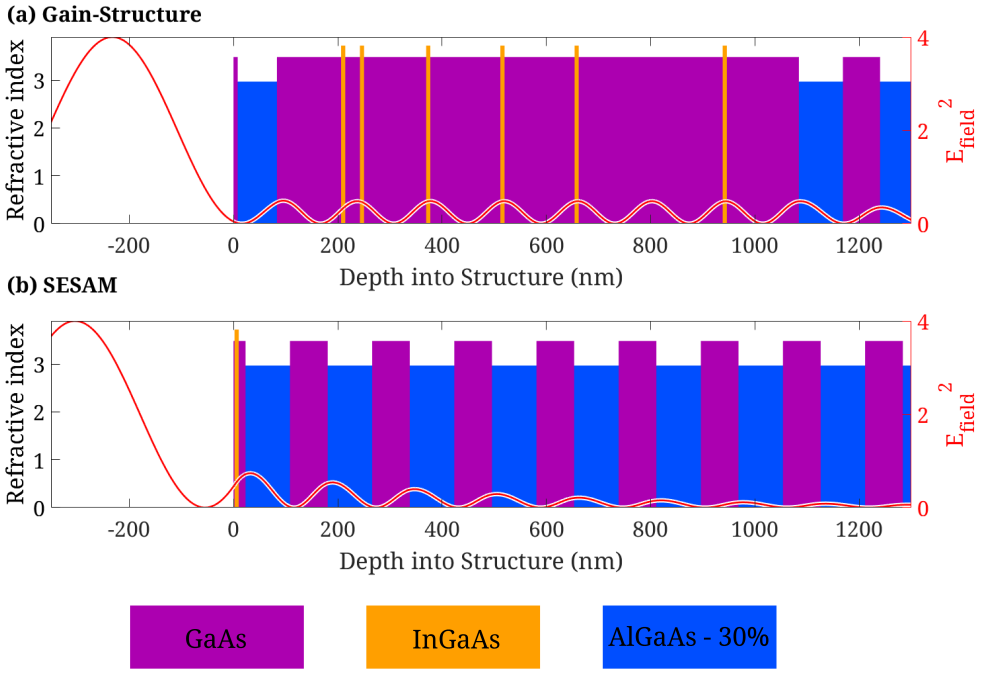

Figure 2.1: *The refractive index as a function of depth into the structure, with colour-coded material in the key below. The depth is cut off at 1300 nm, so the total of 27.5-pairs of DBR material in each structure is not displayed. The* $|E_{field}|^2$ *as a function of depth into the structure is also displayed (red line, right axis) at 997 nm. (a) 1-*μ*m AR 6-QW gain-structure. InGaAs QWs are arranged into a pair followed by 4 QWs with a space between the last two single QWs. The anti-resonant (AR) microcavity* $|E_{field}|^2$ *has a node at the air-structure interface supressing the antinodes at the QWs (b) 1-*μ*m surface recombination SESAM with a single InGaAs QW at approximately 2.1 nm from the surface, followed by a spacer layer and a 27.5-pair GaAs/AlGaAs DBR.*

calculated, shown in Fig.2.2(a), the gradient of the GDD at the design wavelength indicates that high-order phase structure would be present in pulses from this sample, and the pulses would not be transform-limited.

A GaAs surface recombination SESAM (known as V628), designed for operation at 1 μm, was included in the VECSEL with the AR 1 μm gain-structure to provide saturable absorption. The SESAM structure is shown in Fig.2.1(b), displayed with the microcavity $|E_{field}|^2$ at the design wavelength (997 nm).

The SESAM contains a single 8-nm thick $In_{0.26}Ga_{0.74}As$ QW, located at 2.1 nm from the sample surface allowing for carrier recombination. There is a small amount of buffer material behind the QW, followed by a DBR. The structure design was used to calculate: the GDD, the reflectivity and the $|E_{field}|^2$ interaction at the QW (Fig.2.2(b & d)).

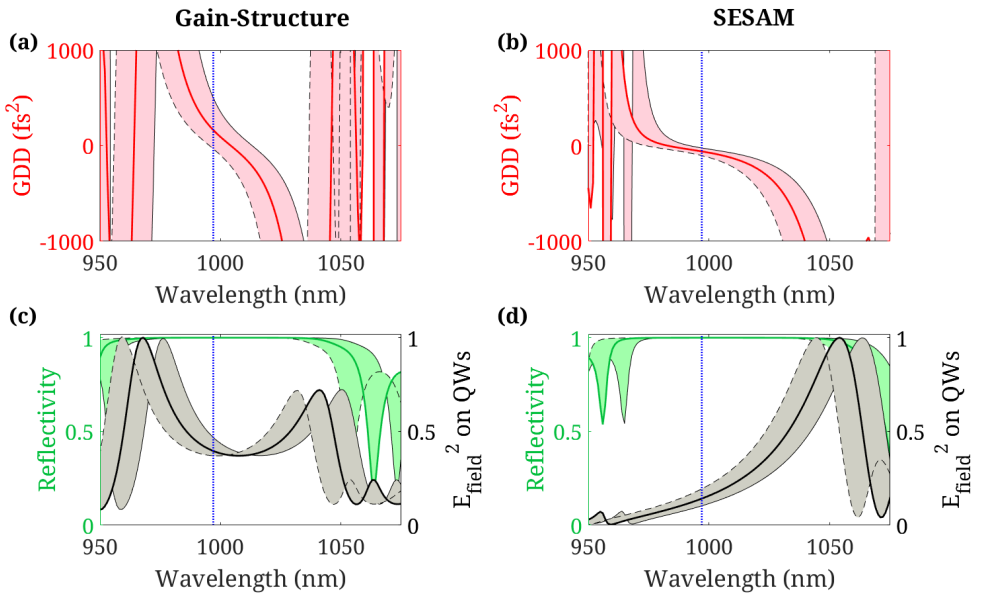

Figure 2.2: *Layer-list calculations for the 1035-nm gain-structure (a and c), and the 1035-nm SESAM (b and d). GDD (red) for (a) the gain stucture and (b) the SESAM, Reflectivity (green) and $|E_{field}|^2$ on the QWs for (c) the gain stucture and (d) the SESAM. All are displayed with filled areas corresponding to -1% (dashed) and +1% (solid) growth error, and the design wavelength of 1035 nm (dashed blue).*

Reflectivity of this structure was designed with a 27.5-pair $AlGa_{0.3}As/GaAs$ DBR with a stop-band from 950-1050 nm (the same design as the 1μ-m gain-structure). The calculated GDD of the SESAM structure is shown in Fig.2.2(b), and is approximately flat at the design wavelength.

The V628 and V629 were selected from available structures as a well matched gain-structure and SESAM pair. The broad emission of V628 was a result of its anti-resonant design, but as a standard growth with no processing its power handling and GDD limited pulse durations to 450 fs or longer. V628 provided a well matched absorption wavelength and flat GDD at V628's emission wavelength. The VECSEL cavities built with these structures were a Z-cavity and V-cavity, described in Sec.2.2 and Sec.2.2.1.

Non-linear reflectivity measurement would enable the retrieval of SESAM parameters for mode-locking. For V629 this measurement was not possible as a fs laser at the design wavelength was not available. The parameters have been measured for V623 in Sec.2.1.1 and are displayed in Table.2.1. The structure designs for both V629 and V623

are designed for very similar operation at their respective design wavelengths, therefore it was concluded that both had very similar parameters.

2.1.2 1035-nm Structures

The second set of VECSEL structures were designed for operation at 1035 nm. The key drive to use these structures was that the gain structure had been designed and processed to optimise high power mode-locking. The primary changes are resonant double quantum well (DQW) design, "flip-chip" fabrication process and a dielectric coating.

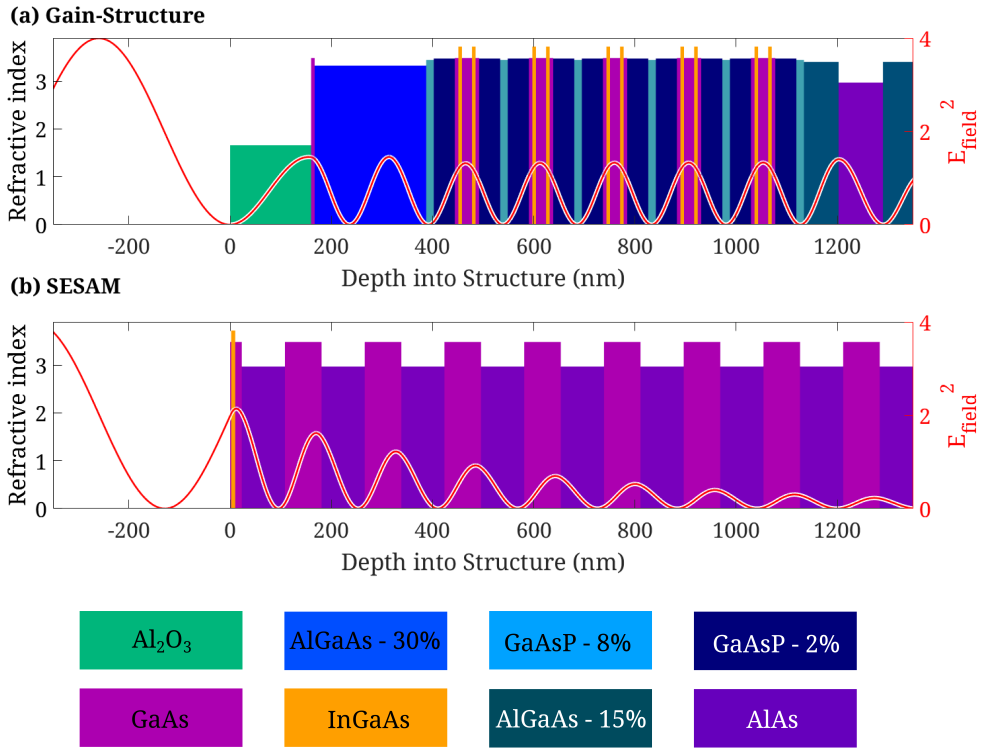

Figure 2.3: *The refractive index as a function of depth into the structure, with colour-coded material in the key below. The depth is cut off at 1300 nm, so the total of 27.5-pairs of DBR material in each structure is not displayed. The E-field^2 as a function of depth into the structure is also displayed (red line, right axis) at 1035 nm. (a) 1035-nm 5-DQW gain-structure. InGaAs DQWs for greater and broader enhancement are shown and the $|E_{field}|^2$ plot shows that the antinodes of the mode line up with the DQWs, as expected for a resonant structure. (b) 1035-nm surface recombination SESAM with a single InGaAs QW at approximately 2.1 nm from the surface, followed by a spacer layer and a GaAs/AlAs DBR.*

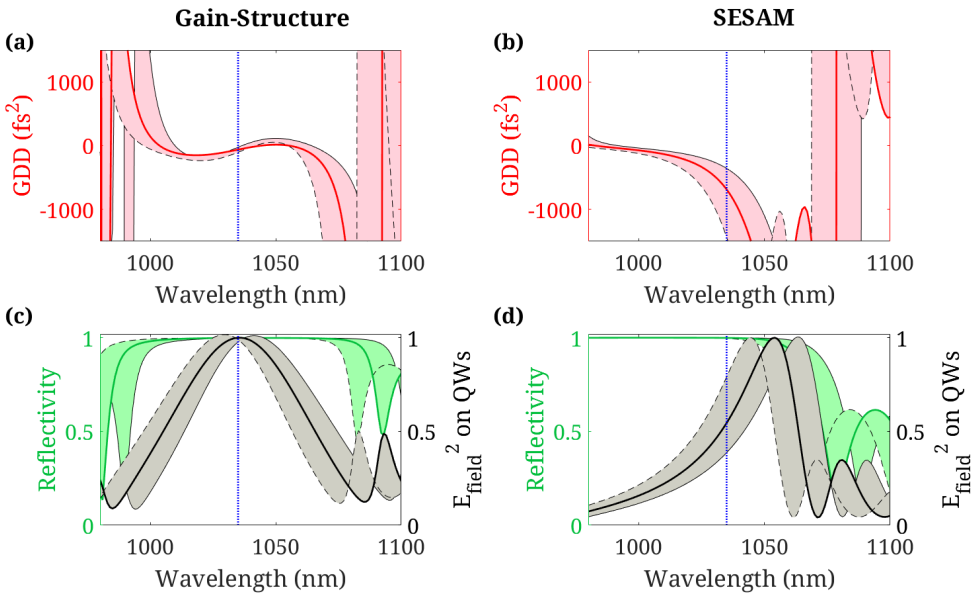

Figure 2.4: *Layer-list calculations for the 1035-nm gain-structure (a and c), and the 1035-nm SESAM (b and d). GDD (red) for (a) the gain stucture and (b) the SESAM, Reflectivity (green) and $|E_{field}|^2$ on the QWs for (c) the gain stucture and (d) the SESAM. All are displayed with filled areas corresponding to -1% (dashed) and +1% (solid) growth error, and the design wavelength of 1035 nm (dashed blue).*

The gain structure is known as H29. The resonant design of this structure provided high enhancement of the $|E_{field}|^2$ in the microcavity at the design wavelength. In contrast to a traditional single QW design, the DQW provides a broader gain bandwidth since, thanks to the greater distribution of QWs, a larger bandwidth will see enhancement due to lining up the anti-nodes with DQWs. A dielectric coating is added as an anti-reflection coating for dispersion management and to suppress the microcavity resonance.

The structure design is shown in Fig.2.3. As this design is a "flip-chip" it is grown from a GaAs substrate which is later etched away, leaving a small layer at approximately 160 nm depth. Next a window layer of $AlGa_{0.3}As$ is deposited to supress air-surface recombination of carrier, which would deplete the available gain in the VECSEL. Next the active region was grown, containing a total of 10 QWs arranged into 5 DQWs. Each DQW was grown in a barrier layer of GaAs, with layers of $GaAs_{0.08}P$ and $GaAs_{0.02}P$ for strain compensation. After the active region a 27.5-pair $AlGa_{0.3}As$/AlAs DBR. Once the sample was grown it was soldered onto an extracavity diamond heat spreader and the intracavity side was coated with the dielectric coating, 160-nm thickness Al_2O_3. The

Structure	**V623**
Wavelength (nm)	1035
F_{sat} $(\mu J/cm^2)$	7.4 ± 0.4
ΔR (%)	3.11 ± 0.05
$L_{non-sat}$ (%)	0.32 ± 0.03
Induced Absorption (mJ/cm^2)	292 ± 30
τ_{slow} (ps)	5.7 ± 0.5

Table 2.1: *SESAM characteristics for V623.*

GDD of the gain structure has been designed to be approximately flat for the design wavelength (Fig.2.4(a)), essential for reducing pulse durations to approach the transform limit. The reflectivity of the structure is dominated by the DBR stop-band, from 990-1075 nm. The $|E_{field}|^2$ enhancement profile has a broad resonant profile peaking at the design wavelength.

For mode-locking a 1035-nm SESAM was selected (known as V623), that contains a single 8-nm thick $In_{0.26}Ga_{0.74}As$ QW at a depth of 2.1 nm. The structure for this SESAM is shown in Fig.2.3(b). The calculated GDD, reflectivity and $|E_{field}|^2$ interaction with the QW is shown in Fig.2.4. The 1035-nm SESAM structure is approximately the same as the 1-μm SESAM but the DBR has been changed from 27.5-pairs of $AlGa_{0.3}As$/GaAs to AlAs/GaAs to change the stop-band of the structure. The GDD for the SESAM is displayed in Fig.2.4(b), the structure does not have flat GDD at 1035 nm, which may lead to high order phase structure, this is discussed further in the results for the lasers that used these structures (Sec.2.3).

Non-linear reflectivity measurements extracted the parameters shown in Table.2.1. The slow recovery time of this SESAM was founds to be $\tau_{slow} = 5.7 \pm 0.5ps$, characterised by Turnbull (2015) via a pump probe measurement.

2.2 Mode-Locked Operation of an Anti-resonant Z-cavity VECSEL

A preliminary study for the development of the tZ-cavity design was made using a standard Z-cavity VECSEL. V628 and V629 were tested with a Z-cavity to determine

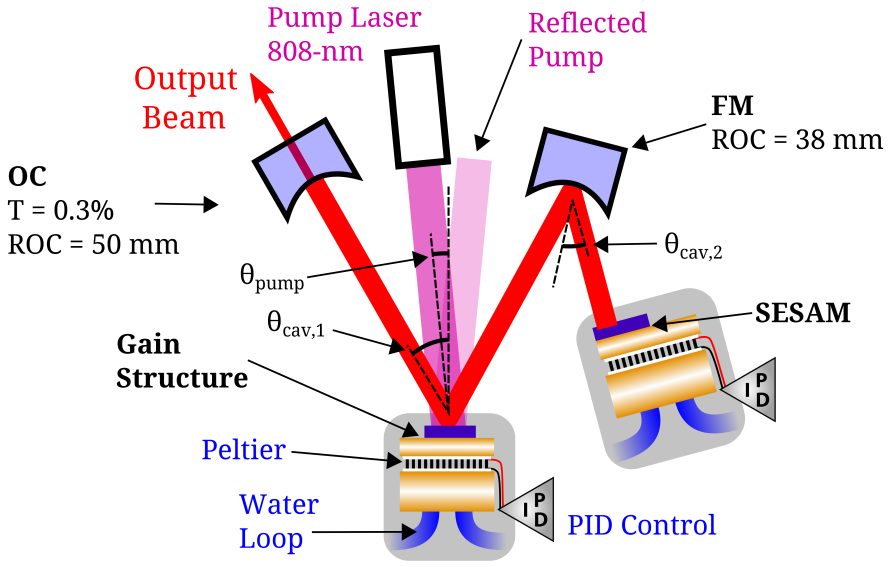

Figure 2.5: *Schematic diagram of the Z-cavity VECSEL. The VECSEL is pumped by a fibre coupled 808-nm bar diode-laser at a half angle of* θ_{pump}= *5°. The cavity elements are SESAM, Fold Mirror (FM), Gain Structure and Output Coupler (OC), forming a "Z-shaped" intracavity mode at half angles of:* $\theta_{cav,1}$= *22° and* $\theta_{cav,2}$= *15°. The Gain structure and SESAM are cooled actively by PID-controlled Peltier thermoelectric cooling, and passively by cooled water loop. The intracavity beam waist and folded-out cavity are displayed in Fig.2.6.*

their viability for mode-locking in a tZ-cavity, since the tZ produces lower area-ratios which can be critical for stable mode-locking. The Z-cavity is defined by its Z-shape, given by the four cavity elements present in the cavity, output coupler mirror, gain-structure, fold mirror and SESAM, shown in Fig.2.5.

V628 was previously found to emit average output power in excess of 500 mW CW. In addition, layer list calculations and photo luminescence (PL) spectra indicated band-widths larger than 5 nm, ideal for mode-locking. The structure samples available for use displayed a high concentration of strain damage defects, known as dark-line defects, therefore up to 220 mW CW was achieved when tested as a Z-cavity pumped with 3 W of 808-nm output from a fibre coupled diode laser focused to approximately 90 μm. The CW test was conducted with a high reflecting mirror in place of the SESAM, which introduced additional loss when used for mode-locking.

The Z-cavity VECSEL was pumped with up to 4 W by an 808-nm diode-laser, focused to a 90 μm spot. The VECSEL was constructed as a Z-cavity to allow independent tuning of the mode area ratio between the Gain structure and SESAM, critical for mode-locking

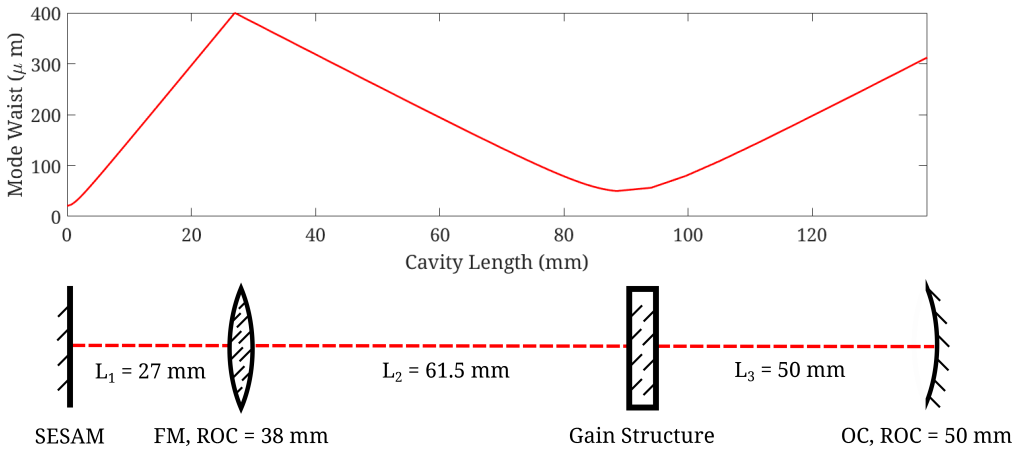

Figure 2.6: *The intracavity mode calculated for a Z-cavity VECSEL built with a 50-mm RoC OC and a 38-mm FM, at separations of:* L_1*= 27 mm,* L_2*= 61.5 mm and* L_3*= 50 mm (as shown in the accompanying folded out cavity diagram). The spot sizes at the gain and SESAM were:* w_{gain}*=50 μm and* w_{sesam}*=21 μm, for an area ratio of approximately 5.6.*

due to the F_{sat} and modulation depth characteristics of the SESAM. The cavity was built with a 50-mm RoC 0.7% output coupler and a 38-mm RoC fold mirror, arranged as shown in Fig.2.6, with separations of L_1 = 27 mm, L_2 = 61.5 mm and L_3 = 50 mm. The cavity mode half angles were: $\theta_{cav,1}$= 22° and $\theta_{cav,2}$= 15°. This cavity arrangement results in a gain spot size of 50 μm and a SESAM spot size 21 μm, for an area ratio of approximately 5.6.

The gain spot size is deliberately made smaller than the pumping spot to compensate for the difference in half-angle between the laser cavity $\theta_{cav,1}$= 22° and the incident and reflected pump beam $\theta_{cav,1}$= 15°. The difference in angle adds ellipticity to both the cavity mode and the pump spot proportional to $sin(\theta)$, and the pump profile may be irregular as a result of the diode laser and fibre coupling. Therefore, the over-filling the gain spot size with the pump spot allows uniform excitation across the laser mode.

The calculated variation of the mode waist along the cavity is shown in Fig.2.6. The temperature of both gain and SESAM structures was adjusted to set the emission of the gain and the absorption of the SESAM to the same wavelength. Thermal adjustment was performed with a combination of Peltier-cooling and water-cooled copper heatsinks, each capable of extracting up to 50 W of heat. To achieve mode-locking, the gain

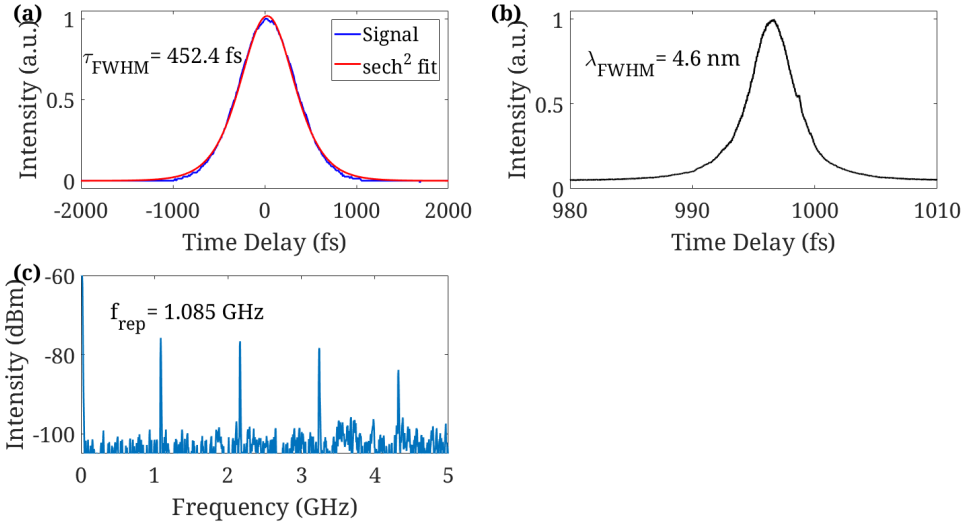

Figure 2.7: *Pulse train characterisation of the 1-μm (V628 and V629) AR Z-cavity VECSEL, pumped at 1 W. (a) Intensity Autocorrelation (blue) with sech^2 fit to extract the time FWHM of 452 fs. (b) Optical spectrum displaying a broad peak of λ=4.6 nm, on an approximately sech^2 peak centred at λ=997 nm. (c) RF spectrum recorded from 0-5 GHz, with first order peak at f_{rep}=1.08 GHz, and stable peak intensities up to 3 GHz (limited by photodiode response). Average output power was P_{avg}=30 mW (P_{peak}=48 W and E_{pulse}= 25 pJ). The time bandwidth product was calculated to be β= 0.447, or 1.42 times the bandwidth limit.*

and SESAM structures were cooled to -10 °C and heated to 30 °C respectively; this was necessary to blueshift gain emission and redshift SESAM absorption for better matching.

Experimentally, it was found that at large cavity-element angles (half angle ≈ 45°), the VECSEL parameters were different enough between orthogonal polarisations that the output was ML (or modulated) in the one polarisation (out of cavity plane) and CW in the other (in cavity plane). This was thought to be due to increased loss and, to a lesser extent, the change in effective thickness of the gain structure.

The pulse train from the Z-cavity was characterised with an optical spectrum analyser (OSA), a radio frequency spectrum analyser (RFSA) and an intensity autocorrelator (AC). Fig.2.7 displays the pulse train characterisation of the Z-cavity, with the laser pumped by 1 W (of 808-nm light focused to a 90-μm spot). The intensity autocorrelation in Fig.2.7(a) is fitted to a hyperbolic secant ($sech^2$) pulse shape, which retrieves a pulse duration at FWHM of 452 fs. The pulse shape shows no pedestal, but differs from a hyperbolic secant either side of the peak close to 1 ps from the centre. Optical spectrum

Pulse length (fs)	450
Wavelength (nm)	997
Wavelength FWHM (nm)	3.55
Rep. Rate (GHz)	1.080
Transform limit	1.42 ($\beta = 0.447$)
Average Power (mW)	30
Pulse Energy (pJ)	25
Peak Power (W)	48

Table 2.2: *Pulse train characterisation for 1-μm AR Z-cavity VECSEL built with V628 and V629.*

(displayed in Fig.2.7(b)) displays a smooth shaped peak at 997 nm, 4.6-nm wide at FWHM, corresponding to 1.42 times the transform limit (β= 0.447). The calculation for transform limit and the variations in the pulse-wings are attributed to phase in the pulse as a result of the GDD gradient of the gain structure near 997-nm (Displayed in Fig.2.2). Finally the RF spectrum (displayed in Fig.2.7(c)) shows a first cavity harmonic of 1.08-GHz, within the targeted range for nanostructure excitation. This frequency can be verified against measured cavity lengths using Eqn.(1.1). The first three harmonics displayed in the RF spectrum decrease in intensity for the latter two peaks, this was a result of photodiode bandwidth (4 GHz) and insufficient bias voltage. The results of pulse train characterisation are summarised in Table.2.2. This result was used to motivate further tests of the gain-structure and SESAM for tunable f_{rep} VECSELs.

2.2.1 Study of a 1-μm V-cavity

Once the mode-locking characterisation was performed with a Z-cavity it was necessary to investigate whether the structures would mode-lock under the conditions available in a tZ-cavity. In a Z-cavity the mode sizes at the gain and SESAM can be designed independently thanks to having a second curved mirror in the cavity between the two elements. Since in a tZ-cavity the gain-structure and SESAM are adjacent cavity elements (shown in Fig.2.10), the mode areas are determined by the single fold mirror. This gives very little variability in the cavity design restricting it to a predetermined gain spot size and area-ratio. For this reason a V-cavity VECSEL was built to test the gain-structure and SESAM combination at lower area ratios than those in the Z-cavity.

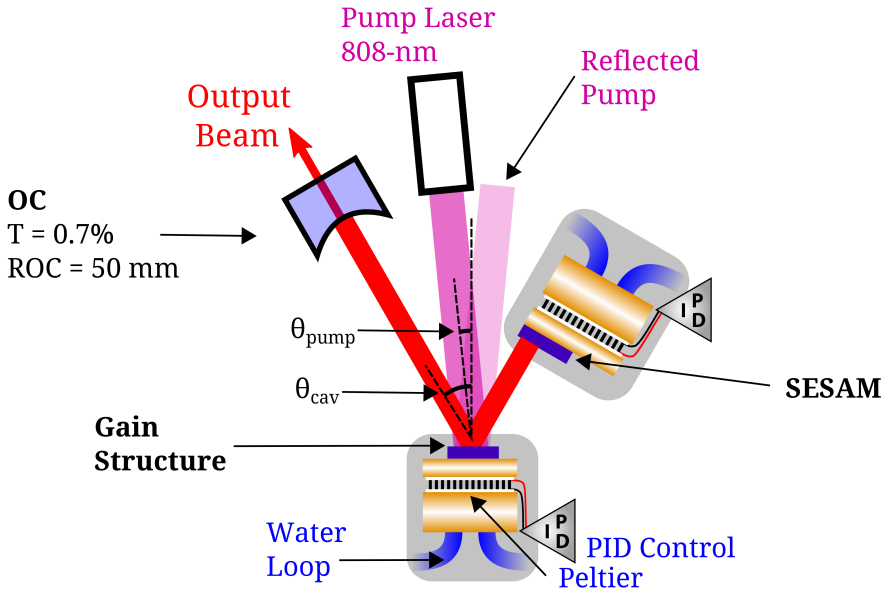

Figure 2.8: *Schematic diagram of the V-cavity VECSEL. The VECSEL is pumped by a fibre-coupled 808-nm bar diode-laser at a half angle of of θ_{pump}= 16°. The cavity elements are SESAM, Gain Structure and Output Coupler (OC), forming a "V-shaped" intracavity mode, at a half angle of θ_{cav}= 32°. The Gain structure and SESAM are cooled actively by PID-controlled Peltier thermoelectric cooling, and passively by cooled water loop. The intracavity beam waist and folded-out cavity are displayed in Fig.2.9.*

The VECSEL V-cavity was constructed with a 75-mm RoC OC, and was tested at multiple transmission values (0.3%, 0.7%, 1.45%). The cavity was pumped by up to 4 W of optical power at 808 nm from a bar diode laser. The cavity lengths used were close to calculated target lengths of: L_1= 5.8 mm and L_2=68.8 mm (shown in Fig.2.9), the resulting cavity mode radii were: w_{gain}=62 μm and w_{sesam}=40 μm, for an area ratio of approximately 2.5. The cavity frequency that would have been achieved when mode-locked was 2 GHz.

These cavity lengths were found via cavity mode calculations similar to those shown in Sec.2.3.1 and mode variation as a function of cavity length changes is displayed in the Appendix.C. Compared to the successfully mode-locked Z-cavity, the reduction in area ratio and increase in repetition frequency were both detrimental to achieving mode-locking.

The 75-mm V-cavity was incapable of producing a stable mode-locked output: optical

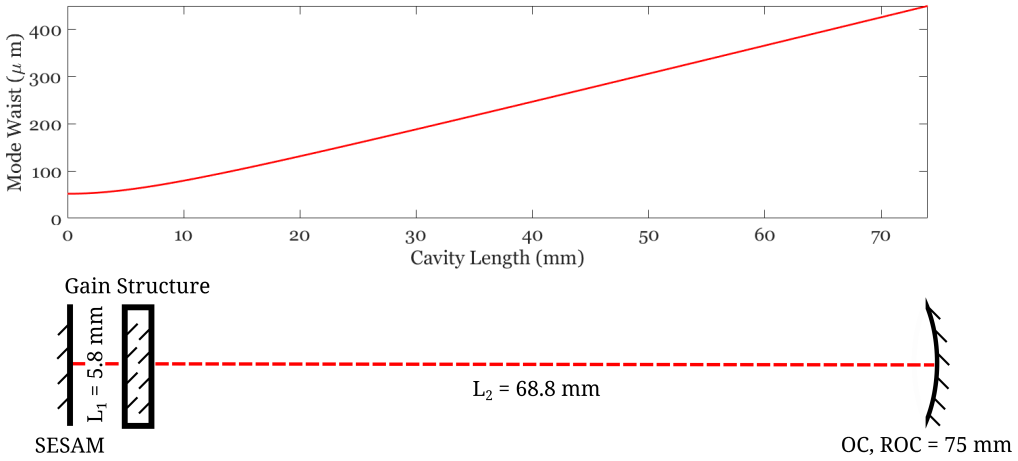

Figure 2.9: *The intracavity mode calculated for a Z-cavity VECSEL built with a 75-mm RoC OC, at separations of:* L_1*= 5.8 mm and* L_2*= 68.8 mm (as shown in the accompanying folded out cavity diagram). The mode sizes at the gain and SESAM were:* w_{gain}*=62 μm and* w_{sesam}*=40 μm, for an area ratio of approximately 2.5.*

spectra showed a modulation of output but intensity autocorrelation and RF spectrum analysis were not possible. This was attributed to the short cavity length resulting in a high repetition rate, which reduces the intra-cavity pulse-energy; which in turn results in low saturation of the SESAM and hence mode-locking is not achieved.

Ultimately, this investigation showed that V628 and V629 would not be viable for a broadly repetition frequency tunable VECSEL. In addition, neither the V-cavity nor the Z-cavity geometry is stable for cavity length changes in either: area ratio or gain spot size, meaning a different cavity had to be designed: the tZ-cavity.

2.3 Tunable Repetition Rate Flip-Chip ML-VECSEL

The goal of the PhD was to produce a tunable cavity-length ML-VECSEL, where the repetition frequency frequency can be tuned by moving the cavity OC. Moving the OC in a VECSEL leads to changes in gain-mode area and SESAM-mode area. Gain-mode area must be kept fixed to match the optical pump spot size, or the cavity power will drop change to the overlap of these two areas. The SESAM-mode area relative to the gain-mode area, known as area-ratio, must also be kept approximately fixed to ensure that the SESAM can saturate properly leading to mode-locking.

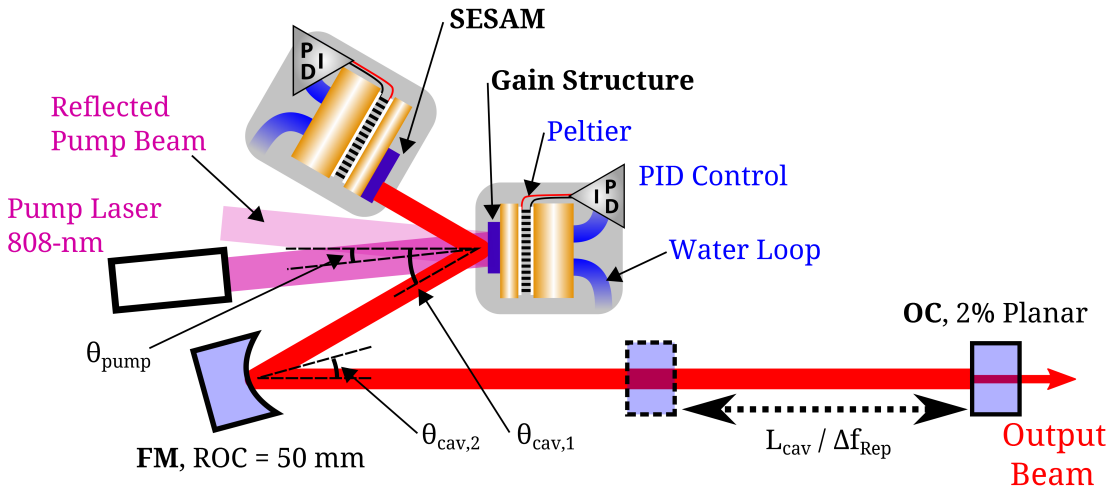

Figure 2.10: *Schematic diagram of the tZ-cavity VECSEL. The VECSEL is pumped by a fibre coupled 808-nm bar diode-laser at a half angle θ_{pump}= 16°. The cavity elements are SESAM, Gain Structure, Fold Mirror (FM) and Output Coupler (OC), forming a "Z-shaped" intracavity mode, at half angles of: $\theta_{cav,1}$= 32° and $\theta_{cav,2}$= 16°. To differentiate from the standard Z-cavity it is known as tunable-Z-cavity VECSEL (tZ-cavity). The Gain structure and SESAM are cooled actively by PID-controlled Peltier thermoelectric cooling, and passively by cooled water loop. The intracavity beam waist and folded-out cavity are displayed in Fig.2.11, L_3 may be varied continuously to vary the cavity repetition frequency Δf_{Rep}.*

Therefore, the design challenge this goal presented was to achieve the greatest OC movement range whilst being able to minimise the variation in gain-mode area and area-ratio. The cavity arrangement used is the tunable-Z-cavity (tZ-cavity, shown in Fig.2.10). The tZ-cavity contains 4 cavity elements forming a "Z-shaped" laser mode but is more closely related to the V-cavity due to the gain-structure and the SESAM being adjacent cavity elements, therefore the area ratio is directly related to the FM-RoC and the gain-structure SESAM separation. This differs from the Z-cavity case where the mode size on the gain-structure and SESAM may be changed independently, achieving higher area-ratios more easily. The cavity lengths may also be tuned to produce a near-collimated section of mode waist. This is shown in Fig.2.11 between the FM (at 50 mm) and OC (at 111 mm), for the same cavity configuration used for mode-locking in Sec.2.3.2 and Sec.2.3.3. The cavity configuration was designed with the help of numerical optimisation code presented in Sec.2.3.1.

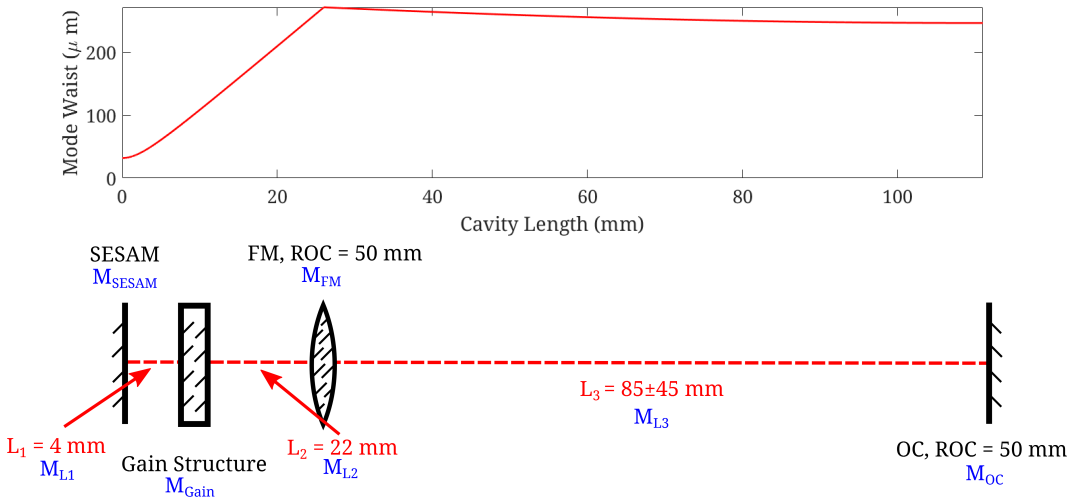

Figure 2.11: *The intracavity mode calculated for a tZ-cavity VECSEL built with a planar OC and a 50-mm RoC FM, at separations of: L_1= 4.2 mm, L_2= 22 mm and L_3= 85 mm (as shown in the accompanying folded out cavity diagram). L_3 may be varied from 53.5 mm up to 144 mm for the largest demonstrated tuning range. The mode sizes at the gain and SESAM were: w_{gain}=52-57 μm and w_{sesam}=27-41 μm, for an area ratio range of approximately 1.7-4.7.*

2.3.1 tZ-Cavity Mode-Area Calculations for Stable Mode-locked Design

Designing the VECSEL laser cavity for the largest possible tuning range while mode-locking constrains the cavity primarily to low variation of two parameters: gain spot size and area ratio (calculated via the quotient of squares of gain-structure and SESAM mode radii). Gain mode size will affect the VECSEL coupling to the optical pump, while mode-locking of the intracavity power will depend on area ratio.

For the tZ-cavity, the beam waist is plotted as a function of distance from the SESAM z in Fig.2.11 (this is also shown for the Z and V cavities in Fig.2.9 and Fig.2.6). However, to facilitate the design phase of the tZ-cavity VECSEL the mode size over cavity length cannot be evaluated for each output coupler position (change in L_3). Instead, the equations for beam waist calculations are evaluated at the gain-structure and SESAM to produce surfaces of variations in size (Figures Fig.2.12).

Surface plots of variations in intracavity laser mode radii were calculated by applying ABCD matrices to the complex beam parameter of the mode. First the ray transfer matrix for the cavity round-trip was calculated,

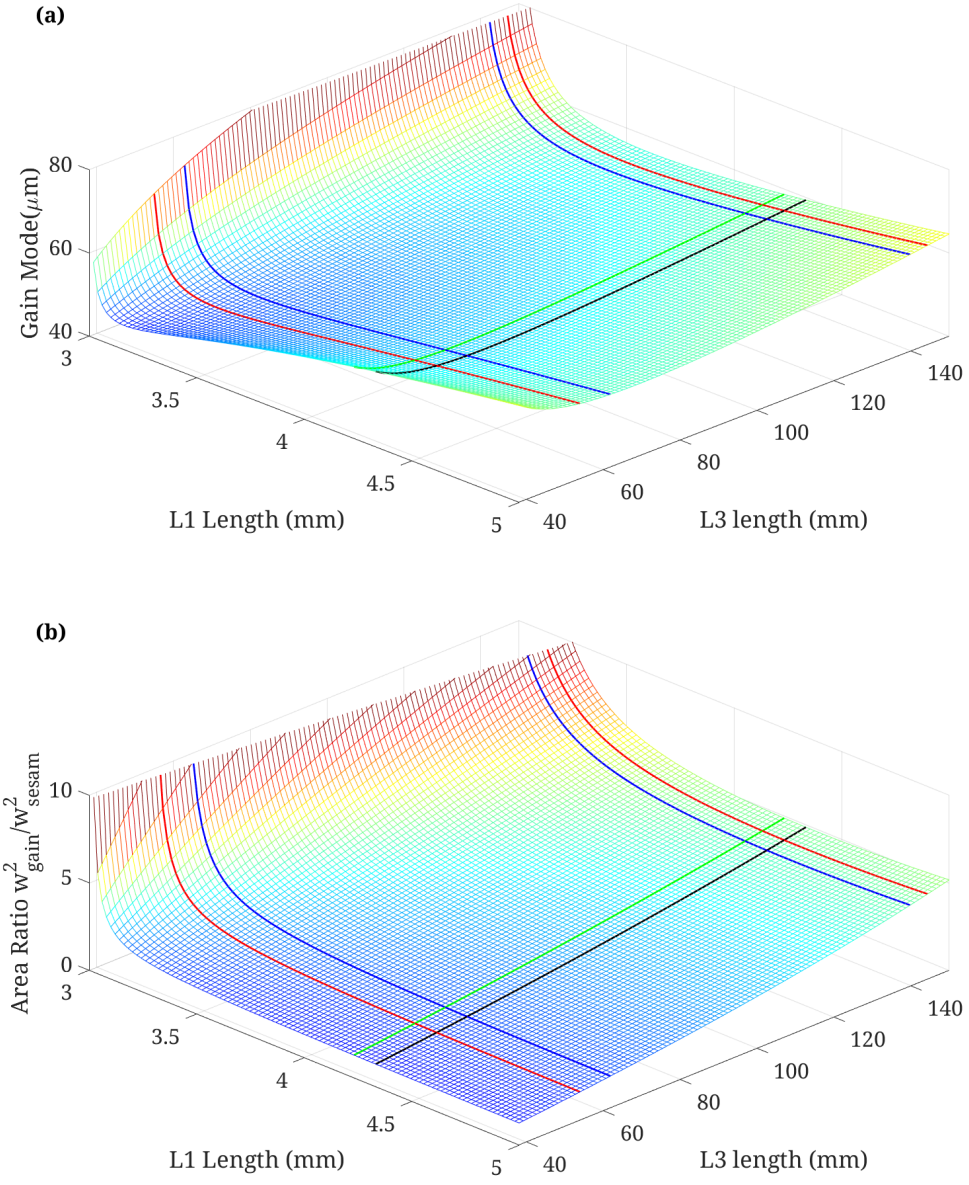

Figure 2.12: *Output from beam waist calculation for tZ-cavity as a function of changes in L_1 and L_3 for a fixed L_2=22 mm (Shown in Fig.2.11). (a) Gain mode radius in μm and (b) Area-ratio between the gain spot size and the SESAM mode (Shown in Appendix.B). Calculation also displays (green) the lowest gain spot size variation and (black) the lowest area ratio variation. Experimentally obtained tunability ranges are plotted for: (red) 1-W tZ-cavity, 0.880-1.880 GHz ,and (blue) 6-W tZ-cavity, (0.9-1.7 GHz).*

Min std. dev.	Gain-mode		Area-Ratio	
L_1 (mm)	4.2		4.4	
L_3 (mm)	53.8	144.3	53.8	144.3
Gain-mode (μm)	53.2	58.2	53.9	58.9
SESAM-mode (μm)	40.6	27	41.4	27.4
Area-ratio	1.7	4.6	1.7	4.6

Table 2.3: *Calculated Gain and SESAM mode-waists and area-ratios for the lowest standard deviations of gain-mode and area-ratio. L_3 range corresponds to the result presented in Sec.2.3.2.*

$$M_{resonator} = \begin{array}{l}[M_{SESAM}M_{L_1}M_{Gain}M_{L_2}M_{FM}M_{L_3}M_{OC}]_{SESAM-OC} \\ [M_{L_3}M_{FM}M_{L_2}M_{Gain}M_{L_1}M_{SESAM}]_{OC-SESAM}\end{array} \tag{2.1}$$

Where M_i is the beam propagation matrix for the ith element, shown in Fig.2.11. The result of the ray transfer matrix calculation is,

$$M_{resonator} = \begin{bmatrix} A & B \\ C & D \end{bmatrix} \tag{2.2}$$

where A, B, C and D can be used to evaluate the laser mode in the cavity (as shown in Appendix.B. The surfaces in Fig.2.12 are formed by evaluating for a fixed L_2 which has been determined iteratively by finding the lowest standard deviations for gain-mode radius (green) and area ratio (black), while keeping the gain spot size large enough to overlap with the optical pump efficiently. Therefore, the surfaces and the two plotted lines display the largest stable range of cavity length change (ΔL_3) for a given separation of Gain structure and SESAM (L_1). The intracavity mode size for the middle of the tuning range is shown in Fig2.11, along with the folded-out cavity. In this figure we can see that a similar mode size variation to a V-cavity up to the fold mirror (Fig.2.9); if we had a V-cavity formed by SESAM, gain-structure and OC of half the RoC of the FM in the tZ-cavity we would achieve approximately the same gain spot size and area ratio, making a V-cavity test as was performed with the 1μm structures a reasonable result to discount those structures for tZ-cavity experimentation.

Min std. dev.	Gain-mode		Area-Ratio	
L_1 (mm)	4.2		4.4	
L_3 (mm)	61.7	139.8	61.7	139.8
Gain-mode (μm)	52.8	57.8	53.5	58.4
SESAM-mode (μm)	38.1	27.4	38.8	27.8
Area-ratio	1.9	4.5	1.9	4.4

Table 2.4: *Calculated Gain and SESAM mode-waists and area-ratios for the lowest standard deviations of gain-mode and area-ratio. L_3 range corresponds to the result presented in Sec.2.3.3.*

Using the code to produce the tunability plots shown in Fig.2.12(a & b), it was determined that a cavity length L_1 = 4.4 - 4.2 mm provides the longest range of cavity length L_3 at a length L_2 = 22 mm. Experimentally, cavity lengths may be measured to approximately ±0.5 mm, so this may be used as a rough constraint on cavity design; to determine real cavity-length tunability the cavity length L_3 was varied and kept lasing over long ranges, and L_1 and L_2 were iteratively varied to maximise the stable ΔL_3. The final result was a tunable range of: ΔL_3 = 9.1 cm for the P_{avg} = 18 mW case, and ΔL_3 = 7.8 cm for the P_{avg} = 50 mW case (full conditions for both are discussed later in this section).

2.3.2 Mode-locking at 1 W of Optical Pump

The tZ-cavity was also built with new samples to address the limitations of the gain-structure V628 and SESAM V629 used for the 1-μm AR Z-cavity discussed in Sec.2.2. The primary limitation of the V628 and V629 was their power handling capabilities, which limits their performance in both power scalability and pulse duration. The structure-pair that was selected to replace them were H29 and V623, described in Sec.2.1.2.

A further experimental design constraint of the tZ-cavity was that the cavity angles must be kept low to reduce laser mode astigmatism. Therefore small-width copper heat sinks were designed to allow closer proximity of cavity elements. However, the smaller Peltiers required for these mounts were limited to 20 W of heat extraction (compared to the 50 W that the other VECSEL cavities were able to use). The reduced rate of

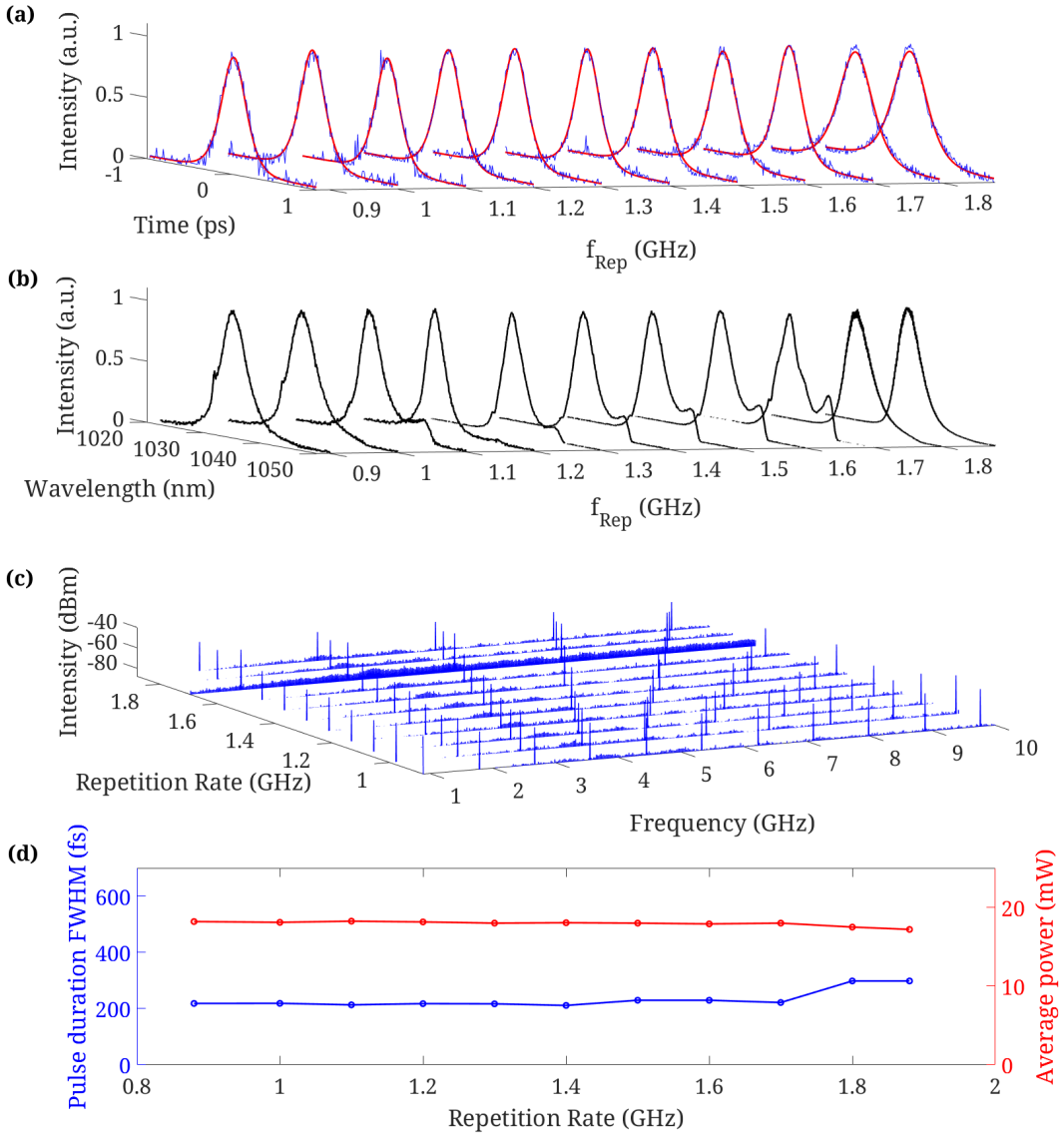

Figure 2.13: *Pulse characterisation for the 1035-nm (H29 and V623) VECSEL tZ-cavity pumped by a 1 W of 808-nm diode laser (a) Intensity autocorrelations as a function of repetition frequency (blue) with sech^2 data-fits. (b) Optical spectra as a function of f_{Rep}. (c) RF spectra as a function of the repetition frequency. (d) (blue) pulse durations retrieved from sech^2 fit to the data in (a), (red) average power recorded as a function of f_{Rep}.*

heat extraction reduced the "thermal rollover" threshold, limiting the VECSEL output power.

The first iteration of the tZ-cavity VECSEL was pumped with 1 W from an 808-nm diode laser focused to a 101-μm pump spot, and was built with a 0.3%-transmission planar OC. The characterisation of the pulse train produced by this laser is shown in Fig.2.13. The intensity autocorrelations were fitted to hyperbolic secant functions and plotted as a

function of repetition frequency. This showed that the VECSEL produced approximately 215-fs pulses across the majority of the tuning range (Fig.2.13(a & d blue)), except beyond f_{Rep}=1.7 GHz where it increased up to 400-fs before the laser was no longer stable. The optical spectra as a function of repetition frequency show that the spectrum has a "shoulder" on the long wavelength side, indicating high order phase structure (Fig.2.13(b)). The high order phase structure present in the pulses from this laser has been previously reported by Head et al. (2016). Fig.2.13(c) displays the RF spectra as a function of the first recorded harmonic peak. Each of the recorded spectra show stable peaks of approximately equal intensity up to 10 GHz. Finally, the average power and the pulse durations extracted from hyperbolic secant fits to intensity autocorrelation data are plotted as a function of repetition frequency Fig.2.13(d), displaying the tuning stability of the laser output.

The experimental limits on continuous laser tunability were found to be at 0.88 GHz and 1.88 GHz. At the lower limit on repetition frequency the laser transitioned to a multi-pulsing regime where the autocorrelation was unstable and increased to approximately 300 fs and the repetition frequency switched to double the frequency corresponding to the cavity length (approximately 1.6 GHz). This was attributed to sufficient gain recovery between pulse round-trips to support another pulse. At the high frequency limit of the repetition frequency the pulse durations increase up to 400 fs before the VECSEL no longer lased at all, this is attributed to large area-ratio and gain-mode changes for short L_3 as shown in Fig.2.12, as the limit on lasing will correspond to large changes in the gain-mode/pump-spot overlap.

2.3.3 Mode-locking at 6.6 W of Optical Pump

The second iteration of the tZ-cavity was pumped with up to 35-W of 808-nm light from a bar diode-laser focused to a 129-μm pump spot, and was optimised at a pump power of 6.6 W. The laser OC was switched from the first iteration to a 1%-transmission planar OC. The change in pump power was made to increase the output power of the VECSEL for use driving nanostructures as shown in Chapter.5.

Pump Power (W)	**1.0**	**6.6**
Pulse length (fs)	215-400	240-290
Wavelength (nm)	1035	1035
Wavelength FWHM (nm)	5 - 7.5	5 - 7.5
F_{rep} (GHz)	1.38±36%	1.34 ±28%
ΔF_{rep} (GHz)	0.88 - 1.88	0.96 - 1.72
Transform limit	1.4 - 1.8 ($\beta = 0.5 - 0.6$)	1.6 - 1.9 ($\beta = 0.5 - 0.6$)
Average Power (mW)	18-17	51-47
Pulse Energy (pJ)	20-9	53-27
Peak Power (W)	95-23	221-94

Table 2.5: *Pulse train characterisation for the 1035 nm AR Z-cavity VECSEL built with H29 and V623. Both characterisations for 1 W and 6.6 W of optical pump.*

The characterisation of the high power tZ-cavity is shown in Fig.2.14. Intensity autocorrelations showed clean pulse shapes limited by noise, the autocorrelations were fitted to hyperbolic secant profiles retrieving pulse durations of 240-290 fs (Fig.2.14(a & d blue)). Repetition frequency tunability for this iteration of the tZ-cavity was shown to be 960 MHz - 1.72 GHz via RF spectra (Fig.2.14(c)), the RF spectra show stable harmonics of approximately equal intensity up to 10 GHz. Optical spectra, shown in Fig.2.14(b), display a pronounced shoulder, on the red-shifted side of the main 1035-nm peak. This feature was attributed to the same phase structure observed for all VECSEL outputs produced by the sample pair H29 and V623.

The larger pump power reduced the tunable range of the VECSEL, this was attributed to a number of factors relating to the increased intracavity power and larger pump optics. The optical pump spot was not optimised to the cavity mode, the mismatch between the gain-mode and the pump mode was due to requiring larger collimation and focusing pump optics for power handling which increased the pump spot to 150 μm. A larger pump spot meant that mode-matching at lower pump powers was poor hence increasing the operational pump-power for mode-locking (from 1 to 6.6 W). Increasing the pump power also limited the range over which the SESAM could modulate the intracavity power, the effects limiting stability shown for the 1-W tZ-cavity were exacerbated by the increase in power. At low repetition frequencies the complete modulation of large intracavity power was not possible and this added to the limitation of carrier lifetime

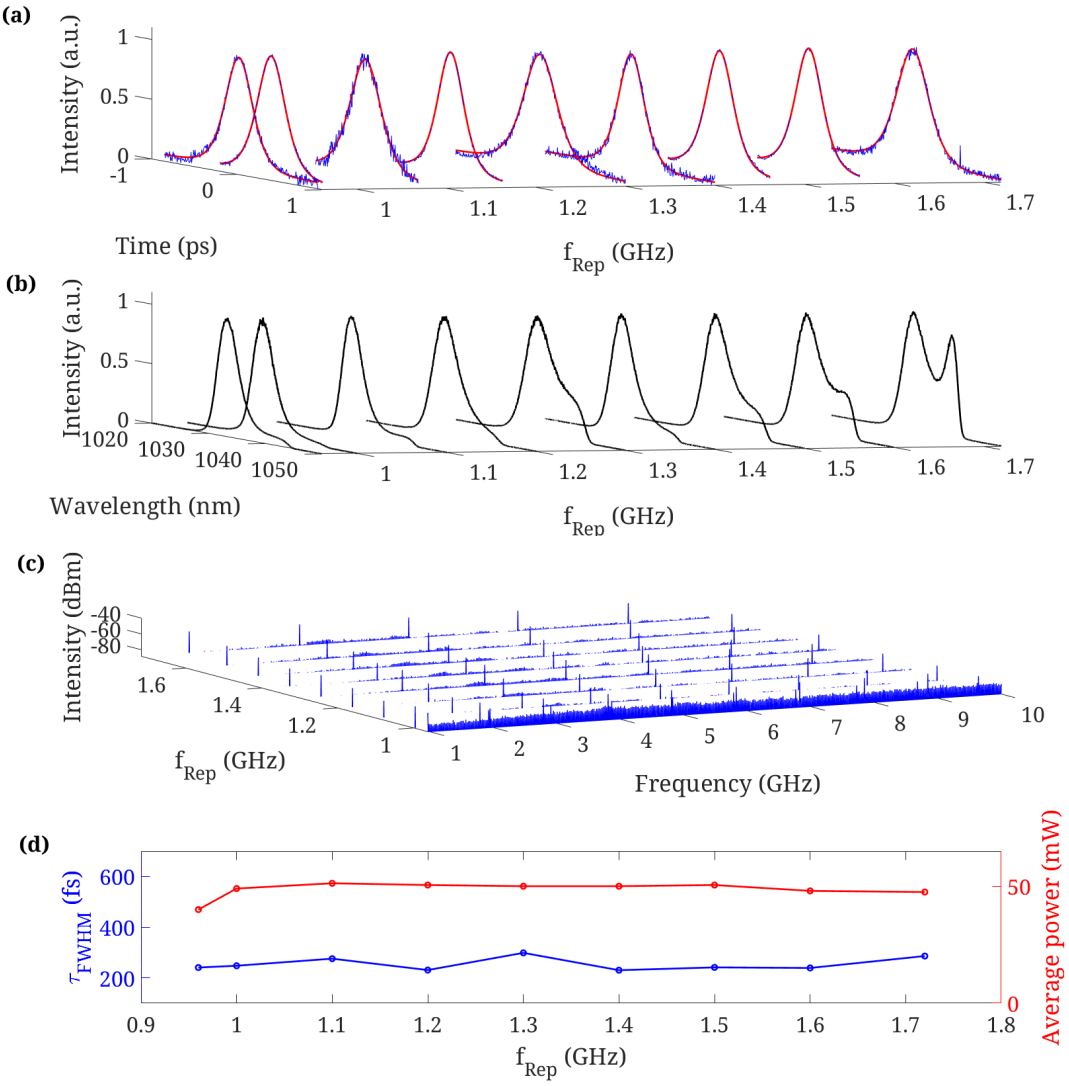

Figure 2.14: *Pulse characterisation for the 1035-nm VECSEL tZ-cavity pumped by a 1 W of 808-nm diode laser (a) Intensity autocorrelations as a function of repetition frequency (blue) with sech^2 data-fits. (b) Optical spectra as a function of f_{Rep}. (c) RF spectra as a function of the repetition frequency. (d) (blue) pulse durations retrieved from sech^2 fit to the data in (a), (red) average power recorded as a function of f_{Rep}.*

meaning multi-pulsing occurred At high repetition frequencies, the SESAM cannot saturate enough at the lower area-ratios, again limiting mode-locked range on tunability. In addition, a related effect was recorded where the VECSEL operating well within its tuning range at 1.3 GHz, would multi-pulse at double the cavity repetition frequency when pump power was increased by 0.2 W (to a total of 6.8 W) again attributed to enough available gain between round-trips to support an additional pulse circulating in the cavity (similar to the effect seen at low repetition frequencies).

2.4 Conclusions

In this chapter I have presented the characterisation of the first sub-300-fs VECSEL to demonstrate over 70% repetition frequency tunability close to 1 GHz.

First it was shown that an AR structure design paired with a suitable surface recombination SESAM produced stable sub-300-fs pulse trains at approximately 1-GHz repetition frequencies . The pulse formation was heavily dependent on area-ratio between gain spot size and SESAM-mode, requiring an area-ratio of 5:1. This limitation on mode-locking constrains the cavity design to a traditional Z-cavity, as this cavity can independently vary the gain-mode and SESAM-mode. Therefore the 1-μm structures could not be used to construct a tunable VECSEL as the tZ-cavity required for tunable repetition frequency mode-locking would be unable to achieve the area ratio to saturate the 1-μm SESAM.

A design protocol described here (and expanded upon in Appendix.B) was developed to optimise performance of VECSELs. This design protocol, based on mode calculations, may be applied to any cavity configuration, but was used to optimise tZ-cavity length changes for the smallest variation of gain-mode and area-ratio. The cavity designs were successfully applied to two iterations of tZ-cavity.

The first iteration of the tZ-cavity VECSEL has shown that a stable 215-400 fs pulses of 1035 nm can be produced over a 9 cm cavity length change equivalent to 880 MHz - 1.88 GHz (Δf_{Rep}=1 GHz). This tuning range is currently limited by: fold mirror placement and output coupler translation stage. By moving the fold mirror (or switching to a different RoC) it will be possible to change the stable cavity length range.

The second iteration of the tZ-cavity VECSEL increased the output power of the laser from 30 mW to 50 mW, but at the expense of minor changes to pulse duration and repetition frequency tunability. The reduction of tunability at high powers is given by limitations on: carrier lifetime for low repetition frequencies and SESAM saturation for high repetition frequencies . Both would require modifications to be made to the structure designs to extend this range to high power at this repetition frequency.

Further conclusions, design changes and future work are discussed in Chapter.7.

Chapter 3

Semiconductor Nanowires for GHz Acoustic response

Semiconductor nanowires are a well understood and fabricated nanostructure. The very high light-scattering properties of nanowires are highly desirable for thin-film light interactions, making these nanostructures applicable to light emission and sensing, in a number of fields as varied as biosensing (Gao et al. (2007)) and renewable energy (Fitriani et al. (2016)).

Semiconductor materials are vital for electronics and light matter interactions, but can be further improved by increasing the scattering properties using nanoscale structures. Semiconductor growth can also be perfected for a number of nanostructure geometries. In this research, the property that has been of interest is the mechanical oscillations of these nanostructures. The nanowire may be modelled as an oscillating cantilever with equal thickness and width, bound at one end; this will result in acoustic modes corresponding to bending, extensional and torsional movement.

3.1 MOVPE/VLS Nanowire Fabrication

These structures were grown by Muskens et al. (2009) via metal-organic vapour phase-epitaxy (MOVPE) Muskens et al. (2008) Muskens et al. (2009). The available samples

are grown onto a silica slide with 300 nm of GaP substrate. The GaP nanowires were grown with a combination of vapor-solid-liquid (VLS) and lateral growth processes to tune length and diameter independently, so that the diameter did not depend on length for a fixed material density. First GaP substrates were prepared by wet etching with a mixture of HNO_3:HCl:H_2O at 80 °C and a 0.3-nm layer of gold was deposited onto the [111] sample surface. Once prepared, the substrates were placed in an MOVPE machine and held at low pressure and high temperature. TriMethylGallium (TMG) and Phosphine (PH_3) were introduced to the chamber to deposit as GaP. Radial nanowire was induced at higher temperatures, while VLS growth promoted nanowire length growth. A complete record of fabrication conditions is described in Muskens et al. (2009).

3.2 Nanowire Characterisation and Simulation

Fig.3.1 shows SEM images of the GaP nanowire sample under study. The nanowires are shown to be [111]-growth GaP nanowires of 2.3 μm length and approximately hexagonal cross sections with diameters of 160-190 nm, a taper in cross-section is visible from tip to base of approximately 30%, therefore base diameter of (110-133 nm). Due to the growth

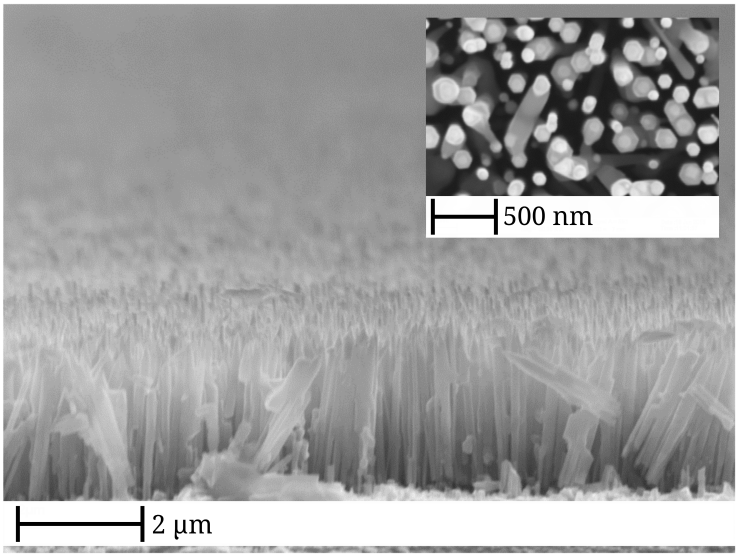

Figure 3.1: *SEM images of the nanowire sample used for experimentation in this report. Side view SEM of GaP [111] nanowires of 2.3 μm length and (Inset) top-down view SEM showing approximately hexagonal diameters of 160-190 nm.*

procedure of these nanowires the wires are subject to irregularities such as coalescing from the shell growth into compound nanowires of twice the design thickness.

Electrostriction, opto-thermal and carrier recombination (Sec.1.2) are the mechanisms by which the acoustic modes can be excited in semiconductor for an intense driving pulse. Therefore, the semiconductor material will react non-linearly producing excited carriers to the intense driving pulse, as long as the driving pulse is at the correct wavelength and intense enough. For highly-scattering GaP nanowires, the mechanism for carrier generation has been used previously to excite the nanostructures and harnessed to measure the acousto-optic response via the modulation of nonlinear reflectivity from excited carriers (Mariager et al. (2010), Mante et al. (2012)).

The shape of mechanical resonances for nanowires will match those of a vibrating rod bound at one end. The frequency of these modes can be calculated via Finite Element Method (FEM) Analysis.

3.2.1 Finite Element Method Analysis for Acoustic Mode Simulation

Finite Element Method Analysis is a technique which solves partial differential equations for a system, using weak-form constraints on boundaries. This is done as opposed to strong form equations as they may not be efficient or output classical solutions, since continuous boundary conditions are required particularly for complex domains or material-material interfaces, making weak formulation more appropriate for potential discontinuities in the material geometry. The finite element method divides a geometry under study into a mesh of sub-domains, each with a small volume compared to the geometry. The weak formulation of model constraints is applied but may allow for discrepancies, increases of mesh size may improve accuracy, but must be balanced against the model taking an unnecessarily long time to compute. For this research, the COMSOL structural mechanics module was applied, specifying the use of Physics for Solid Mechanics in 3D. This made it possible to calculate mechanical eigenfrequencies for the geometry and materials selected for study. The output from this analysis is a eigenvalue which can be expressed as a complex eigenfrequency which takes into account damping as loss. First the fixed boundaries were made static, for the nanowires the nanowire

base, and for the nanocantilevers the domains excluding the cantilever. To simulate vibration an instantaneous boundary load was added to the tip face of the nanowire and cantilever respectively.

A limitation highlighted by the development process of this modelling was the dependence on the geometry under study. The model was compared to data from the paper by Mante et al. (2012), where their model provided eigenfrequencies comparable to their frequency. The results of modelling are presented in Sec.3.2.2 and Sec.4.3.

3.2.2 Semiconductor Nanowire Extensional Modes

For nanowires, extensional acoustic modes can be detected experimentally due to their strong the dependence on length and Young's modulus only. By contrast, the breathing and bending modes depend heavily on the dispersion and inhomogeneous broadening will lead to difficulties in detection of such modes Mante et al. (2012). Other modes, such as whispering gallery modes and torso-radial modes have lower Q-factors and will not be detected. Based on FEM analysis and parameter sweeps, extensional mode frequency

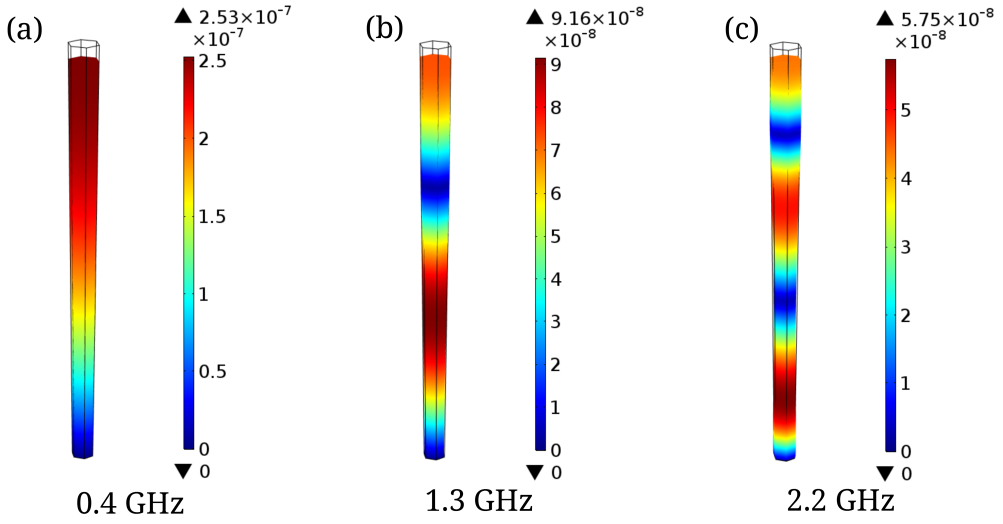

Figure 3.2: *Surface displacement simulations for a GaP nanowire: 80 nm radius, 2.3 μm length. The nanowire cross-section is hexagonal and there is a taper from tip to base from 80 nm to 60 nm. The displayed modes are (a) 1st, (b) second and (c) third order extensional modes, and are shown with theoretical surface displacement to show relative displacement. The calculated eigenfrequencies are (a) 0.4 GHz, (b) 1.3 GHz and (c) 2.2 GHz.*

will depend most strongly on nanowire length and to a lesser extent, on diameter; the diameter will most strongly influence the Q-factor of the resonance and the displacement.

Theoretical extensional modes have been calculated via FEM for the samples shown in SEM (Fig.3.1). The theoretical eigenfrequencies (displayed in Fig.3.2) correspond to the n=1-3 extensional modes of the GaP nanowire geometry. The 2nd order mode (1.3 GHz) lies within the range of the repetition frequency tunability demonstrated in both Sec.2.3.2 and Sec.2.3.3, while the 1st (0.4 GHz) and 3rd (2.2 GHz) are just outside the tunable range. This meant that the 2nd order mode was directly targeted, and the 3rd order mode may be excited via sub-harmonic excitation at 1.1 GHz. FEM estimated Q-factors for these modes of 100±0.4, however this estimate does not account for gas surrounding the structure and inhomogeneity in the sample.

3.3 Experimental Methods

3.3.1 Vacuum Chamber

To suppress the interaction with gas molecules surrounding the nano mechanical samples, a vacuum chamber was designed to fit into existing optical setups. The chamber thickness was limited by the working distance of the microscope objectives used, therefore long working distance (1.2 cm) objectives were selected. The chamber was able to isolate a nanostructured sample at low pressure, $1.1 \cdot 10^{-3}$ mbar. To access the sample, two 1-mm thick 25.4-mm diameter transmission windows, anti-reflection coated for 650-1050 nm, were placed either side of the sample. The chamber was pumped down with a rotary vane mechanical vacuum pump, connected via a plastic tube. The plastic tube was necessary to reduce transmission of mechanical vibrations from the vacuum pump to the vacuum chamber and thereby the sample. The plastic tube increased the minimum achievable vacuum pressure from that possible with a metal tube ($\approx 1 \cdot 10^{-4}$ mbar).

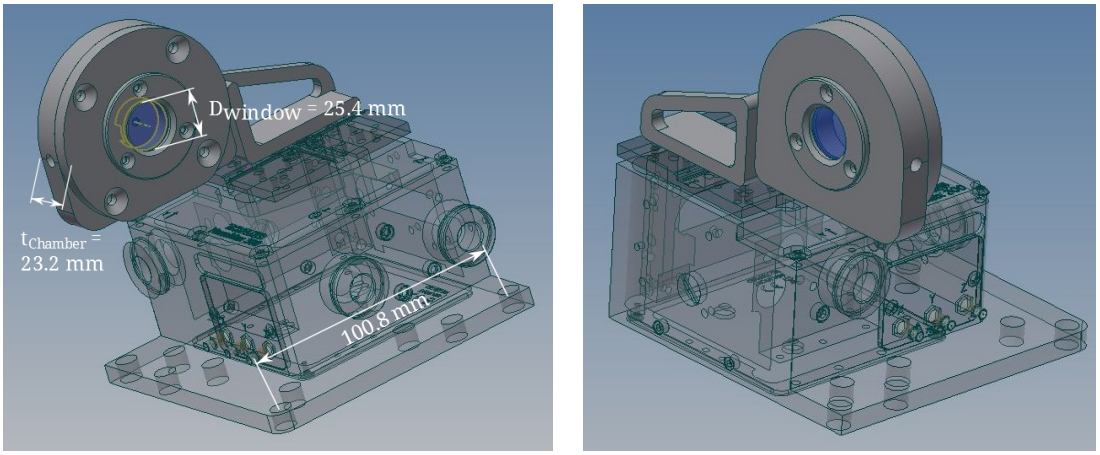

Figure 3.3: *3D renders of the low thickness vacuum chamber for holding the samples under low vacuum of approximately* $1.1 \cdot 10^{-3}$ *mbar. Also shown, is the 3D-translation stage (transparent) for sample positioning. The chamber windows were anti-reflection coated for 650-1050 nm and were: 25.4 mm diameter, and 1 mm thick. The total chamber thickness is 23.2 mm, and the sample is held approximately in the centre of this range (at 11.6 mm).*

3.3.2 Time-Domain Pump-Probe Spectroscopy

To measure transient optical reflectivity and transmission a time domain spectroscopy pump-probe experiment was built (shown in Fig.3.4), using an 184-fs Yb:KGW fibre laser (characteristics in Table.3.1). This setup split the output from the fibre laser into two beams via SHG and dichroic mirrors to drive the nanostructures at 517 nm and probe their response at 1035 nm. This was performed by focusing the fibre-laser output into a potassium titanyl phosphate (KTP) crystal and separating pump (green) and probe beams (IR), and the 1000-nm long pass (LP) dichroic mirror. Then the pump

	Yb:KGW	Supercontinuum
Pulse length (fs)	184	9000
Wavelength (nm)	1035	400-2000
Wavelength FWHM (nm)	11.5	20 (slit width)
Rep. Rate (MHz)	75.5	20
Transform limit	1.34 (β=0.592)	-
Average Power (W)	1	1
Pulse Energy (pJ)	13	50
Peak Power (W)	71	5

Table 3.1: *Beam characteristics for the Yb:KGW 184-fs fibre laser and MOPA supercontinuum laser.*

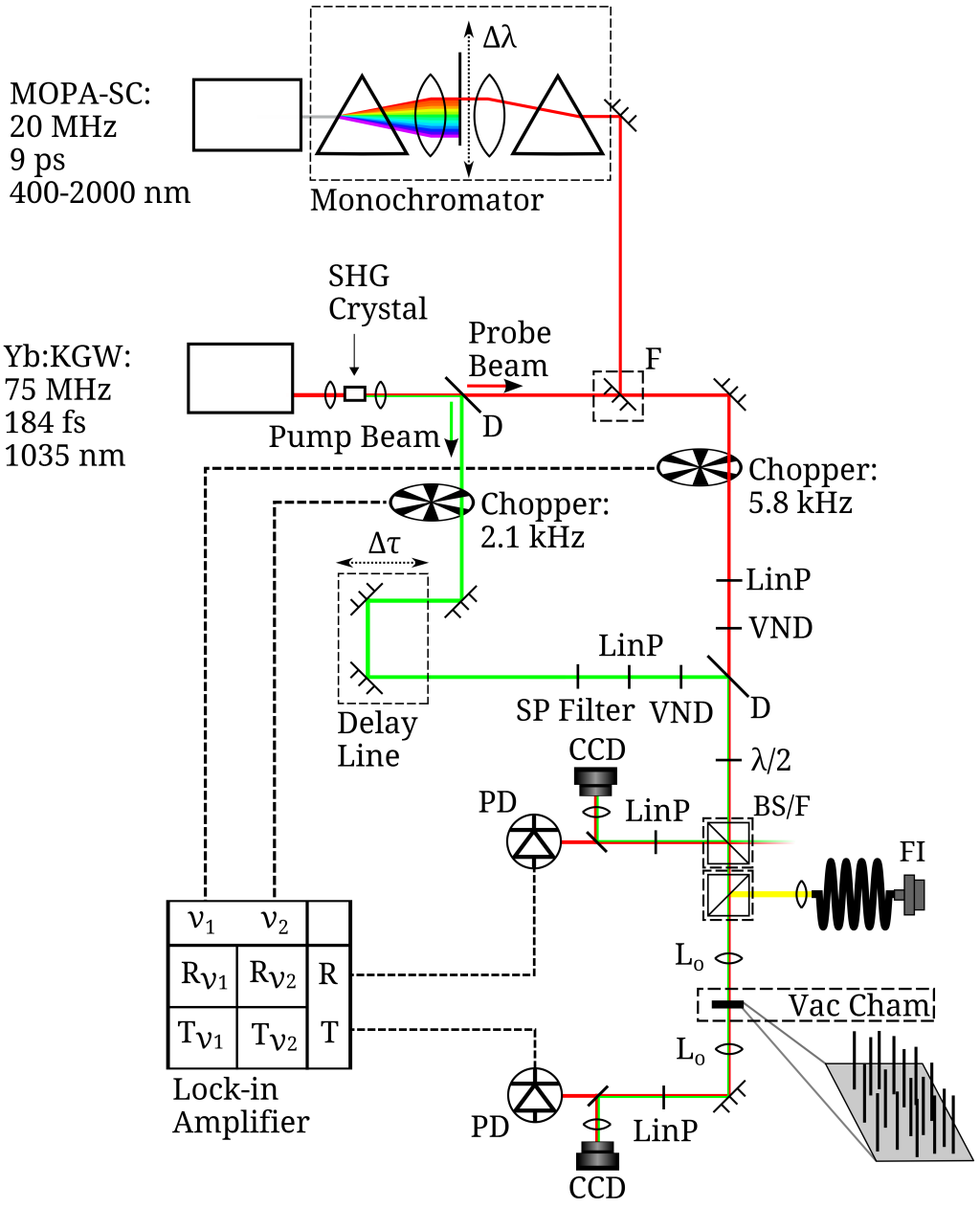

Figure 3.4: *Setup used for both linear spectroscopy and pump-probe spectroscopy for nonlinear time-domain reflectivity and transmittivity. The sample is tested and imaged with a pair of microscope objectives, illumination provided by a white-light fibre-illuminator FI, a vacuum chamber can be included to isolate the sample under test. The setup for linear reflectivity is performed by scanning the output wavelength of the dispersive monochromator, the output was modulated by the chopper up to 6 kHz, and th beam is polarised and rotated with a linear polariser LP and half wave plate λ/2. The setup was built to allow switching to nonlinear time-domain pump-probe spectroscopy, with a long variable delay line (up to 6 ns/1.8 m). In time-domain spectroscopy the output from a Yb:KGW fibre laser (184 fs, 1035 nm, 75 MHz) is frequency-doubled and split into 1035-nm probe and 512-nm pump beams.*

beam passed through an optical chopper at 2.1 kHz and passes through to a 30-cm delay line with retro-reflectors for 6 passes and a total path difference of up to 1.8 m. Finally the pump beam passed through a short pass (SP) filter to remove any remaining IR, and a variable neutral density filter (VND). The IR probe beam passed through a 5.8-kHz optical chopper and a second VND for independent power control to the pump beam. The probe beam was then recombined with the pump beam at a second dichroic mirror. Both beams were aligned to travel co-linearly and are focused onto the nanostructure held in the vacuum chamber (described in Sec.3.3.1). To focus the beams onto the sample, two 50x Cassegrain objectives were used (WD= 12 mm, NA= 0.5). The spot size radius of the pump and probe beams were approximately 2 μm. A Cassegrain objective uses mirrors instead of lenses to achieve higher throughput efficiency at a wider wavelength bandwidth. It does however clip the central portion of the beam (in the case of those used here $\approx$30%), leaving a cone of incident radiation on the sample. In addition the tight angle of focus may have affected the reflection and transmission signals. Two CCDs were used to overlap the pump and probe beams and select nanostructure regions of interest, imaging the nanostructure was performed with a white light fibre illuminator (FI). The pump and probe beams were polarisation controlled using linear polarisers (LinP) and half waveplates ($\lambda/2$). The polarisations could therefore be set to parallel or cross-polarisation for additional pump beam rejection, and the probe polarisation cold be optimised for polarisation sensitive structures. The pump and probe beam powers were set to P_{pump}= 0.6 mW and P_{pump}= 0.4 mW respectively.

The reflected and transmitted probe beams were sent to two photodiodes with LP filters to eliminate the pump beam for detection. Finally, in addition to the filtering of all signal except the probe beam, lock-in amplification was applied. The type of lock-in amplifier used in this experimentation is a: Scitec instruments 4450DV2 Dual Channel DSP Lock-In Amplifier. The dynamic reserve of this system is 100 dB allowing a signal to be recovered from noise 10^6 times larger. This lock-in amplifier has 16 demodulation channels using Digital Signal Processing (DSP), allowing 16 independent outputs demodulated with combinations of the two reference frequencies ν_1 = 5.8 kHz and ν_2 = 2.1 kHz. In this experiment separate demodulation channels were used to analyse the reflection and transmission channels independently. It also separately demodulates

the channels with up to two reference frequencies. Resulting in four outputs: R and T demodulated with ν_1 and R and T demodulated with ν_2. The channels demodulated by ν_1 are designated: ΔT and ΔR and those demodulated by ν_2 are T and R. The quotient of the two channels for each photodiode ($\Delta T/T$ and $\Delta R/R$) is then calculated in a Labview interface. In this experiment, after the demodulation of signal low pass filters were applied to the demodulated signal at a time constant of 200 ms for fast scans and 1 s for longer scans. For a slow varying signal the 1/f noise (where f is reference frequency) will be the primary source of noise, which falls with increasing f. Hence, for detection of a small optical signal it is necessary to have a fast reference for modulation, in this case the kHz choppers.

3.3.3 Linear Spectroscopy

In addition to characterisation in the time-domain, the setup shown in 3.4 was reconfigurable for linear spectroscopy in wavelength. Linear spectroscopy measurements were performed using a Master Oscillator Power Amplifier (MOPA) supercontinuum source using the probe beam chopper and blocking the time-domain setup pump and probe beams. The emission of the supercontinuum source was a pulse train of 9-ps pulse duration spanning a wavelength range of 400-2000 nm at a repetition frequency of 20 MHz. The supercontinuum was used with a double-prism subtractive mode monochromator, where the beam is first dispersed by a prism and then focused onto a slit for selection of a specific wavelength. A second lens and prism were used to recombine spectral components after filtering. The probe beam could therefore be tuned with a resolution of up to 20 nm. The pulsed output from this laser was not used to make time dependent measurements, instead it was used for linear reflectivity and transmission characterisation using empty space and a gold reflector for normalisation of spectra.

3.4 GaP Nanowire Results

3.4.1 Linear Spectroscopy Results

Fig.3.5 displays the reflectivity and transmission measurements performed for the nanowire sample, performed with the setup described in Sec.3.3.3. The transmission trace displays a broad decrease in transmission toward short wavelengths, corresponding to scattering recorded in Muskens et al. (2009). The recorded transmission value at the tZ-cavity VECSEL wavelength was T_{1035nm}=0.46, the remaining radiation is reflected, absorbed or scattered by the sample. The reflection trace for this sample also displays a reflection value R_{1035nm}=0.10 and the same trend shown by transmission, with the exception of a peak close to 1030 nm corresponding to the seed pulse for the supercontinuum. The dominant effects in this measurement were the low reflectivity of the sample, due to large scattering angle and membrane misalignment strongly affecting the reflection signal. The reflection values are also lower than those in transmission due to the strong dependence on scattering and absorption, rather than bulk reflection. The results displayed here were used to conclude that transmission would be more reliable for measurements in Chapter.5.

3.4.2 Time-Domain Results

GaP response to above-bandgap excitation with a pump-probe is well documented and results from absorption of pump by free carriers, which are excited to the conduction-band. The band-gap energy of GaP is $E_{G,GaP}$= 2.26 eV, corresponding to 548.6 nm. The nonlinear response was then measured, indirectly, by its effect on the probe beam. The temporal evolution of carrier population of GaP displays as a transient absorption which decays over a period of nanoseconds. The reflectivity transient will also be modulated by the vibrations of the nanostructure.

The result of time domain characterisation is shown in Fig.3.6. The reflection and transmission transients are shown over a 6-ns scan range, where the primary feature

recorded was nonlinear absorption. The nonlinear response of the nanowires follows an exponential decay with fast and slow components, therefore the expected trend will be

$$\Delta R/R = R_0 + A_1 e^{(-t/\tau_1)} + A_2 e^{(-t/\tau_2)} \tag{3.1}$$

where,$\Delta R/R$ is the measured reflectivity, R_0 is the linear reflectivity, τ_1 and τ_2 are the fast and slow constants of the decay, and A_1 and A_2 are the relative amplitudes of the decay constants. This trend also applied to transmission $\Delta T/T$ with an offset T_0 for linear transmission. The result of fitting showed that the retrieved carrier relaxation time constants in reflection were: τ_1=2.0 ns (A_1=6.9 $\times$ 10^5) and τ_2=8.3 ns (A_2=6.9 $\times$ 10^4). In transmission, the τ_1=2.2 ns (A_1=2.2 $\times$ 10^6) and τ_2=5.1 ns (A_2=6.9 $\times$ 10^4). The large discrepancy in τ_1 is attributed to the large amount of noise present at timescales close to pump-pulse arrival at the nanowires, t= 0 ps. The noise present at timescales close to t=0 ps also causes fitting inaccuracies in τ_2, as τ_1 and τ_2 will be coupled in the fit making distinguishing them difficult. The residuals from the exponential fit to the transients are displayed below. These do not show an obvious temporal effect modulating the decay, however, there is a noisy response from 1 - 2.5 ns, as well as a longer timescale oscillation

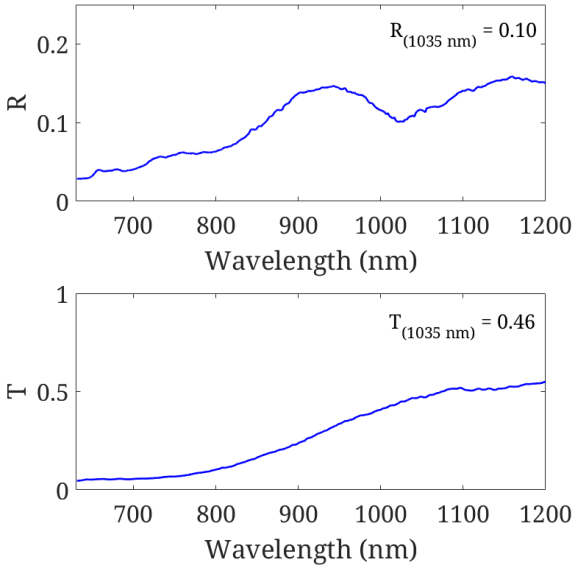

Figure 3.5: *Normalised reflectivity and transmission, for the GaP nanowire sample described in Chapter.3. Absorption and scattering increased toward shorter wavelengths and reflectivity and transmission at 1035 nm was R= 0.1 and T=0.46 respectively.*

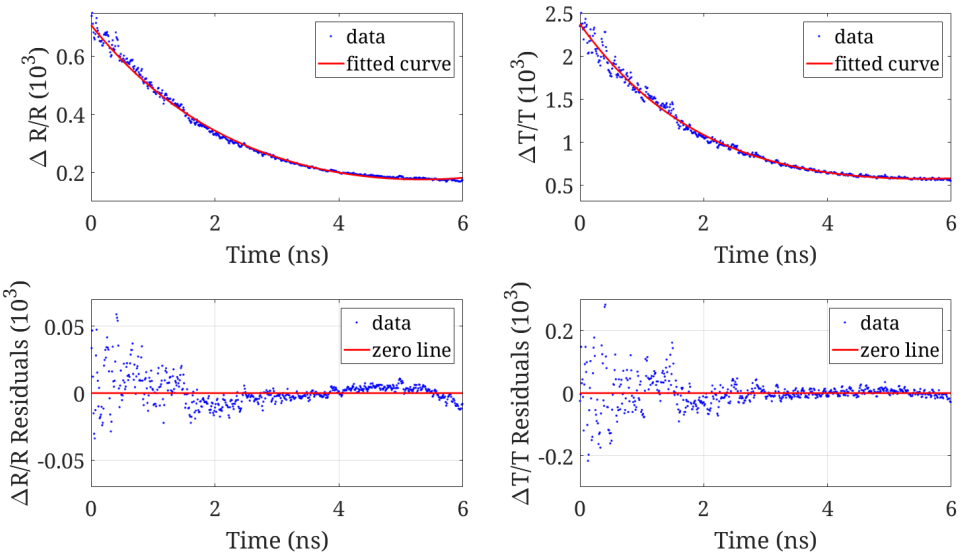

Figure 3.6: Reflectivity and transmission transients for GaP nanowires. Data is displayed as ΔR or ΔT (demodulated at the probe frequency) divided by R or T (demodulated at the pump frequency) to show transients independent of pump power variation. Both are fitted to 2nd order exponential functions (Exp2) to retrieve the residuals for analysing acoustic response.

from 2 - 6 ns. The first occurs with a single cycle over 1.4 - 1.7 ns corresponding to a 1.39 GHz oscillation. The second oscillation occurs over 2.2 - 4.8 ns, approximately 188 MHz. However, if the oscillation is acoustic it would be expected to have opposing sign in reflection and transmission respectively. In addition, the secondary oscillation may be a result of inaccuracies of the exponential fit.

The analysis in Sec.3.2 showed that the nanowires under study are expected to have extensional modes at 380 MHz, 1.3 GHz and 2.2 GHz. The second order extensional mode may correlate with the observed oscillation to within variations across the nanowire sample, however, without resonant control the modes should be excited proportionally to the predicted displacement.

3.5 Conclusions

In this chapter the transient absorption of semiconductor nanowires has been measured, showing the decay of carriers from above-band-gap excitation. The decay occurs over a

period of ns, and was intended to be used to retrieve mechanical vibrations as modulations of reflectivity or transmission on the transient absorption, excited by the same optical pulse that generates carriers.

The absorption transients display the expected exponential decay of carriers, occurring over a period of ns. The modulation of reflectivity/transmission/scattering that was expected at the resonance frequencies of 380 MHz, 1.4 GHz and 2.2 GHz, was not retrieved from the exponential fit and noise of the transient. There was however a significant amount of noise at the beginning of the transient and modulation over the 6-ns time period.

As has been noted in previous research, time-domain acoustic interrogation will be limited in signal to noise by the delay line, which will introduce beam pointing variations and mechanical vibration. These factors contribute to the signal to noise ratio of the signal; coupled with the high frequency of acoustic resonance of these structures and the inhomogeneity of the samples, the transient was heavily dependent on sample position and distribution of nanowire geometry in the pump-probe spot.

Futher work with this sample is performed in Chapter.5, and further conclusions are discussed along with future work in Chapter.7.

Chapter 4

Nanoantenna/Cantilevers for GHz Acoustic Response

It has been previously shown for SiN cantilevers of 10 - 100 μm lengths that high Q-factor mechanical resonances can be interrogated in time and frequency domain by laser deflection methods (Babaei Gavan et al. (2009), Sadeghian et al. (2010)). This order of magnitude length cantilever produces resonances from 10 kHz - 100 MHz. The detection scheme also relied on thermal noise to drive the rather than excitation from the laser.

To change the cantilever response to GHz a large change in cantilever size (10 μm - 100 nm) must be made. The change in scale not only affects the cantilever resonance frequency, but also reduces the amplitude. It can be shown by approximating cantilever thermal energy as mechanically stored potential energy, that the displacement of 10-μm cantilevers will be on the scale of of the order 10 pm Babaei Gavan et al. (2009). Meanwhile for 100-nm cantilevers, displacements will be approximately 10^{-4} pm. In Sadeghian et al. (2010), the detection of 150-μm cantilevers was enhanced by deflection at the cantilever tip. In addition, bi-material cantilevers have been characterised for structures producing MHz resonances (Datskos et al. (2004)). For 100-nm length cantilevers, it was not be possible to interact with a specific location of the cantilever. Therefore, the structure must be engineered to exploit a mechanically sensitive reflectivity/transmission effect such as plasmonic resonances.

In this research, a sample was built to make use of plasmonic absorption to enhance acoustic interrogation. The basic design is a gold nanoantenna dimer on top of a SiN substrate that is milled leaving one of the gold strips in each antenna on a cantilever, free to vibrate independently. The structure consists of both: a cantilever with approximately GHz acoustic resonances and a nanoantenna with plasmonic resonances in the near infra-red. The cantilever vibration caused the nanoantenna gap to expand and contract, changing the plasmonic resonance and thereby coupling acoustic response to plasmonic enhancement.

Therefore, this sample combines the well documented behaviour of a nanoscale cantilever with the high sensitivity and large absorption cross section of a nanoplasmonic resonator. In addition, large arrays of these structures can be produced which increases sensitivity, and reduces the complexity of measurement over interaction with a single nanoantenna on this scale.

4.1 Optical Response of Nanoantenna Dimers

The plasmonic response of the nanoantenna is an effect of localised surface plasmon polaritons (LSPP), where this can be considered as a standing wave across the nanostructure surface. As shown in Fig.4.1(a), an incoming E-field induces the vibration of free electrons relative to the nanorod lattice. For a dimer configuration, the LSPPs are coupled as long as the separation of the two structures in the dimer is much lower than the wavelength of the excitation field; the dimer LSPPs may be described as oscillating dipoles, coupled via Coulomb interaction. The charge oscillation on each nanostructure is restored by Coulomb forces proportional to the direction of oscillation. Parallel to the dimer axis Fig.4.1, charge oscillations are started by the incoming E-field $E_{excitation}$, the charges then oscillate across the nanostructure surface with Coulomb forces coupling the motion across the nanoantenna gap. for the perpendicular case the excitation will be lower and blue-shifted due to the changes in scale. The actual charge distributions will differ from those shown in the schematic diagram, and will have multiple orders as they may be described as standing waves. For $E_{excitation}$ polarised in the dimer axis, the

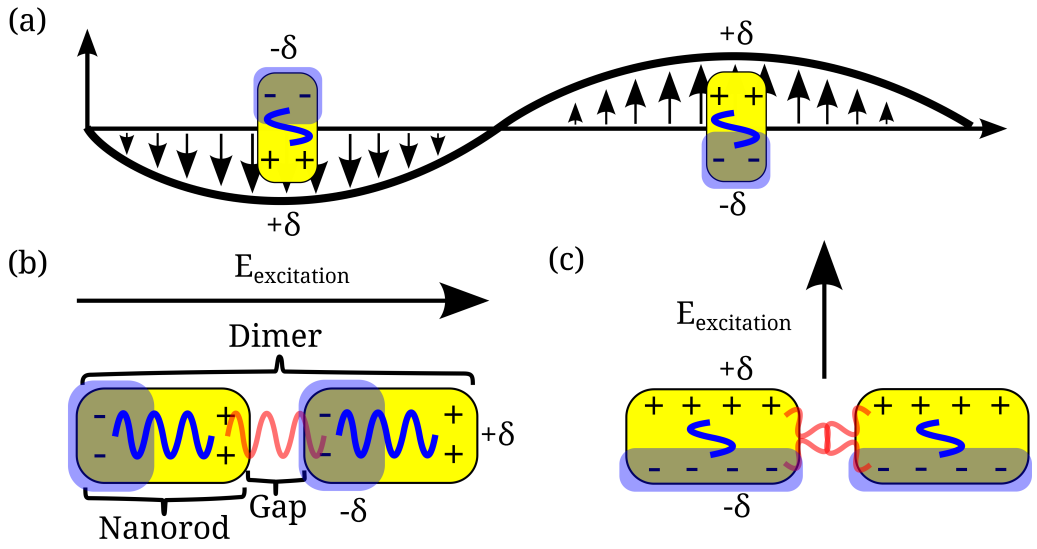

Figure 4.1: Schematic diagram of the LSPP mechanism for nanoantenna dimers. (a) Induced charge differences in the surface of the nanoantenna are generated by the incoming exciation E-field $E_{excitation}$. (c) for an excitation field parallel to the dimer axis (c) perpendicular to the dimer axis. The charge distributions oscillate (blue) and are coupled to the other dimer via Coulomb interaction (red).

LSPP interaction is expected to be much stronger than that in the perpendicular case. This effect is due to the comparatively large field enhancement in the nanoantenna gap.

The key features that change the LSPP characteristics are, material and geometry. Metals and metal oxides nanorods have both been demonstrated as viable platforms for nanoantenna dimers (Weeber et al. (1999), Kottmann and Martin (2001), Imura et al. (2004), Aizpurua et al. (2005), Muhlschlegel (2005), Muskens et al. (2006), Bharadwaj et al. (2009), Abb et al. (2014)). Previous research has shown that changes to substrate and gap materials can fine tune the plasmonic response, or uncover other mechanisms, such as fast electron generation. The geometry of the antenna is instrumental to the response as well since the width and length will affect the $E_{excitation}$ coupling, the gap size will affect the coupling across the dimer, and the two will change the near-field enhancement.

The effects of changes to gap size have been reported in Abb et al. (2014) and Kuykendall et al. (2004) for ITO nanorods in the gap. The results of nanorod transmission spectra for changing geometry showed that changes in gap size will more strongly red-shift the

long-wavelength side of the resonance peak. This feature results in ≈1-2 μm resonance wavelength shifts for length changes of ΔL= 250 nm (in ITO nanorods from 200 nm to 1000 nm). This implies that an estimate of peak wavelength shift for pm displacements of dimer gap size the will be of the order ≈pm.

4.2 FIB Nanoantenna/Cantilever Fabrication

These samples were made by O. Buchnev through Focused Ion Beam (FIB) milling from a 100-nm thick SiN/Au membrane window for x-ray microscopy (from Norcada). The membrane is composed of 50 nm of Au on top of 50 nm SiN.

The design dimensions of the nanoantennas and cantilever have been selected both to produce an appropriate vibrational response and to maximise the plasmonic enhancement at close to 1-μm wavelengths. These design criteria narrowed the dimensions of the antennae and cantilevers to l=100 - 300 nm, w=100 nm and gap=1-3 nm.

The FIB is used to etch away the Au from the SiN, apart from two co-linear strips to produce linear nanoantenna dimers, shown in Fig.4.2(a-d)). The FIB is then used to cut through the SiN in a "u-shape" leaving an Au antenna on a SiN cantilever. This process was performed for 4 different designs of nanoantenna/cantilever length, and each design was repeated in a 25x25 grid separated by 860 nm in each direction, to produce a total area of 21.5x21.5-μm for each structure design. The separation of each dimer to its nearest neighbours was selected to minimise dimer-dimer interactions. Limitations for fabrication included the resolution of Au etch and SiN cut-through due to time constraints on the sample exposure. A more intense beam (used for shorter exposure time) produces a larger cut in the membrane than long exposures at lower intensities.

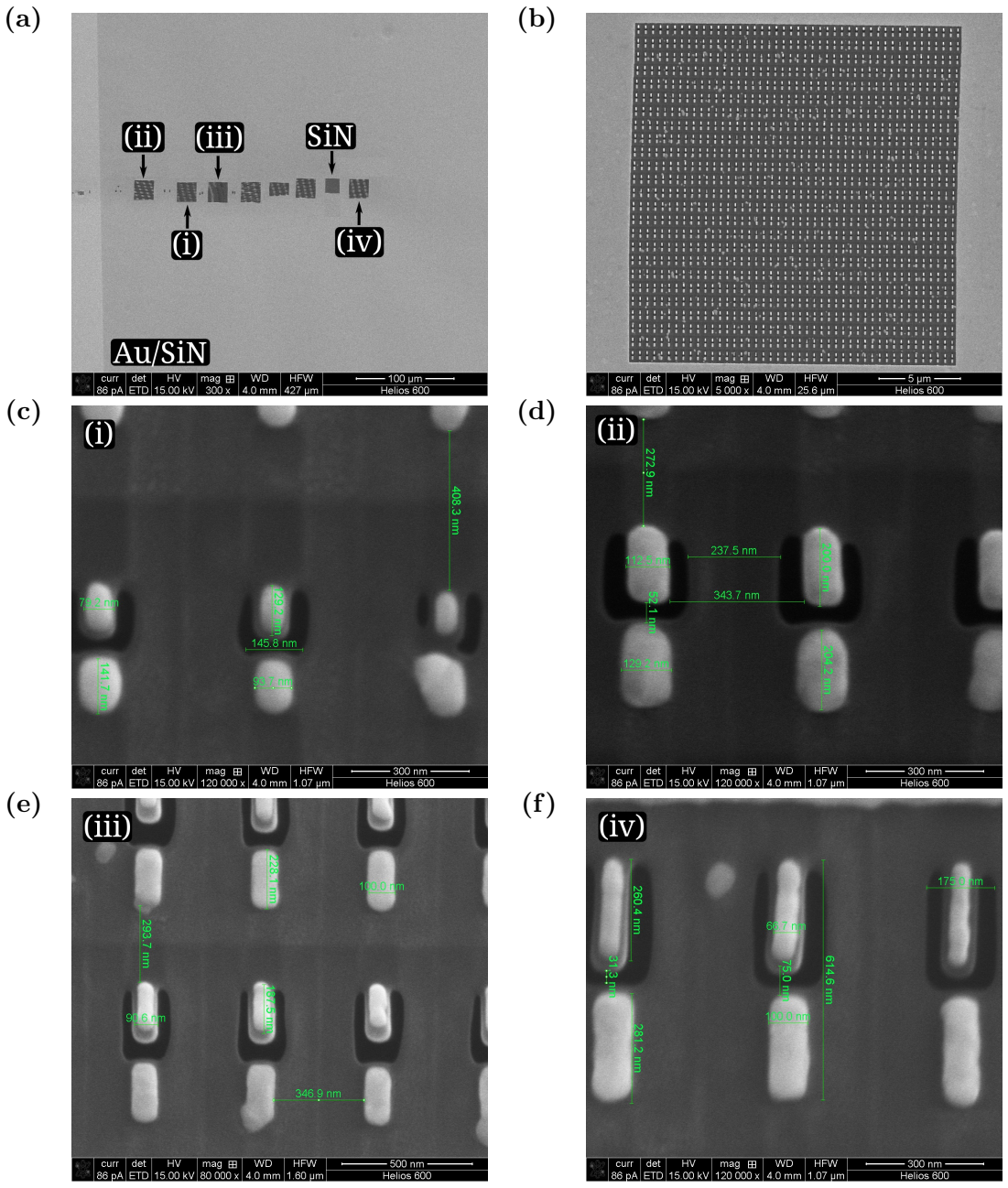

Figure 4.2: SEM of NEMS on SiN/Au nanomembrane. (a) Multiple sites were fabricated with different geometry sizes, from left to right named in ascending geometry size order, "ii", "i", "iii" and "iv". A further three fabrication test sites were made (to the right of "iii"). Finally a section of gold was uncovered leaving blank SiN. (b) A single site ("iv" site) is shown, composed of 25x25 dimers. Each dimer is formed by a Au nanorod pair, displayed as light sections, the top nanorod is surrounded by u-shaped hole in nanomembrane, displayed as dark section. Fig (c-d) display the dimer detail of sites (i-iv), the full list of dimensions of the nanoantenna/cantilever are displayed in Table.4.1.

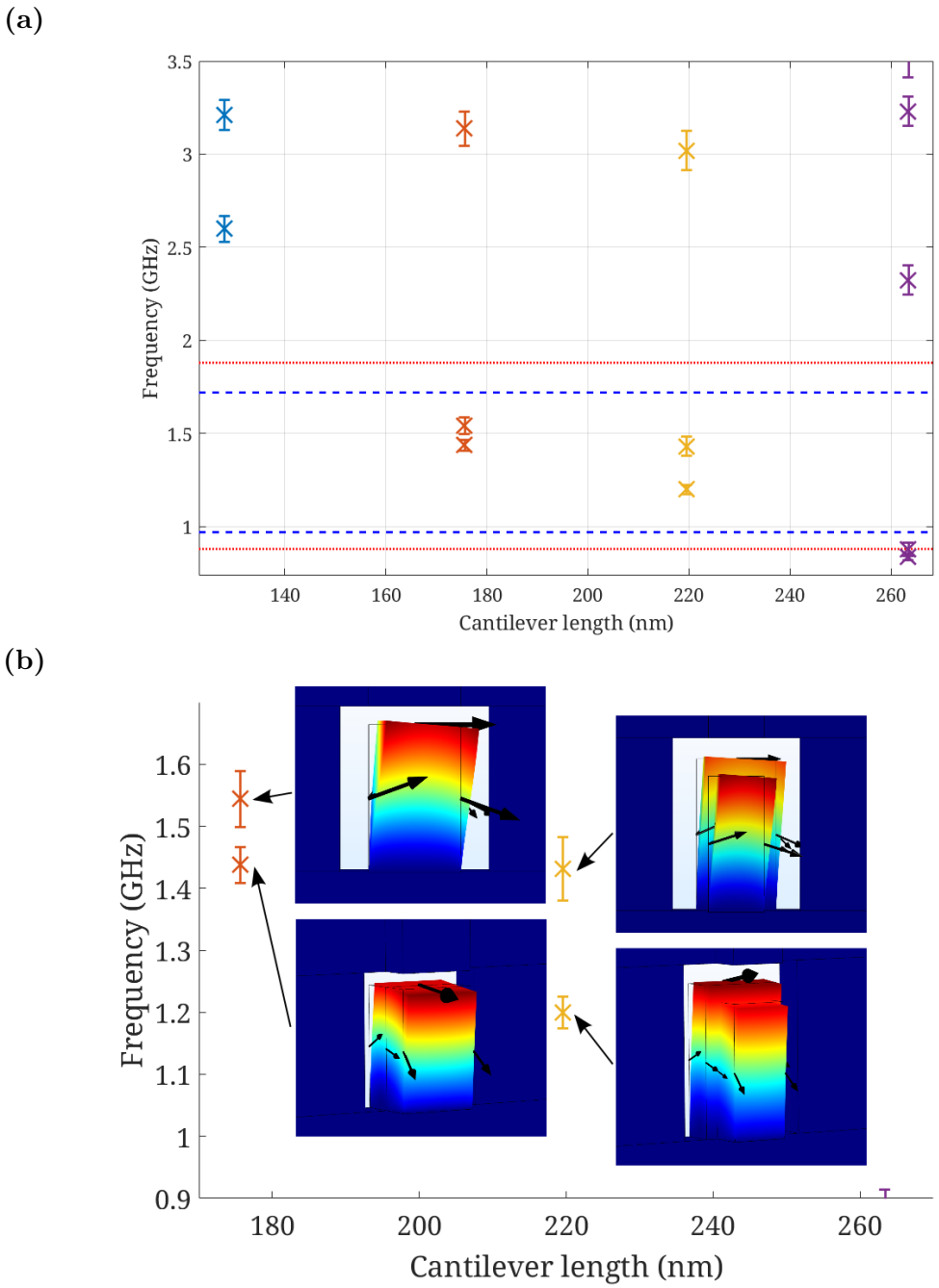

Figure 4.3: (a) Structural eigenfrequencies for SiN/Au cantilevers ("i" blue, "ii" orange, "iii" yellow and "iv" purple) displayed as a function of cantilever SiN length. The Q-factor calculated by FEM is used to calculate the FWHM of the modes, which is displayed as the error bars. The frequency tuning range of the 1-W tZ VECSEL (blue) and 6.6-W tZ VECSEL (red) are overlaid. (b) Shows the eigenfrequencies as a function of cantilever length for the repetition frequency frequency range accessible by the tZ-VECSEL cavity tuning for "ii" orange and "iii" yellow. Inset are the mode shapes for the modes in range, (top) torsional (bottom) transverse bending.

	SiN		Au			$f_e(GHz)$	
Site	L (nm)	W (nm)	L (nm)	W (nm)	Gap (nm)	trans	tors
(i)	128.0	76.8	106.1	36.6	18.3	2.60	3.22
(ii)	175.6	109.8	175.6	109.8	22.0	1.44	1.54
(iii)	219.5	115.9	195.1	80.0	30.5	1.20	1.43
(iv)	263.4	91.5	241.5	58.5	22.0	0.84	0.88

Table 4.1: *SiN/Au cantilever and nanoantenna dimer dimensions taken from SEM images in Fig.4.2. L (length) and w (width) are displayed for both SiN and Au dimensions. The result of FEM analysis are shown, structural eigenfrequencies f_e for transverse bending modes (trans) and torsional modes (tors).*

4.3 Nanoantenna/Cantilever Characterisation and FEM Simulation

Figure.4.2 shows SEM imagery of a arrays of the fabricated cantilevers. Each array is 25x25 nanoantenna dimers, while each SEM focuses on 3. The SEM displays Au nanoantennas as pairs of light areas, SiN as grey and cut-through as a black "U-shape".

The samples fabricated for my research have been shown via FEM modelling (Fig.4.3) to have first-order bending resonances from 800-2000 MHz. Of the four samples two therefore have first-order resonances within the range accessible by the tZ-VECSEL, while the other may display other resonances in this range.

Fig.4.3 shows the results from FEM simulation based on SEM recorded values for cantilever dimensions. The output of the FEM model is used to display eigenfrequencies for the structure in the range of 1 GHz, including an estimate for Q-factor based on material losses for SiN and Au. The primary modes that result for this analysis are divided into: transverse bending and torsional, some the remaining possible modes are twisting, flexural and extensional, these modes are theorised to have lower coupling to the driving force provided by electrostriction due to the direction of excitation and the theoretical magnitude of displacement given by FEM analysis. Fig.4.3(a) shows the modes present for the cantilevers in the sample used for this research as a function of the length of the cantilever, this dimension of the nanostructure is the main factor in the resonance frequency value. The Q-factor is determined by the material losses which have been estimated by making use of research with Au structural mechanics. This value is used

to determine the FWHM of the resonance and displayed as the errorbars in the figure. However, the Q-factor given here is incomplete, a more complete picture is given by the Q-factor derivation for nanoscale cantilevers in Babaei Gavan (2009). Fig.4.3(b) shows a limited range of frequencies corresponding to the tZ-VECSEL Δf_{Rep} tunability range, inset are the mode shapes for the four modes within range, the lower frequency modes are bending modes and the higher frequency modes are torsional.

Q-factor modelling is discussed in Babaei Gavan (2009). The primary mechanisms responsible for damping are: thermo-elastic damping (TED) and collisions with gas molecules (described as molecular or viscous regimes depending on Knudsen number). These considerations may be used to design the frequency domain FD experiment, but cannot be solved in their entirety for the cantilevers without retrieving dynamic parameters specific to the sample materials and geometry.

4.4 Experimental Methods

As described in Sec.3.3 a dual setup for linear spectroscopy and time domain spectroscopy was built to characterise the nanostructures. The same setup was used to characterise the nanoantenna/cantilevers to determine the nanoantenna dimer and measure time-domain response of the cantilever. In addition, the nanoantenna dimers were polarisation sensitive (as discussed in Sec.4.1), as such linear reflectivity was aligned to dimer axis, and for time domain spectroscopy the probe beam was also aligned to the dimer axis.

4.5 Nanoantenna/Dimer Cantilever Results

4.5.1 Linear Reflectivity

The results of transmission and reflection characterisation are displayed in Fig.4.4. Each sample site reflectivity and transmission was measured separately, for polarisation parallel to the dimer axis, Normalisation of reflection and transmission was performed with

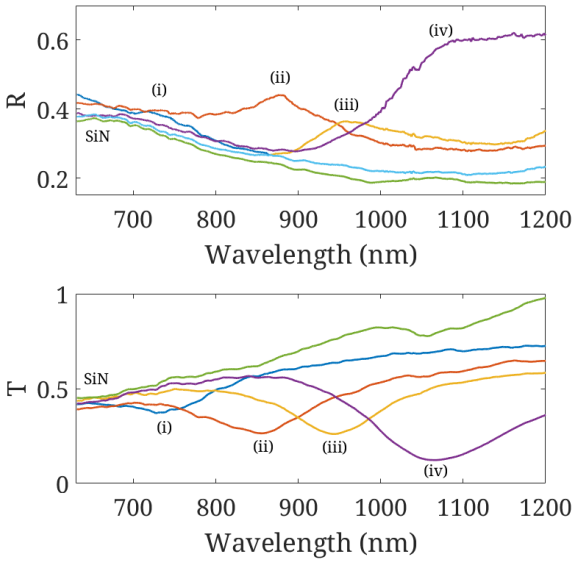

Figure 4.4: *Normalised reflectivity and transmission, in parallel polarisation to the dimer axis, for the four nanoantenna cantilever arrays. The traces correspond to the cantilever dimensions in Table.4.1 referenced here by their gold length, and display resonances at (i, blue) 750 nm, (ii, orange) 850 nm, (iii, yellow) 950 nm, and (iv, purple) 1050 nm. A blank SiN section trace is also displayed (green).*

a gold reflector and free-space respectively. The traces for each site in Fig.4.4 show peaks associated with plasmonic near-field enhancement; (i) 750 nm, (ii) 850 nm, (iii) 950 nm, and (iv) 1050 nm. The absorption/scattering profile for bare SiN is shown in green, but may be influenced by a trace layer of Au that remains from FIB fabrication. The peaks are more strongly visible in transmission data, which was also less affected by membrane misalignment than reflection. As a result the work performed in Chapter.5 was performed in transmission only.

4.5.2 Time-Domain Spectroscopy

The results of time-domain analysis of the SiN/Au cantilevers are shown in Fig. 4.5 4.6. These results are recorded using the same setup shown in Sec.3.3 for GaP nanowires. The reflection and transmission traces shown here were demodulated at the pump modulation frequency ΔR and ΔT and the probe frequency R and T. These were demodulated to obtain the signal from pump interactions with the probe (ΔR and ΔT) and the variations in probe power (R and T). Finally the ratio of each ΔR/R and ΔT/T is shown which

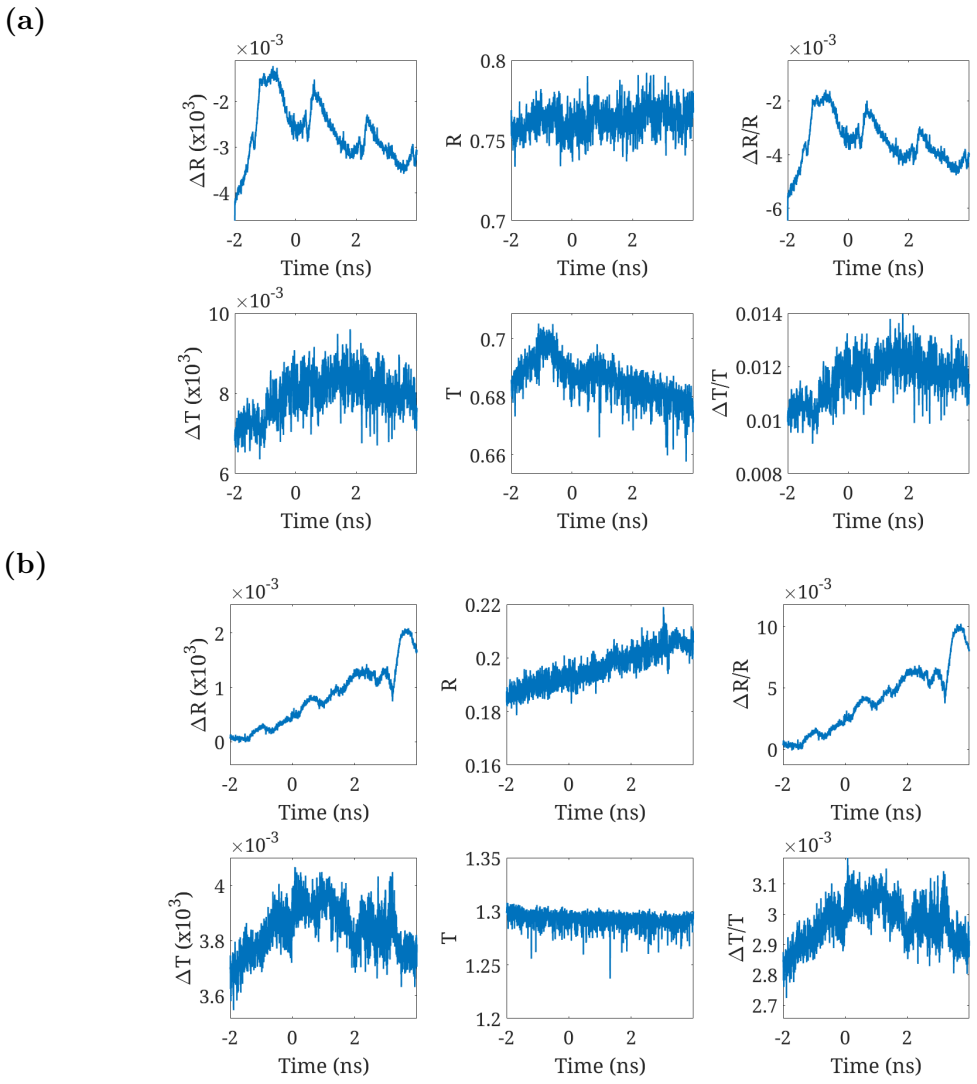

Figure 4.5: *Time domain data displaying typical reflectivity and transmission for SiN cantilevers (a) "i" and (b) "ii", described in Sec.4.3. The traces displayed were demodulated at probe chopping frequency (R and T) and pump frequency (ΔR and ΔT), and the ratio of each ($\Delta R/R$ and $\Delta T/T$). Non-linear excitation is visible at t=0 ns, however, variations in pump and probe power were sufficient to be visible over the expected signal, including persistent modulation attributed to mechanical instability of the delay line.*

retrieves the signal with power variation extracted. For the time domain measurement of GaP nanowires (Fig.3.6) only ΔR and ΔT were displayed, however here all three traces are shown to indicate the origins of noise in the setup. Nanoantenna dimer temporal response depends on carriers produced in the nanorods, but was only faintly visible in transmission at 0 ns due to the signal to noise of the resulting trace (ΔT and ΔT/T for (ii) (iii) and (iv)). In reflection, persistent modulations, invariant of excitation time were

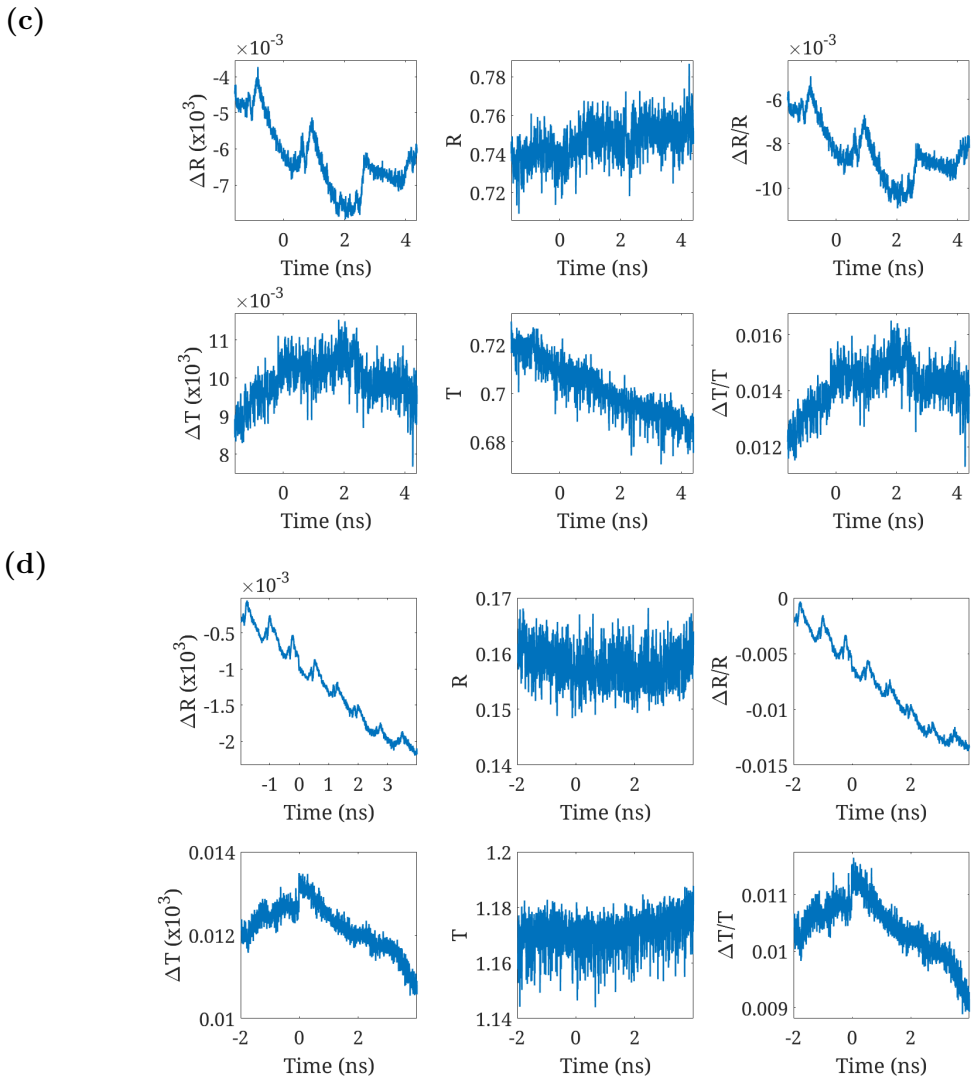

Figure 4.6: *Time domain data displaying typical reflectivity and transmission for SiN cantilevers (c) "iii" and (d) "iv", described in Sec.4.3. The traces displayed were demodulated at probe chopping frequency (R and T) and pump frequency (ΔR and ΔT), and the ratio of each ($\Delta R/R$ and $\Delta T/T$). Non-linear excitation is visible at t=0 ns, however, variations in pump and probe power were sufficient to be visible over the expected signal, including persistent modulation attributed to mechanical instability of the delay line.*

visible. As a result of the low signal to noise, the time domain transient was strongly modulated by mechanical vibration in the delay line and variations in beam overlap, both pointing and size due to imperfect collimation, which are sensitive over the 1.8 m scan range. This cannot be accounted for in the measurement by using R or T since the variation in pump power could not be separated from ΔR or ΔT. For time <0 ns the trace should display a flat profile as the sample should be in a relaxed steady state, this

is not the case and contributes to assessing the remaining trace as a result of delay-line misalignment rather than corresponding to mechanical vibration, or other effects caused by the pump-pulse.

4.6 Conclusions

In this chapter I have described the design, fabrication and characterisation of a novel nanostructure designed with GHz acoustic resonances and LSPP enhanced absorption and scattering. The nanostructure was characterised in reflection and transmission to successfully demonstrate structure-dependent near-field enhancement in the wavelength range 750-1100. This range was selected to be accessible by wavelength tunable CW lasers, for the work detailed in Chapter.5. The structures were also designed using FEM modelling to predict acoustic mode frequencies and engineer GHz modes.

To measure the acoustic response in the time-domain, the same setup used for GaP measurements (Sec.3.3) was applied. The lower response of the nanoantenna compared to highly scattering semiconductor nanowires meant that no signal was resolvable over noise produced by the setup. In addition, the targeted cantilever resonances were dependent on the length, therefore sample inhomogeneity where cut-through the SiN was irregular could shift or eliminate the resonances.

Further work with the nanostructures in this chapter is shown in Chapter.5. Proposed improvements for the detection of acoustic modes in these structures are discussed in Chapter.7

Chapter 5

Frequency Domain Measurement by Resonant Periodic Impact Excitation

Frequency-domain measurement of GHz mechanically active nanostructures has been previously reported for individual nanodisks made from Cu (Tachizaki et al. (2010)), GaAs (Ding et al. (2011)) and Si (Sun et al. (2012)). These detection schemes have been based on low noise GHz detectors and CW external cavity diode lasers. Here we propose a detection scheme based on periodic impact excitation from a pulse train on resonance with the nanostructure. Resonant periodic impacts are expected to drive the structure into a highly excited state, even highly anharmonic regimes.

The nanostructures studied in Chapters 3 and 4 showed minimal or no interaction in the time domain. This was attributed to the signal to noise of the experimental setups, and the increase of 1-2 orders of magnitude in the resonance frequency under study. This reduces the deflection produced by the nanostructure vibration and therefore made time-domain detection a great technical challenge.

5.1 Experimental Methods

To perform the measurement of the proposed excitation mechanism, it was necessary to build a setup for GHz frequency analysis. A pump-probe technique was built using the tZ-VECSEL (described in Sec.2.3.3) to optomechanically excite the sample on resonance, and a continuous wave (CW) probe beam was used to detect the modulation on reflectivity by the mechanical resonance.

The CW probe beam was produced by a wavelength tunable titanium-doped sapphire laser (Ti:Sapphire source). The Ti:Sapphire is configurable for multiple wavelength ranges, with intracavity gratings, for this research the wavelength range 970 -1000

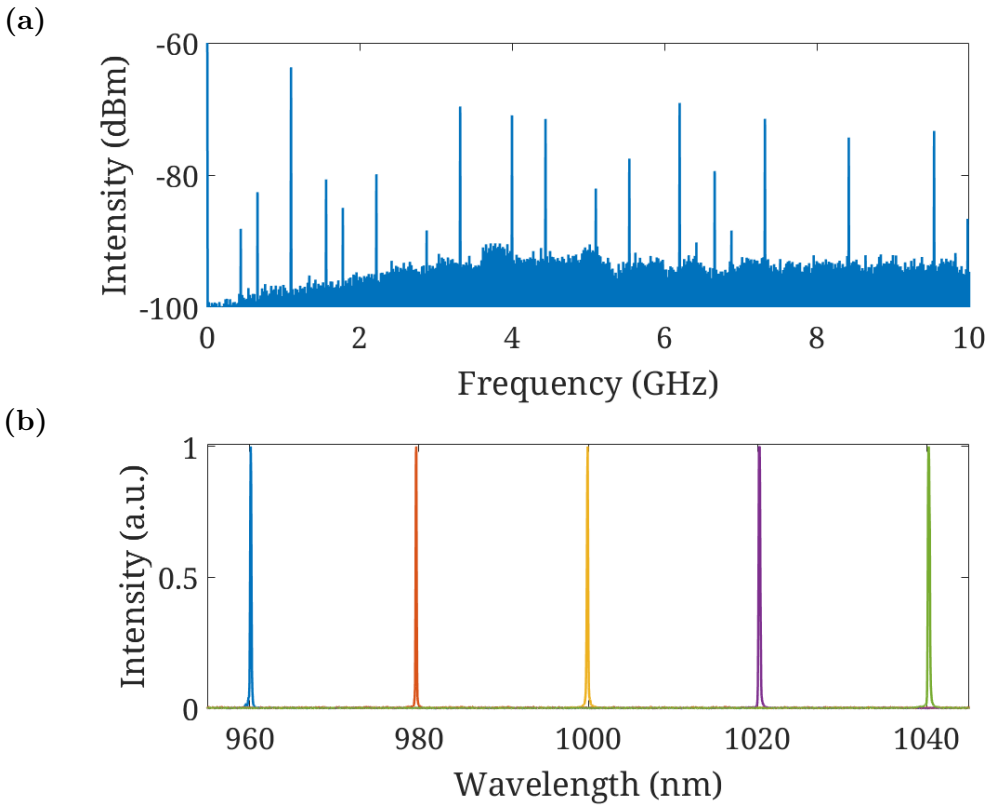

Figure 5.1: (a) A typical RF spectrum of the CW Ti:Sapphire laser, taken at 980 nm. The primary peak in the frequency range of resonances is at 1.1 GHz, secondary peaks are located at 0.44, 0.66, 1.56 and 1.78 GHz. (b) Optical spectra recorded for changes in intracavity grating position. The peak height has been normalised to display the low variation in peak shape due to significant peak intensity changes. Recorded spectra were limited by the OSA range (960 nm) and the Ti:Sapphire tuning range (1040 nm).

Wavelength (nm)	960-1040
Wavelength FWHM (nm)	0.1
Average Power (W)	2.5

Table 5.1: *Output characterisation for the CW Ti:Sapphire laser.*

nm was selected, to cover the range of wavelengths for which plasmonic response was recorded for the SiN cantilevers (shown in Fig.4.4).

This setup is shown in Fig.5.2. The pump beam is provided by a tZ-VECSEL as described in Chapter.2, providing intracavity tuning of the repetition frequency of pulses. The output from a CW Ti:Sapphire laser was used as the probe beam, enabling probe beam optimisation via intracavity wavelength tuning. The tunability of this laser is shown in Fig.5.1(b). The outputs of these two lasers were combined with a 1000-nm dichroic mirror, limiting the Ti:Sapphire to this wavelength, to ensure adequate beam combination. After the beams exit the vacuum chamber a 1000-nm short-pass filter was used to reject the pump beam. In addition a linear polariser was used to increase rejection when the pump and probe beams were orthogonally polarised.

The RF spectrum of the CW laser was recorded (shown in Fig.5.1) to ensure that peaks found in the experiment could be rejected if they match those produced by the laser rather than those corresponding to acoustic modulation. The primary peak present in the RF spectrum near the range of VECSEL tunability appeared at 1.1 GHz, with secondary peaks at 0.44, 0.66, 1.56 and 1.78 GHz.

During the experiment itself, the VECSEL output was incident on a 50:50 beamsplitter (BS), to split an amount of the pulse train away to the three measurement systems required for verificatrion of mode-locking behaviour: RF spectrum analyser (RFSA), optical spectrum analyser (OSA) and autocorrelator (AC). Input to the RFSA was via a fibre-coupled 25-GHz fast photodiode. The AC used free space optics and is further optimised with a linear polariser (LP) and half-wave plate ($\lambda/2$). The results of pulse train characterisation with this arrangement are those shown in Sec.2.3.3.

The outputs from both lasers were combined with a 1000-nm dichroic mirror and independently power and polarisation adjusted with LP, $\lambda/2$ and variable neutral density

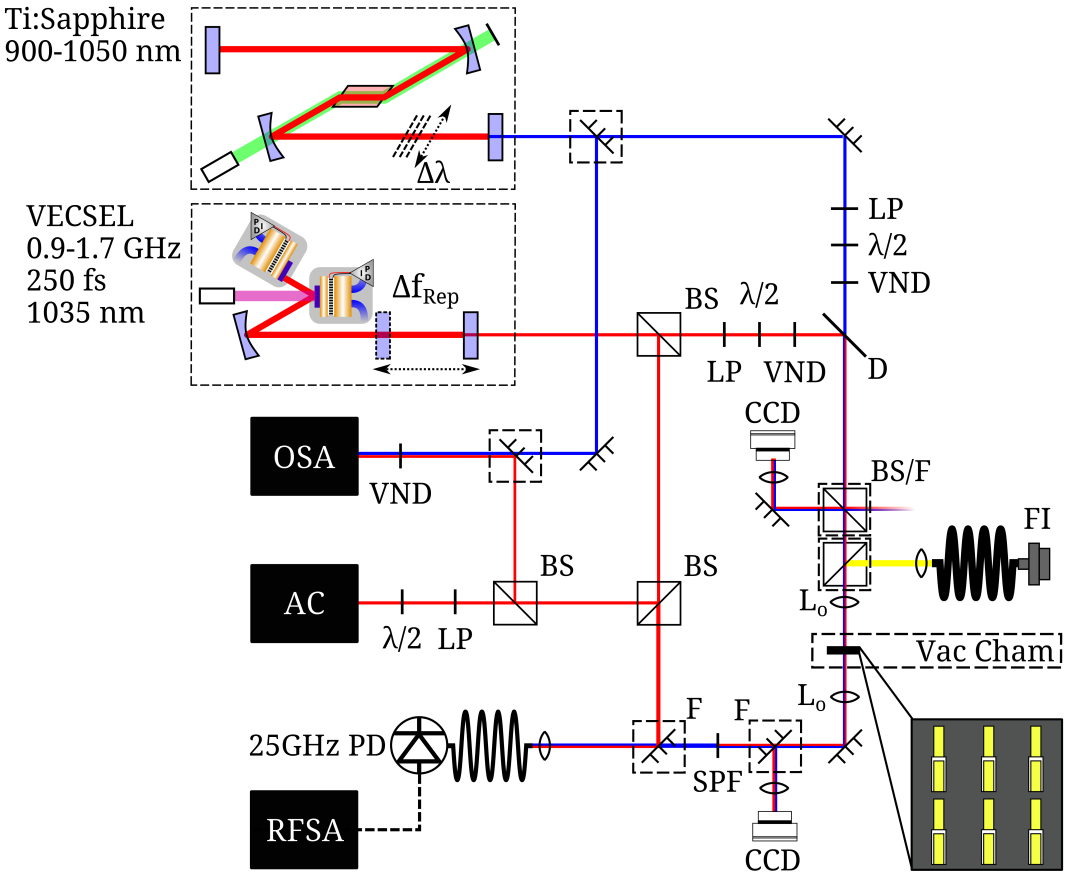

Figure 5.2: *A schematic diagram of the setup used for resonant excitation using a pump beam (red) from a continuous intracavity repetition frequency tuning (Δf_{Rep}) with a VECSEL. The sample transmission is then interrogated with a probe beam (blue) from a CW Ti:Sapphire which is wavelength tuned ($\Delta\lambda$) with an intracavity birefringent filter. The pump and probe beams were independently power and polarisation controlled by $\lambda/2$, LP and VND, and then combined using a 1000 nm dichroic mirror.*

filters (VND). The beams were further combined with a white light fibre illuminator (FI) for sample imaging. Two microscope objectives (the same ones used for TDS Sec.3.3.2) were used to focus onto the sample and collect as much of the transmitted light as possible. The sample was contained within a vacuum chamber (described in Sec.3.3.1) to isolate the sample under test from the air.

Two schemes were used for testing the response of polarisation sensitive nanostructures to make best use of the plasmonic near-field interaction, pump rejection and multiple acousto-optic excitation mechanisms. First, polarisation of the probe beam was set to 0° to the dimer axes to maximise the interaction of the probe-beam with the nanoantenna

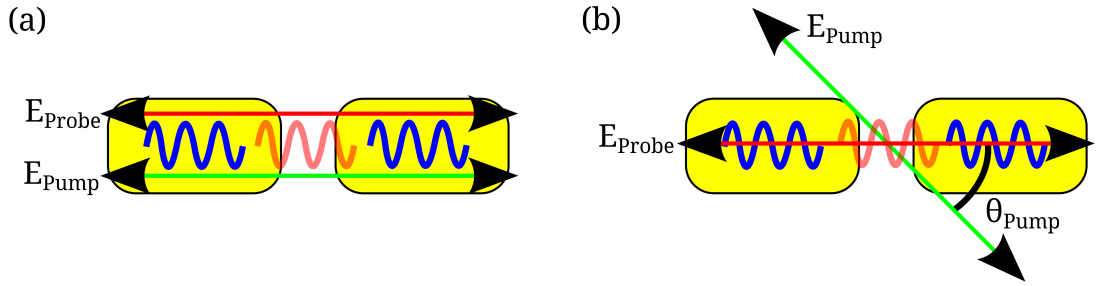

Figure 5.3: Schematic diagram of the two pumping schemes applied to frequency domain measurement to (a) enhance pump-beam interaction with the nanoantenna and (b) improve rejection of pump beam by using linear polarisers.

LSPP. The pump beam polarisation was set to $\theta_{pump} = 0°$ similarly to the probe beam to maximise the excitation via pumping the LSPP. The pump polarisation was also tested at $\theta_{pump} = 45°$ to account for mechanisms such as electrostriction that excite vibrations perpendicular to polarisation, this polarisation was also used to reject half of the pump beam by using a linear polariser oriented to the dimer axis.

5.2 Results

5.2.1 Semiconductor Nanowires

The results of frequency domain testing are displayed in Fig.5.4. RF spectra recorded with a 25-GHz photodiode are shown as a function of 100-MHz repetition frequency steps. The results are displayed with a red line corresponding to the expected location of resonantly excited peaks, and black lines retrieved from the Ti:Sapphire RF displayed in Fig.5.1(a). RF spectra were recorded up to 4 GHz to record potential peaks from higher frequency modes that may result from improved coupling as a result of vibrational shapes, no peaks in this range were observed so Fig.5.4 displays the range for resonant excitation.

Even at high pump powers there are no visible modulations corresponding to acoustic modes predicted with FEM, at 1.4 GHz or subharmonic at 2.2 GHz. The peaks corresponding to the RF peaks recorded for the Ti:Sapphire are visible at -90 - -85 dBm, over a noise floor of -100 dBm. This can be attributed to low coupling of the VECSEL

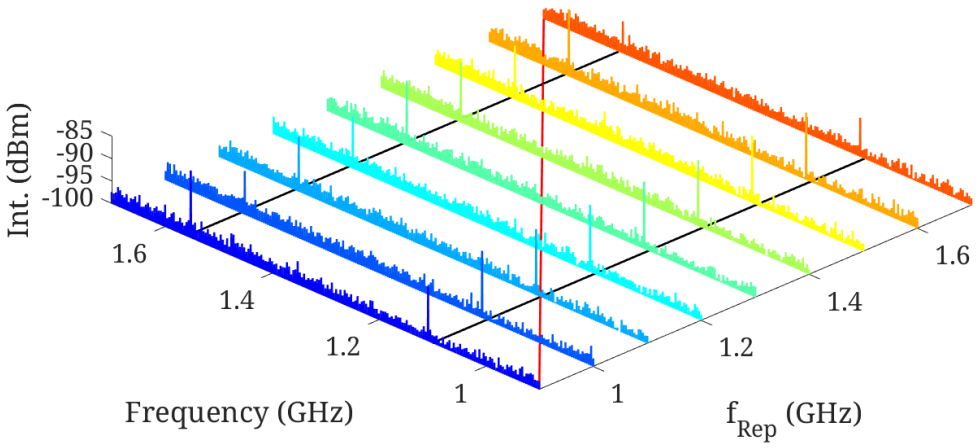

Figure 5.4: *RF spectra of the Ti:Sapphire probe beam transmitted through the GaP nanowire sample (described in Chapter.3), recorded as a function of VECSEL repetition frequency (blue to red). Black lines correspond to RF peaks recorded in Ti:Sapphire laser output. The red line represents resonant excitation where frequency is equal to the driving repetition frequency.*

pulse train to acoustic excitation, and low modulation intensity provided by nanowire acoustic modes.

5.2.2 Nanoantenna/cantilevers

The results of frequency domain testing with the nanoantenna/cantilevers are displayed in Fig. 5.5, 5.6, 5.7 and 5.8. Peaks at 1.1 GHz are visible mainly for site "i" spectra, corresponding to the CW Ti:Sapphire laser mode at this frequency. The peaks are shown strongly on the spectra (10 dB above the noise floor) for the site "i" nanoantenna/cantilevers, this was performed at higher power than the remaining data sets, but was used for "i" as initial testing showed no signs of damage.

Laser damage threshold of the sample was approximately 0.5 mW for the ML-VECSEL and 20 mW for the CW-Ti:Sapphire. Above the damage threshold, the sample displayed higher transmission and lower reflectivity under optical microscope. SEM imaging of the sample after experimentation showed darkening of the sample surface, which was attributed to stripping the residual gold layer away from the SiN (SEM shown in Appendix.D).

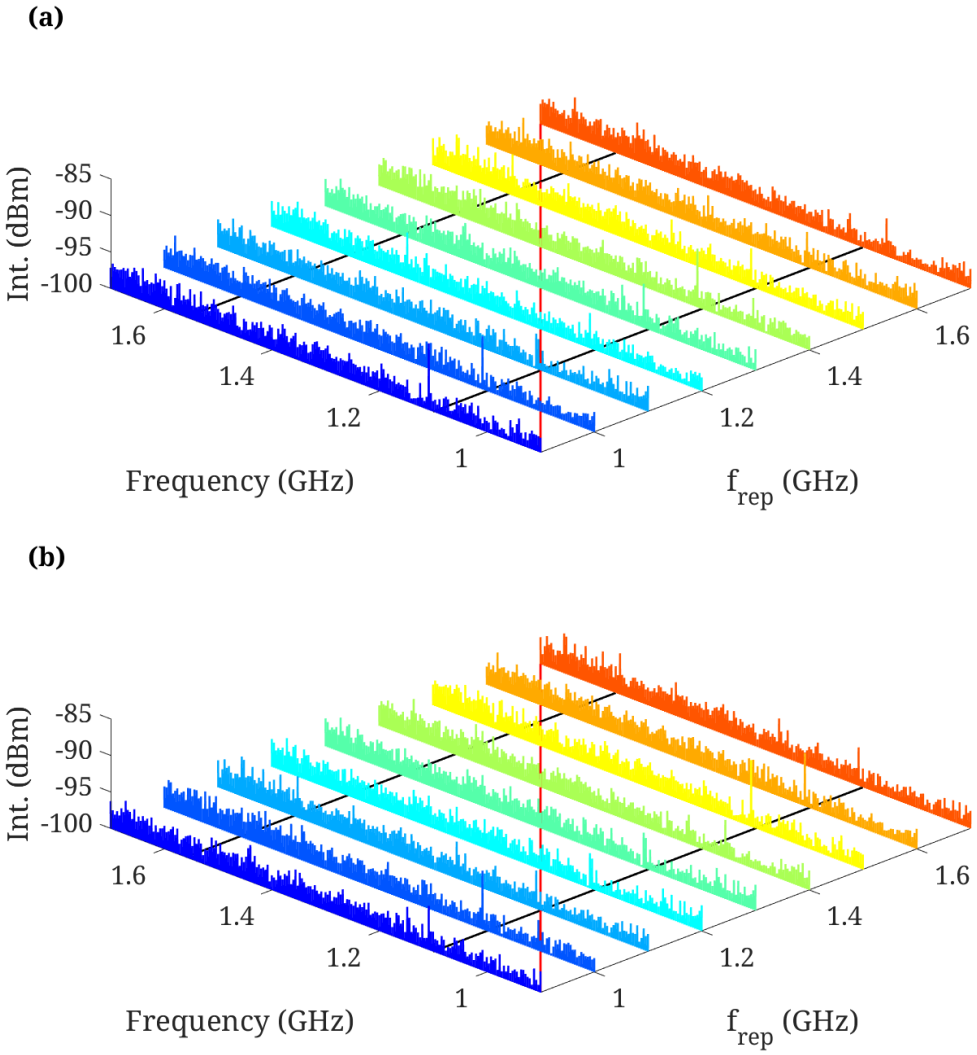

Figure 5.5: *RF spectra of the Ti:Sapphire probe beam transmitted through the SiN/Au cantilever sample "i" (Described in Chapter.4), recorded as a function of VECSEL repetition frequency (blue to red) for (a) θ_{pump}= 0°, and (b) θ_{pump}= 45°. Black lines correspond to RF peaks recorded in Ti:Sapphire laser output. The red line represents resonant excitation where frequency is equal to the driving repetition frequency.*

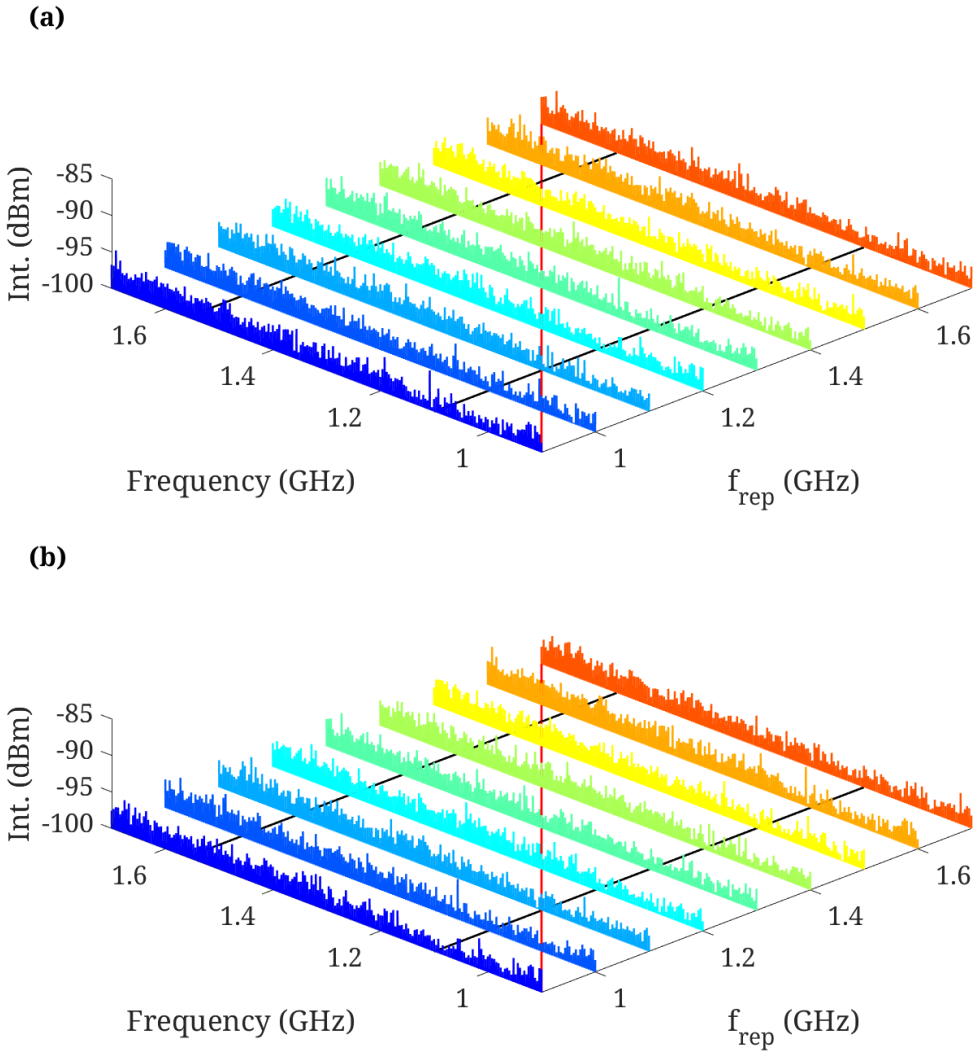

Figure 5.6: *RF spectra of the Ti:Sapphire probe beam transmitted through the SiN/Au cantilever sample "ii" (Described in Chapter.4), recorded as a function of VECSEL repetition frequency (blue to red) for (a) θ_{pump}= 0°, and (b) θ_{pump}= 45°. Black lines correspond to RF peaks recorded in Ti:Sapphire laser output. The red line represents resonant excitation where frequency is equal to the driving repetition frequency.*

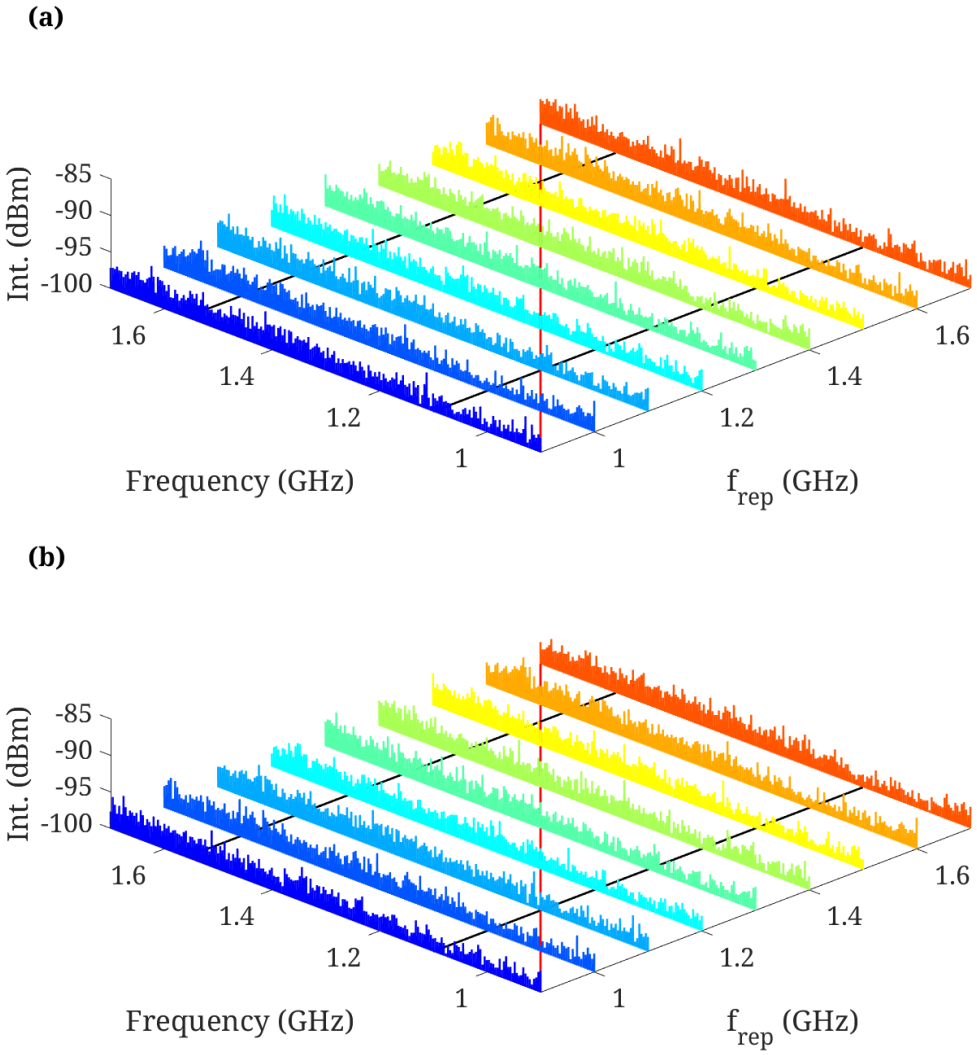

Figure 5.7: *RF spectra of the Ti:Sapphire probe beam transmitted through the SiN/Au cantilever sample "iii" (Described in Chapter.4), recorded as a function of VECSEL repetition frequency (blue to red) for (a) θ_{pump}= 0°, and (b) θ_{pump}= 45°. Black lines correspond to RF peaks recorded in Ti:Sapphire laser output. The red line represents resonant excitation where frequency is equal to the driving repetition frequency.*

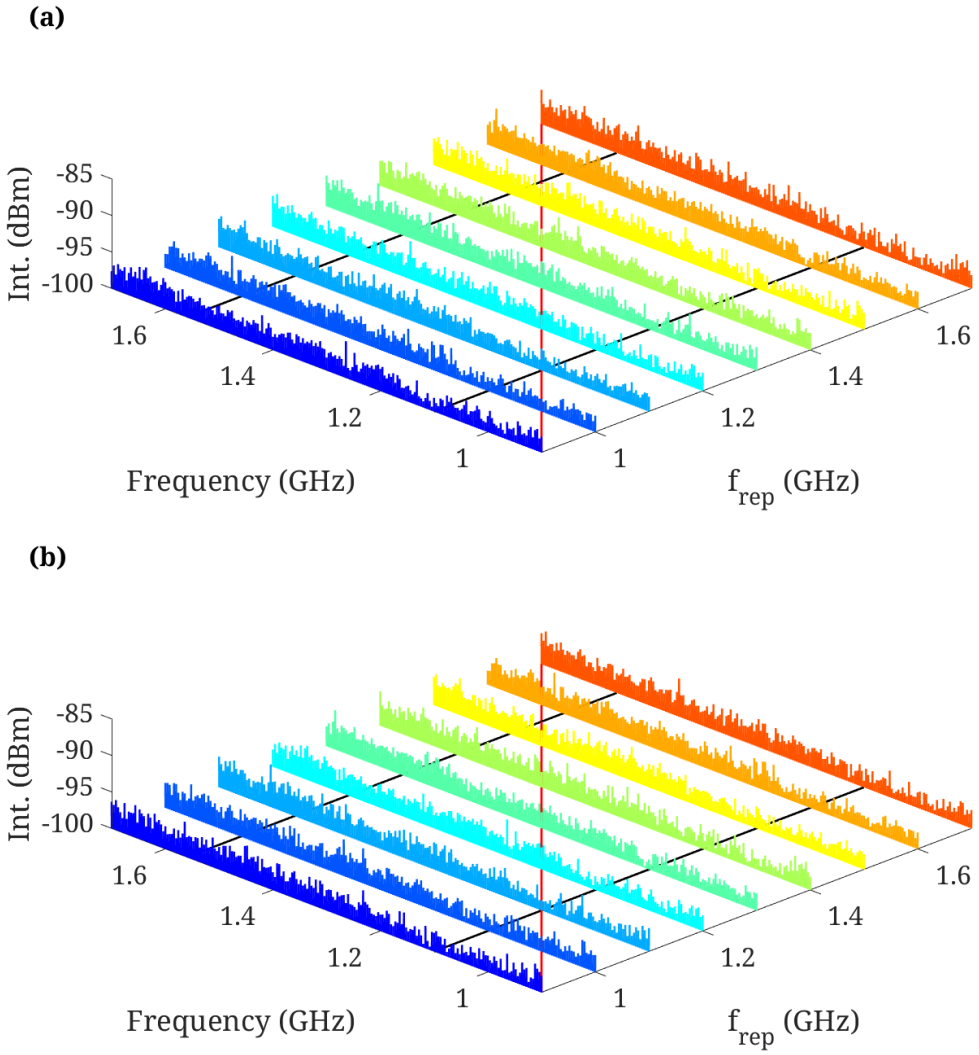

Figure 5.8: *RF spectra of the Ti:Sapphire probe beam transmitted through the SiN/Au cantilever sample "iv" (Described in Chapter.4), recorded as a function of VECSEL repetition frequency (blue to red) for (a) θ_{pump}= 0°, and (b) θ_{pump}= 45°. Black lines correspond to RF peaks recorded in Ti:Sapphire laser output. The red line represents resonant excitation where frequency is equal to the driving repetition frequency.*

5.3 Conclusions

This chapter has described the first iteration of a novel frequency domain measurement based on direct resonant periodic impact excitation from a tunable repetition frequency laser. The structures and scanning range for this experiment have been determined by the output of the laser described in Sec.2.3.3.

The results displayed in this chapter were not able to resolve acoustic excitation over the noise of the setup. This is limited by resonance Q-factors, laser noise, and coupling mechanisms, both for detection and driving. The acoustic modulation was expected to modulate the CW probe beam by scattering and reflection changes over the eigenmode vibration. For the SiN cantilevers the structures were designed so effects harnessed for CW detection were further enhanced by LSPP.

Proposed improvements and further conclusions for the experiment are discussed in Chapter.7.

Chapter 6

Intracavity PCA-SESAM for VECSEL THz Emission

In this chapter, the design and fabrication of a semiconductor structure with dual functionality as a SESAM for VECSEL mode-locking converted to an intracavity THz emitter is described.

Improvements to VECSEL outputs (power and pulse duration) allow the ML-VECSEL to compete with the pulse trains of conventional systems, but with the additional benefit of cavity flexibility and intracavity elements. To harness these characteristics we have fabricated a gold mask directly onto the surface of a conventional SESAM to produce a Photo-Conductive Antenna SESAM (PCA-SESAM). Using the PCA-SESAM, the VECSEL was mode-locked with the SESAM between the gold strips of the PCA. A pulse train characterisation under THz emission conditions is demonstrated in this chapter. Finally shown with Time-Domain Spectroscopy (TDS), under the conditions for VECSEL mode-locking, is a characterisation of the THz emission with the same PCA-SESAM.

6.1 Experimental Methods

This proposed cavity configuration is dubbed THz-VECSEL cavity and is shown in Fig. 6.1 (a), a VECSEL V-cavity with a standard curved and transmissive output coupler mirror, and a PCA-SESAM is attached to a copper mount with an aperture for heat extraction and to allow THz pulse output. The THz VECSEL can therefore use the large intracavity power to produce THz in place of a high intensity pump beam, and using the optical pulse as the probe beam in a much more compact configuration than typical THz-TDS. In Fig.6.1(b) the stripline antenna with the intracavity mode and the resulting THz output is shown.

6.1.1 PCA-SESAM Fabrication

Fig.6.1(b) shows the gold stripline antenna design on the structure. The SESAM structure used as the semiconductor base for this stripline antenna was a 1035-nm GaAs surface-recombination SESAM identical to that used in Sec.2.1.2, structure (shown in detail in Fig.2.3(b)). To produce the stripline antenna, the 1035-nm SESAM was masked with a strip of tape of ≈1 mm width. The structure was then placed in an evaporator, and Cr and Au were exposed to thicknesses of ≈3±1 nm and ≈100±1 nm respectively. Finally, the mask was removed to expose the SESAM surface with two strips of gold either side, as required for a PCA-gap. The 1-mm PCA gap was selected to minimise the overlap of the antenna with the intracavity mode, which would introduce loss that may affect mode-locking or beam quality. In addition, the large PCA -gap allows a large region of the SESAM to be scanned to find the optimum spot for stable mode-locking and shortest pulses.

6.1.2 VECSEL Cavity Design and Mode-Locking

The VECSEL was constructed as a V-cavity since the gain-structure and SESAM selected were capable of mode-locking at the area-ratio achievable in this cavity. The V-cavity also reduces the laser mode astigmatism and the cavity losses from additional cavity elements.

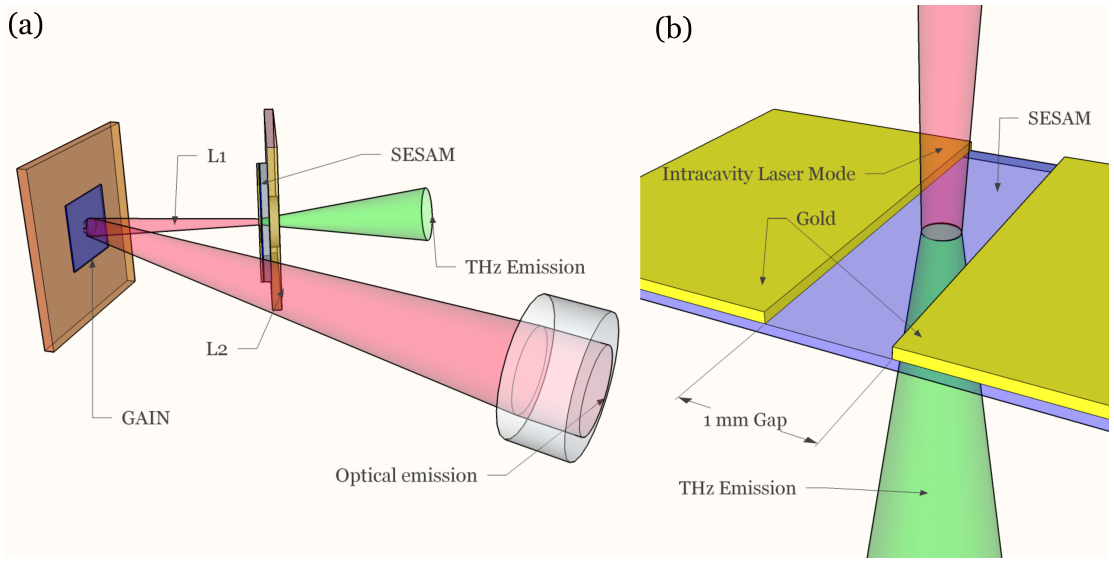

Figure 6.1: *(a) A schematic diagram of the V-cavity layout for simultaneous optical and THz pulses, THz output exits the cavity through the SESAM and optical output exits via the OC. The gain-structure, the PCA-SESAM and the OC were separated by $L_1 = 24$ mm and $L_2 = 67$ mm, with a cavity half angle of $\theta_{cav} = 32°$ (b) A schematic diagram of the coplanar strip-line emitter structure of patterned Gold on a (thickness 0.7 mm) SESAM structure. The PCA gap is 1 mm and the gold strips are 100-nm thick.*

The cavity losses due to the addition of an intracavity element were a priority during the design phase. To mitigate the losses H29 was selected as the gain-structure. H29 was the same design as that used in Sec.2.3, a 5-DQW 1035 nm GaAs-substrate flip-chip structure (structure design in Fig.2.3(a)). This structure was selected for the large number of QWs which provide high gain, while the diamond heat spreader allowed for large power handling. Shorter pulses may have been achieved with a 4-DQW structure, but the reduction in gain was expected to be more detrimental to THz generation, than the potential benefits of shorter intracavity pulses. The same design of 1035-nm SESAM, V623, used for tZ-cavities in Sec.2.3 was paired with the gain structure (structure design in Fig.2.3(b)). The same configuration of structure cooling was applied by means of water-cooled Peltier devices. The size of the Peltiers was increased allowing up to 50 W to be extracted at each structure.

To produce the PCA-SESAM the structure was modified according to the changes described in Sec.6.1.1. And to demonstrate that the THz-VECSEL was capable of direct THz emission, a bias voltage of up to 120-V was applied to the PCA.

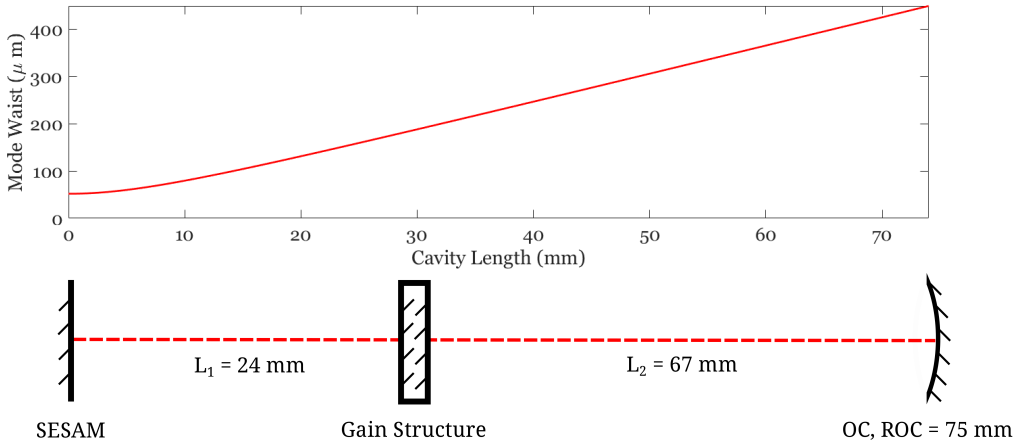

Figure 6.2: *The intracavity mode calculated for a Z-cavity VECSEL built with a 100-mm RoC OC, at separations of: $L_1 = 24$ mm and $L_2 = 67$ mm (as shown in the accompanying folded out cavity diagram) at a cavity half-angle of $\theta_{cav} = 32°$. The mode sizes at the gain and SESAM were: $w_{gain} = 127$ μm and $w_{sesam} = 97$ μm, for an area ratio of approximately 1.7.*

The VECSEL was built as a V-cavity (as shown in Fig.2.8). The VECSEL cavity is formed by a 100-mm RoC 2% transmission OC, the 1035-nm gain-structure and the 1035-nm PCA-SESAM. The VECSEL is optically pumped with up to 35 W by an 808-nm fibre-coupled laser-diode, focused to a 388-μm radius spot (at $1/e^2$). The cavity elements are separated by lengths $L_1 = 24mm$ and $L_2 = 67mm$ (shown in Fig.6.1(a)). The cavity mode calculation for these cavity lengths showed that the mode waists were: $w_{gain} = 127$ μm and $w_{sesam} = 97$ μm, resulting in an area-ratio of approximately 1.7.

The voltage was applied to the SESAM via silver solder to a PCB, which was mounted onto the SESAM surface. The PCB physically limited the cavity half angle to $\theta_{cav} = 32°$ to avoid damage to the PCB from the reflected pump light.

6.1.2.1 Mode-locking

To demonstrate that the PCA-SESAM was viable for intracavity THz generation, first the structure's ability to mode-lock the VECSEL was determined. Therefore, the THz-VECSEL was built and characterised under the conditions necessary for direct THz emission.

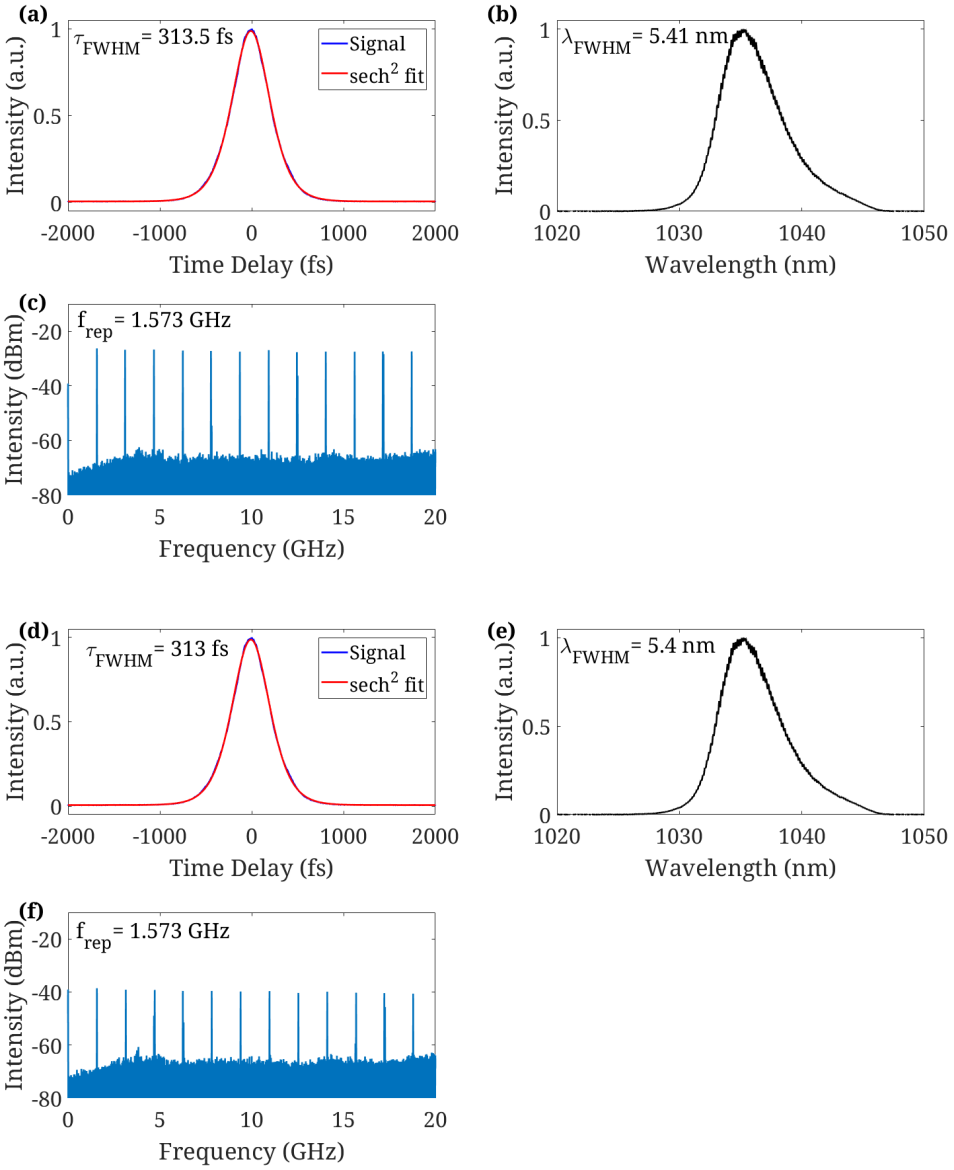

Figure 6.3: *Pulse train characterisation of the 1035-nm THz-VECSEL, pumped at 28 W (a,b,c) and under THz emission conditions (100-V V_{bias}, reduced SESAM cooling) (d,e,f). (a,d) Intensity Autocorrelation (blue) with $sech^2$ fit to extract the time FWHM of 314 fs. (b,e) Optical spectrum displaying a broad peak of $\lambda = 5.4$ nm, the spectrum shows a shoulder toward higher wavelengths attributed to high-order phase structure present in the pulse. (c,f) RF spectrum recorded form 0-20 GHz, with first order peak at $f_{rep} = 1.573$ GHz, and stable peak intensities up to 20 GHz.*

Pump Power (W)	28
Pulse length (fs)	315
Wavelength (nm)	1035
Wavelength FWHM (nm)	5.4
Rep. Rate (GHz)	1.573
Transform limit	1.51 ($\beta = 0.476$)
Average Power (mW)	440
Pulse Energy (pJ)	279.7
Peak Power (W)	890

Table 6.1: *Pulse train characterisation for 1035-nm V-cavity THz-VECSEL, both at V_{bias} of 0 V and 120 V.*

At 28 W of optical pump power, the VECSEL produced an average output power of P_{avg} = 440 mW. The intensity autocorrelation was recorded and a $sech^2$ fit retrieved a FWHM pulse duration of τ_{FWHM} = 314 fs (Fig.6.3(a)). The optical spectrum displayed a broad emission of λ_{FWHM} 5.4 nm at a centre wavelength of λ = 1035 nm (Fig.6.3(b)). The shape of the optical spectrum resembled those, described by Head R. et al.Head et al. (2016) using the same SESAM but a different gain structure with 4-DQW, rather than 5 DQWs used here. The FROG characterisation of this 4-DQW structure showed third-order spectral phase and negative chirp, caused by the 1035 nm SESAM (the same as the pulses from the tZ-cavity based on the same structures). The pulse repetition frequency was measured via the RF spectrum (Fig.6.3(c)) to be f_{rep}=1.573 GHz, with stable harmonics of near equal intensity up to more than 20 GHz (approaching the photodiode response limit at 25 GHz). The time bandwidth product of the pulse train was calculated to be β=0.476 (or 1.51 times the transform limit).

This pulse characterisation was performed with a 1.5-mm hole milled into the SESAM heat sink and a DC bias of up to 120 V (20 V more than that used to produce THz in Sec.6.1.3.1) applied to the SESAM, both these changes showed no visible change in the pulse train stability, pulse duration or wavelength. The change in voltage produces a transient current as required for THz emission. However, the resultant changes to carrier dynamics in the THz-VECSEL were expected to change the mode-locking. The result we obtained was that, even at a bias voltage of 120 V, there was no change whatsoever to the pulse train produced by the THz-VECSEL (Shown in Fig.6.3).

In addition, the THz-VECSEL was shown to lase with the SESAM mode in close proximity to the gold strips. Contrary to the initial hypothesis, this result means that the PCA could be redesigned for a much smaller gap, which would eliminate the need for a 100-V bias. However, the condition required for THz detection via lock-in amplification is a modulation of the THz generation. This can be done with an AC bias voltage, optical chopping of the pump-beam or optical chopping of the THz output. However, kHz AC bias at 100 V was not possible for the high bias voltage required for the 1-mm PCA gap. Neither was it possible to optically chop the pump beam as that would have been the intracavity mode. Therefore the remaining option was to optically modulate the THz output from the PCA-SESAM, requiring a large-gate optical chopper. The modulation frequency was therefore limited by the beam size of the THz to 100 Hz and furthermore the vibration form the chopper destabilised the VECSEL from mode-locking. This limitation made direct THz-TDS impossible with the systems and structures available. A setup was built to test intracavity THz emission, but the optical chopper vibration destabilised the VECSEL so it would not mode-lock.

The intracavity power and spot size on the SESAM was calculated to be result in a fluence of approximately: 0.089 mJ/cm^2. The intracavity fluence was approximately 5.5 times smaller than that in the pulse train from the selected fs-Yb source (0.498 mJ/cm^2 conditions shown in Sec.6.1.3). This mode size and fluence, coupled with the reduced gap size demonstrated that the large 1-mm PCA gap could be reduced without adversely affecting mode-locking or THz generation.

6.1.3 Terahertz Time-Domain Spectroscopy

To characterise the PCA-SESAM as a THz emitter, a pump-probe technique known as THz-TDS was used. As shown in Fig.6.4, seed pulses from a fs laser were split into a pump-beam which was focussed onto the PCA-SESAM, and a probe-beam,used for detection at a resolution of the pulse duration. Both pulses are combined on a second THz antenna for detection, using a variable delay section on either of the two beams to impose time dependence, so that the fs optical-pulse can be use to gate the ps THz-pulse. The experiment was designed to use a laser source with similar pulses to a VECSEL,

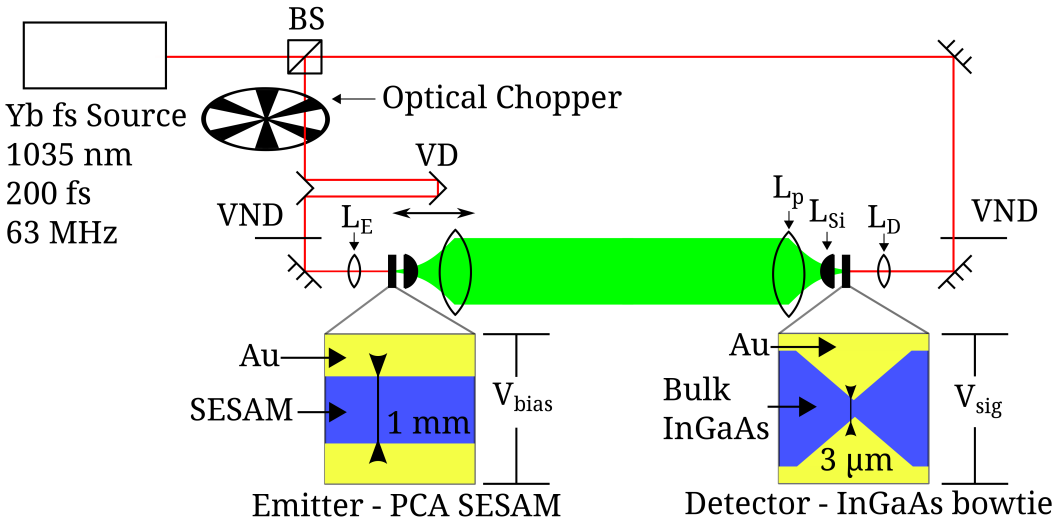

Figure 6.4: *Schematic diagrams of THz time-domain spectroscopy setups based around (a) an extracavity THz emitter pumped with a fs-Yb source. The relative delay of the Yb-TDS is controlled so that the seed pulse and THz pulse emitted by the PCA-SESAM arrived simultaneously at the InGaAs bow-tie detector.*

in both wavelength and pulse duration. Fig.6.4 shows the first characterisation setup, based on an Yb fibre laser that emitted a pulse train with 200-fs $sech^2$ pulses with a centre wavelength of 1035 nm with a FWHM of 8.6 nm, at a repetition frequency of 63 MHz (Table.6.2). First this pulse train was split with a 98:2 non-polarising beam-splitter (BS). The lower intensity beam (probe-beam) was sent through a variable neutral density filter (VND) for power control to limit the probe beam to a maximum of 20 mW. A 10-mm lens (L_D) onto a bow-tie InGaAs detector with a 3 μm tip gap (as shown in the InGaAs bow-tie diagram, Fig.6.4). This type of antenna geometry is more efficient for THz emission/detection, but requires the beam to overlap the bow-tie tips, which made it unviable for the PCA-SESAM. The higher intensity beam (pump-beam) passes

Pulse length (fs)	211
Wavelength (nm)	1035
Wavelength FWHM (nm)	8.59
Rep. Rate (MHz)	63.3
Transform limit	1.6 (β=0.506)
Average Power (mW)	210
Pulse Energy (nJ)	3.3
Peak Power (kW)	15.8

Table 6.2: *Beam characteristics for the High-Q Yb fibre laser.*

though an 800-Hz optical-chopper, a 10-cm variable delay stage (VD), a VND and a 10 mm focusing lens (L_E). The focusing lens was selected to focus the beam onto the PCA-SESAM with a waist comparable to the intracavity mode.

The variable delay stage was added to the pump-beam rather than the probe-beam since the 1-mm gap of the emitter was less critically aligned than the 3-μm gap of the detector. Once the pump-beam was incident on the emitter (PCA-SESAM), a biasing voltage of 100 V was applied to produce a transient photocarrier current, causing the emission of a THz pulse. The THz pulse was collected and collimated by a combination of a silicon hemispherical lens (L_{Si}) and a 50-mm plastic lens (L_p), and then collected and focused by an identical set of lenses onto the detector (InGaAs bow-tie). Detection of the THz pulse is performed by generating carriers in the InGaAs bow-tie detector which are accelerated by the THz E_{field}. Lock-in amplification of the voltage (V_{sig}) produced in the detector would ideally have used a kHz-modulated bias voltage on the emitter. For the PCA-SESAM this was not possible as the bias voltage was 100 V, which made acquiring a modulated source for this voltage difficult. Instead of directly modulating the bias voltage, the pump-beam was modulated at 800 Hz using an optical chopper.

Carriers in the SESAM structure were primarily generated in the SESAM-QW. This means that the carrier population, and therefore the THz emission, will limited for a given SESAM mode area and R%, in the regime of SESAM saturation by resonant excitation. However, as described in Sec.1.3 non-resonant carrier generation may occur in GaAs. This effect has been reported for THz generation by a VECSEL in Mihoubi et al. (2008).

6.1.3.1 Terahertz Time-Domain Results

Fig.6.5 displays the results THz-TDS performed with the PCA-SESAM when pumped with the fs-Yb source in the setup shown in Fig.6.4. The antenna was irradiated with 60 mW average power of 200-fs pulses, at 1035 nm with a FWHM of 8.6 nm, and 63 MHz focused to a 10μm radius spot, resulting in a fluence of 0.498 mJ/cm^2. The DC bias voltage was set to 100 V, and a characteristic THz trace was detected. The intensity of THz was found to increase with proximity to the anode , matching previous work

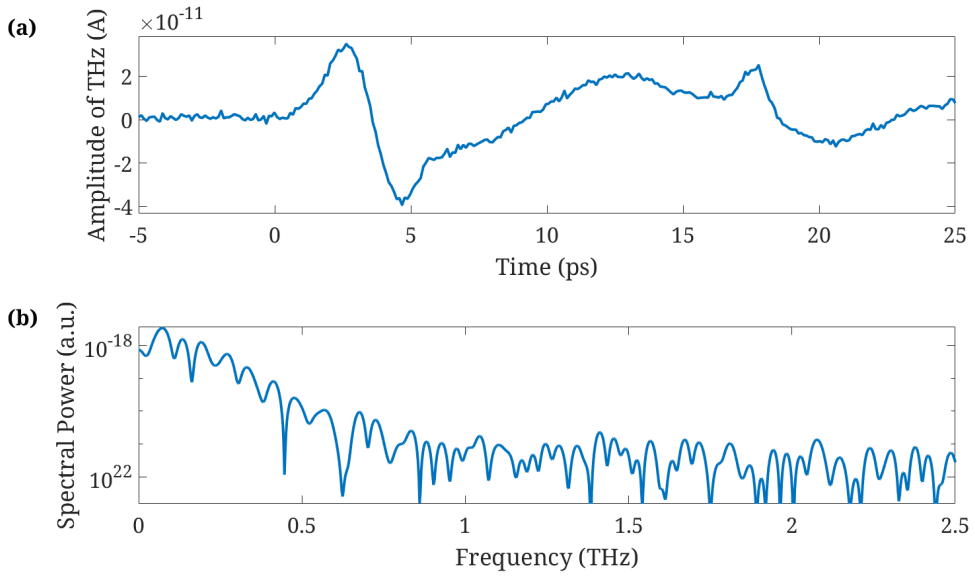

Figure 6.5: *(a) THz time domain trace from a THz SESAM using the fs-Yb source to drive the emission. The primary THz oscillation starts at approximately t = 0 ps and followed by a secondary peak at t = 17.5 ps. (b) The FFT of the THz time domain trace, showing broad THz components up to 0.5 THz approximately 40 dB above the noise floor.*

with stripline emitters in Ralph and Grischkowsky (1991), and Tani et al. (1997). The THz E_{field} was detected via the signal voltage (V_{sig}). V_{sig} is generated by accelerating photocarriers generated in the detector antenna by the probe-pulse. The resulting photocurrent was modulated by an ≈800-Hz optical chopper in the pump-beam, for lock-in amplifier based detection, and the 10-cm variable delay provided up to 667 ps.

Fig.6.5(a) shows the time trace of the THz E_{field}. The primary THz-pulse appears with its first maximum at t = 2.5 ps, and appeared to repeat with a second maximum at t = 17.5 ps. The secondary THz-pulse is attributed to a back reflection in the THz setup, the temporal difference between the two peaks of $\approx \Delta t = 15$ ps, approximately matches the thickness of the PCA-SESAM. The remaining oscillations in the THz trace were attributed to etalon effects, further back reflections and misalignment. Fig.6.5(b) displays the power spectrum of the time domain signal, with an ≈0.5 THz wide peak approximately 40 dB above the noise-floor.

6.2 Conclusions

The results presented in this chapter demonstrate that: an intracavity gold antenna can be added to a VECSEL SESAM structure to produce a device that can be used as both a saturable absorber for mode-locking a VECSEL, and as a stripline antenna for THz emission.

Several key results were obtained during the development of the THz-VECSEL. VECSEL mode-locking was demonstrated for close proximity between the SESAM mode and the strip antenna, with a bias voltage of up to 120 V applied to the structure and a hole was cut into the SESAM heat-sink These conditions were expected to adversely affect mode-locking but the characterisation shown in Fig.6.3 demonstrated that there was little to no effect on the pulse train under the conditions required for the PCA-SESAM to emit THz, indeed producing identical pulse trains for both conditions.

The main difference between the conditions shown for THz emission (Sec.6.1.3) and THz-VECSEL mode-locking (Sec.6.1.2.1) was the fluence applied to drive the THz emission. This is not expected to be a limiting factor for developing the direct emission of THz from the VECSEL because the majority of carriers generated by 1035-nm radiation in the PCA-SESAM structures are expected to be in the InGaAs QW. Therefore for incident radiation at 1035 nm for a given spot size the same population of carriers will be excited up to the limit of QW saturation.

To conclude, this chapter has reported on the research that demonstrates that stable optical pulse trains may be produced by a VECSEL using a device that functions as both a SESAM and a THz PCA, paving the way to a compact system for directly generating both optical and THz-pulses. Not only may this type of device be applied to ML-VECSELs, but any ML laser using a SESAM could be modified to include this device. Future work proposed for the development of the THz-VECSEL and design changes to the PCA-SESAM are discussed in Chapter.7.

Chapter 7

Conclusions and Future Work

7.1 Broadly Repetition-Rate Tunable Laser

To summarise the conclusions of Chapter.2, I have demonstrated the mode-locked performance of a VECSEL cavity designed for large cavity length changes. The performance of the VECSEL demonstrated for the first time a laser capable of mode-locking with sub-300-fs pulse durations, while being continuously tunable from 0.88-1.88 GHz. The tunability of the VECSELs shown here were limited by several factors which can be divided into, cavity mode changes and semiconductor structure properties.

The cavity repetition rate tunability was investigated with the design code presented in Sec.2.3.1. The design code was used to reduce gain-mode size variation, because gain-mode overlap to the pump-spot must be maintained approximately equal over the tuning range to ensure the VECSEL does not decouple from the pump radiation, resulting in variation in intracavity power. Using the design code, the tuning range and mode area were found to be strongly dependent on the selected fold mirror.

The limits on cavity tuning range are imposed by gain saturation, SESAM saturation, cavity lifetime and carrier lifetime. H29 and V623 lasing characteristics were shown to be limited to mode-locking for the pump power and repetition rates shown in Chapter.2.3. However, a new sample pair would need to be designed specifically for operation at higher pump power and larger changes in repetition rate. Therefore, a particular cavity

tuning range and output power will be determined most strongly by the semiconductor structure lasing characteristics.

In addition, the sample pair used for 1035-nm VECSELs (H29 and V623) demonstrated an optical spectrum with a pronounced shoulder for the longer wavelength side of the main peak. This feature could not be analysed due to power constraints, but has been observed in Head et al. (2016) where a FROG measurement was performed. The results of the FROG displayed a trace consistent with third-order spectral phase and negative chirp. Neither of these features cannot be resolved by the intensity autocorrelation, in the data presented for the tZ-cavity VECSEL in this thesis. But irregular pulse shape may be inferred by the optical spectral shapes and the time-bandwidth product which indicates that the gain bandwidth could support a shorter pulse for a lower and flatter GDD.

As described in Sec.2.3.2 the difference between H29 used in this thesis and H28 used by Head et al. (2016) was the number of DQWs, 5 and 4 respectively. This difference contributes directly to the gain of the structure and the GDD, which is why H29 has higher gain and GDD(1035 nm)=-62 (+/- -24/-104) fs^2 and H28 has a more flat GDD profile at 1035-nm, GDD(1035 nm)=-20 (+/- -45/-91) fs^2 (Appendix.A). The lower the GDD and the lower the gradient at the operational wavelength, the closer to transform limited the pulses will be, hence H28 was used to achieve sub-200-fs pulses, while the increased gain of H29 makes it easier for high power applications with pulse durations >200-fs. However, the difference in GDD profiles in Fig.Adx.A.2 is much less than the GDD of the 1035-nm SESAM, V623. As shown in Fig.2.3, the GDD of V623 AT 1035 nm was -687 (+/- -356/-1438) fs^2. Over an order of magnitude larger than H29, pronounced gradient at 1035 nm and with a large variation associated with potential growth error. Therefore the design of this SESAM the dominant effect on phase structure in the pulses from the VECSELs in this research and those in Head et al. (2016).

To solve this problem, it would be necessary to redesign the SESAM structure and grow the new design. Proposed design changes include changes to the QW depth and thickness and the addition of coatings to act as an anti-reflection coating and manage the dispersion (similar to the coating used in H29 in this thesis). The proposed changes

therefore hinge on structure redesigns to increase output power and tunability, and to further reduce pulse durations.

The tZ-cavity VECSELs demonstrated here are viable for resonant and subharmonic excitation of any structure close to GHz. The application selected here was acoustic nanostructure excitation , however, the tZ-cavity may be used for resonant excitation of microresonators and THz-OSCAT (discussed in Sec.7.3).

7.2 GHz Acoustic Nanostructures for Resonant Excitation

Chapters 3 and 4 display the characterisation of two sets of nanostructures, nanowires and nanoantenna/cantilevers. The purpose of these chapters was to test the viability of the samples for use in resonant periodic impact excitation, described in Chapter.5. The work performed in Chapter.5 is the first iteration of a nanostructure acoustic-mode detection scheme based on resonantly exciting the structure with a tunable pulse train emitted directly from a laser (described in Sec.2.3.3).

To predict the acoustic behaviour, an FEM model was used to calculate the structural resonances of nanostructures to aid in selection and design. This model was compared to data from previous research to confirm that it would be a suitable estimate. The model predicted second order modes for the nanowires within range of the VECSEL tunability. In addition, the model helped design and select SiN/An cantilever structures within range for resonant excitation with the tZ-cavity VECSEL.

GaP nanowires of 2.3 μm length were selected for use and an SHG pump-probe experiment was built to test the carrier-relaxation from above-bandgap excitation, and acoustic response was expected to modulate the relaxation. The results of this testing were heavily subject to probe-beam intensity noise, pointing instabilities and structure inhomogeneity. As a result the expected behaviour was not resolvable. Modifications that may improve the signal to noise ratio and allow the effect to be visible are, stable fs laser source, and increased homogeneity of the nanowire sample. Single nanowire interaction may also eliminate the problems caused by inhomogeneity, however the signal

from a single nanowire may be more difficult to retrieve, hence experimentation here being performed on an ensemble of nanowires.

SiN/Au nanoantenna cantilevers were designed specifically for this research following design parameters to produce a near-field enhancement at wavelengths between 800-1000 and acoustic resonances near 1 GHz. Linear spectroscopy of the nanoantenna/cantilevers demonstrated that the nanoantenna dimer design was successful. The sample was also tested with the same SHG pump-probe setup, but due to the difference in structure the excitation was minimal and no acoustic response could be retrieved from the signal produced. Carrier relaxation in the dimer was minimal and it was not possible to resolve time dependent modulations. In addition, the sample contained fabrication defects due to unsuccessful cut-through in the SiN. Length differences and incomplete cut-through can eliminate vibrations or shift their frequency. The fabrication quality of the nanoantenna dimers was more successful as shown in the linear spectroscopy measurements. To improve the homogeneity the structure fabrication-time could be increased, once a structure design was reliably determined. The basic design of the nanoantenna cantilever could also be applied to larger cantilever geometries to harness the LSPP enhanced detection.

Both structures were contained in a retrofitted vacuum chamber which was designed to be approximately double the thickness of the working distance of the focusing objectives. The low profile of the vacuum chamber meant that the sample was mechanically vibrated by the vacuum pump, meaning that the chamber vacuum had to be cut off and slowly vented through the valves. Ideally a larger chamber capable of housing the objectives inside, and withstanding mechanical vibration would be used to isolate the samples.

Therefore for future work on the nanostructures presented in this research, time-domain and frequency-domain measurements would both benefit from changes to sample isolation, power handling and homogeneity.

In the frequency domain the signal may be retrievable with a more sensitive photodiode. The frequency-domain setup sensitivity was limited by the 25-GHz photodiode selected for this experiment. The photodiode had sufficient bandwidth to detect oscillations on the 1 - 2 GHz scale, however, the comparatively low sensitivity (conversion gain of 15

V/W) and the fibre coupling reduced the available modulation signal and the setup's ability to detect it. To increase the sensitivity of the setup a different photodiode can be used as much higher sensitivities (conversion gain of ≈1000 V/W) are available for a lower bandwidth of 2 GHz. The lower bandwidth would not limit the experiment, except for detection of higher order modes being driven by sub-harmonic pumping from the VECSEL. Finally a motorised stage for the VECSEL OC would allow fast scanning of f_{Rep}, resulting in large improvements to resolution.

7.3 Intracavity PCA-SESAM for VECSEL THz Emission

In Chapter.6, I have demonstrated that a PCA-SESAM device was able to mode-lock the output of a VECSEL, under conditions necessary for intracavity THz emission. The mode-locking was unaffected by the conditions of THz-generation and the proximity of the laser mode on the SESAM was less critical on mode-locking quality than expected. These results mean that an intracavity THz VECSEL can be designed with a smaller PCA gap, which reduces the constraint on high-voltage bias and makes it more feasible to directly modulate the bias voltage in the kHz range (increased from ≈800 Hz).

For future work on the THz-VECSEL Fig.7.1 shows the setup proposed to demonstrate the simultaneous use of the PCA-SESAM for IR-pulse formation and THz-pulse generation. The setup was built to perform pulse train analysis in Sec.6.1.2.1, however, THz-TDS could not be performed with a mechanical chopper (discussed in Sec.6.1.2.1). This intracavity-TDS setup only differs from the fs-Yb setup shown in Fig.6.4 in two respects: it uses the intracavity mode as the seed-pulse and adds the variable delay to the probe-beam.

Instead of using a beam splitter as shown in Sec.6.1.3 for conventional THz-TDS. For direct VECSEL THz-TDS, the beam separation into pump and probe beams is performed at the SESAM where the IR-pulse is reflected and the THz-pulse is both generated and transmitted. Direct THz-TDS from a THz-VECSEL is performed with the THz and IR outputs from the THz-VECSEL with the same method and components as those

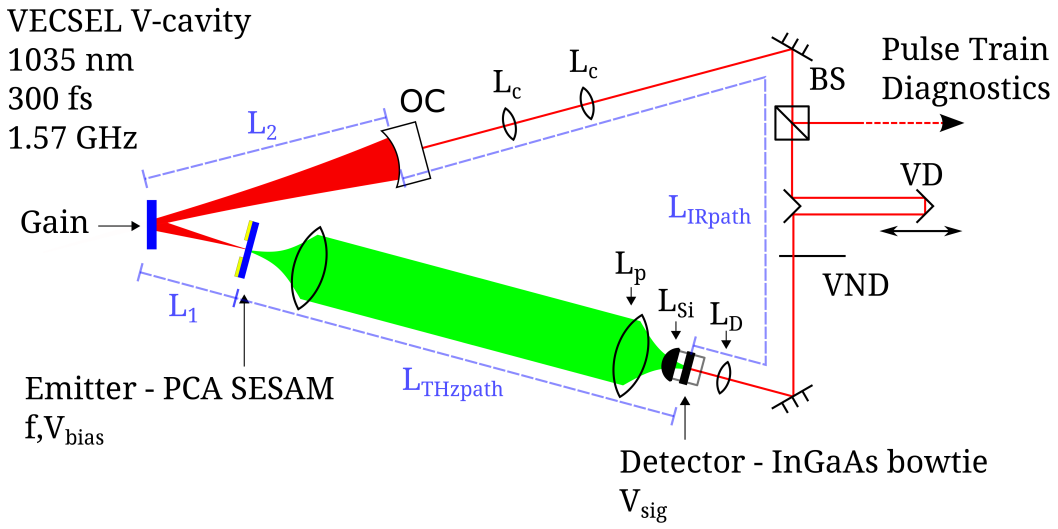

Figure 7.1: *A schematic diagram of THz time-domain spectroscopy setups based around intracavity laser mode in a ML-VECSEL as designed in Chapter.6. The THz pulse travels a distance $L_{THzpath}$. Due to the cavity length of the VECSEL ($L_1 + L_2$) and the length of optics to get the seed pulse to the detector (L_{IRpath}), a pulse n arrives at the detector with the THz-pulse n+5.*

used for TDS performed in Sec.6.1.3. The difference in path length (ΔL) between the IR-pulse and THz-pulse arriving at the detector is given by:

$$\Delta L = L_1 + L_2 + L_{IRpath} - L_{THzpath} \tag{7.1}$$

where the length terms are defined in Fig.7.1, experimentally it was possible to compress the setup to $L_{IRpath} = 103$ cm and $L_{THzpath} = 26$ cm. Therefore, ΔL corresponds to ns, as a result the setup is designed to use the nth pulse to probe the effect of the $(n-5)th$ pulse as pump for THz generation. Since the coherence length of the laser is many roundtrips longer than the 5 round trip difference at the detector, the nth and $(n+5)th$ pulses can be considered identical.

The setup shown in Fig.7.1 was built and successfully used to characterise the VECSEL mode-locking behaviour. The limitation was given by the lack of an AC current driver capable of fast modulation. Optical chopping was shown to destabilise the laser causing it to drop out of ML and lase in CW. Therefore to develop the THz-VECSEL with the same design of PCA-SESAM, a kHz 100-V voltage driver will be required. Reducing the bias voltage may also improve the lifetime of the PCA-SESAM, since prolonged application of

a high voltage bias may lead to semiconductor carrier electro-migration, causing current to no longer flow-properly. It is also possible to redesign the SESAM to reduce the gap, thereby reducing the bias voltage required, or produce Photo-Dember patterns on the surface which emit THz with no bias voltage applied. Lastly, the demonstration of tZ-cavity operation in Chapter.2, and the PCA-SESAM in Chapter.6 can be combined to produce an OSCAT measurement by adding the PCA-SESAM to the tZ-cavity VECSEL. The resulting system will be an even more compact solution to THz-TDS measurements.

Chapter 8

List of Publications

T. Chen Sverre ; C. R. Head ; A. P. Turnbull ; E. A. Shaw ; A. C. Tropper ; O. L. Muskens Tunable repetition rate VECSEL for resonant acoustic-excitation of nanostructures SPIE Photonics West (Feb 2016)

T. Chen Sverre , A. P. Turnbull, P. C. Gow, E. Mavrona , V. Apostoulopoulos , and A. C. Tropper Mode-locked VECSEL SESAM with Intracavity Antenna for Terahertz Emission In press, SPIE Photonics West (Jan 2017)

A. P. Turnbull, C. R. Head, E. A. Shaw, T. Chen-Sverre, and A. C. Tropper Spectrally resolved pulse evolution in a mode-locked vertical-external-cavity surface-emitting laser from lasing onset measurements SPIE Photonics West (Feb 2015)

Ed A. Shaw, Adrian H. Quarterman, Andrew P. Turnbull, Theo Chen Sverre, C. Robin Head, Anne C. Tropper, and Keith G. Wilcox Nonlinear Lensing in an Unpumped Antiresonant Semiconductor Disk Laser Gain Structure IEEE Photonics Technology Letters, Vol. 28, No. 13, (July 2016)

C. R. Head ; Alexander Hein ; Andrew P. Turnbull ; Markus Polanik ; Edward A. Shaw ; Theo Chen Sverre ; Peter Unger ; Anne C. Tropper High-order dispersion in sub-200-fs pulsed VECSELs SPIE Photonics West (Feb 2016)

Ed A. Shaw ; Adrian H. Quarterman ; Andrew P. Turnbull ; Theo Chen Sverre; C. R. Head ; Anne C. Tropper ; Keith G. Wilcox Reflection z-scan measurements of the non-linear lens in VECSEL gain structures SPIE Photonics West (Feb 2016)

Appendix A

VECSEL Structures

Adx.Fig.A.2 shows the calculated GDD and $E_{field}{}^2$ and reflectivity as a function of wavelength between the sample used for this research (H29) and that used for research by Head *et, al.* (2016). The key difference between the samples is the change in number of QWs, which is visible between these calculations as a reduction in GDD and a broadening

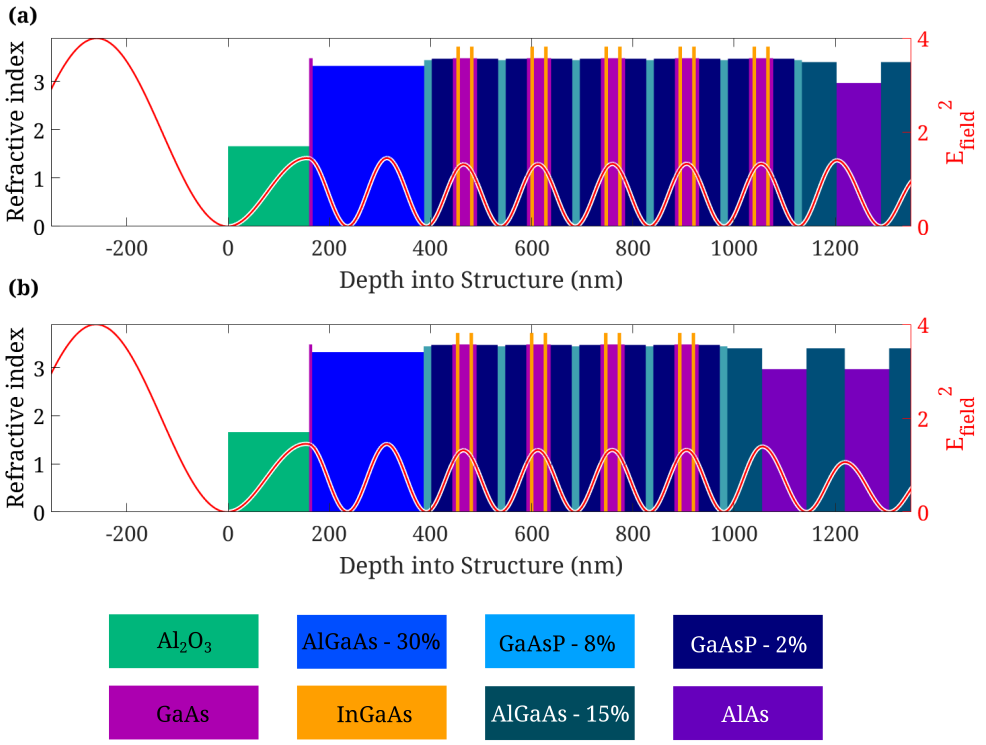

Figure A.1: Structure designs for H28 and H29 used for GDD, $E_{field}{}^2$ and reflectivity calculations in Adx.Fig.A.2.

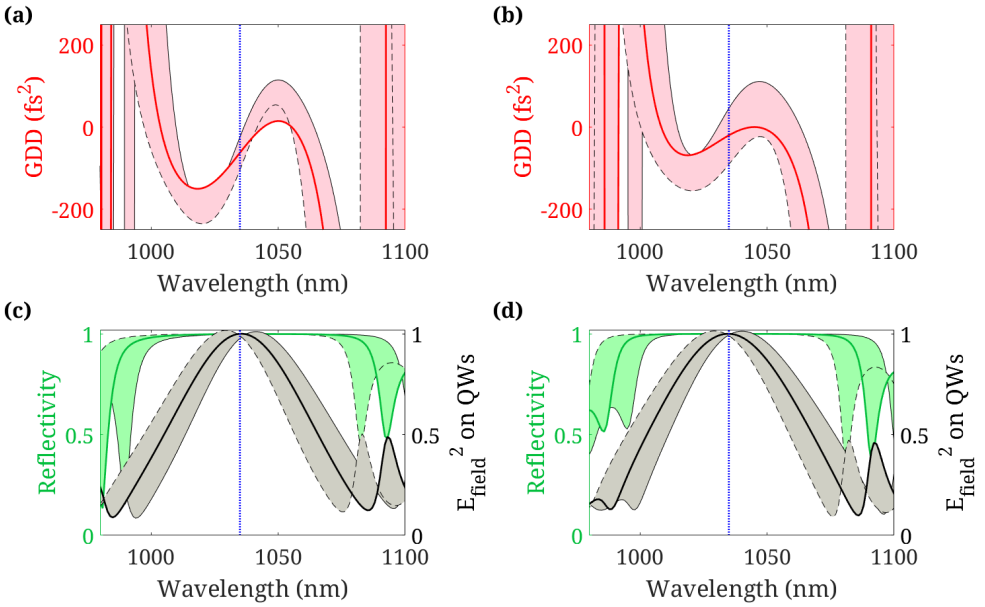

Figure A.2: *Layer-list calculations for 1035-nm gain structures H29 5-DQW gain-structure (a and c), and H28 5-DQW gain structure reported in Head et. al. (2016) (b and d). GDD (red) for (a) the gain stucture and (b) the SESAM, Reflectivity (green) and* $E_{field}{}^2$ *on the QWs for (c) the gain stucture and (d) the SESAM. All are displayed with filled areas corresponding to -1% (dashed) and +1% (solid) growth error, and the design wavelength of 1035 nm (dashed blue).*

in enhancement profile. Structure designs for H28 and H29 calculations are shown in Adx.Fig.A.1.

Appendix B

tZ-Cavity Mode Calculations

First the optical resonator matrix, $M_{resonator}$, is evaluated over a nested loop for L_1 and L_3, calculating $M_{resonator}$ for all combinations of L_1 and L_3 in specified ranges. The ranges of these loops was selected to display: the desired L_3 tunability (≈40-140 mm) and L_1 large enough to find the value of lowest variation for gain mode and area ratio (≈3-5 mm). M_{L_2} is held at a fixed value per code evaluation, therefore, the code must be run multiple times to optimise the L_2 value for a particular gain-mode waist, which is set experimentally by the pump-spot.

Once $M_{resonator}$ has been calculated for a combination of L_1 and L_3, the Rayleigh range of the resonator z_R can be calculated by:

$$z_R = \sqrt{\frac{-B}{C}} \tag{B.1}$$

Where B and C are given in Equation.2.2. Once the Rayleigh range has been calculated, the SESAM-mode waist can be calculated using:

$$\begin{aligned} w_{SESAM} &= w_0 \\ &= |\sqrt{z_R \lambda/\pi}| \end{aligned} \tag{B.2}$$

$$q = z + iz_R \tag{B.3}$$

Where z=0 for the q at the SESAM. By calculating the complex beam parameter q at the SESAM the complex parameter was calculated at a propagation distance z from the cavity focus q_z.

Therefore the mode-waist at the gain-structure was calculated by evaluating a matrix ABCD for the gain position in the cavity relative to the SESAM, z (Equation.B.4). Therefore, new beam parameter q_z can be calculated using Equation.B.5 where z=L_1 for Gain.

$$\begin{bmatrix} A & B \\ C & D \end{bmatrix} = \begin{bmatrix} 1 & z \\ 0 & 1 \end{bmatrix} \tag{B.4}$$

$$q_z = \frac{Cq + D}{Bq + A} \tag{B.5}$$

Finally, the beam radius can be calculated with the imaginary component of q_z:

$$w_z = \left| \sqrt{\frac{\lambda}{\pi Im[q_z]}} \right| \tag{B.6}$$

And the area ratio is given by the ratio of squares of the gain and SESAM mode waists:

$$AreaRatio = \frac{w_{gain}^2}{w_{SESAM}^2} \tag{B.7}$$

The surfaces plotted in Fig.B.1, Fig.B.2 and Fig.B.3 are calculated using the method outlined here for a 1035-nm VECSEL tZ-cavity. The calculated lowest standard deviations of the gain-mode waist and area-ratio for changes in L_3 have been plotted in green and black respectively. The result of the code is that between lines corresponding to the two values of L_1 is the most stable cavity design for large changes in L_3. The achieved repetition rate tuning ranges are displayed as the red and blue lines for 0.88 -1.88 GHz and 0.96 - 1.72 GHz respectively.

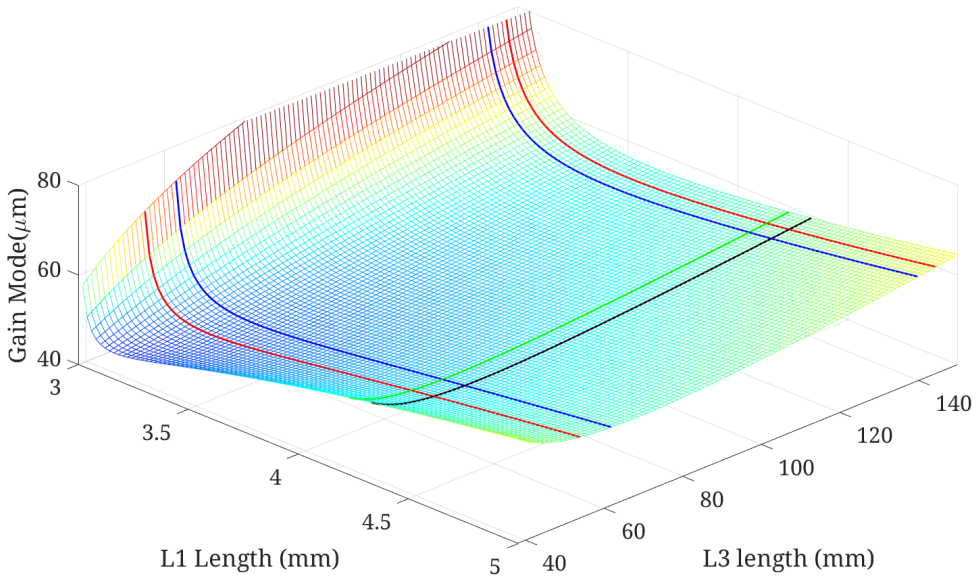

Figure B.1: *tZ-cavity gain-mode radius as a function of variations in L_1 L_3 for a fixed L_2=22 mm (lengths defined in Fig.2.11).*

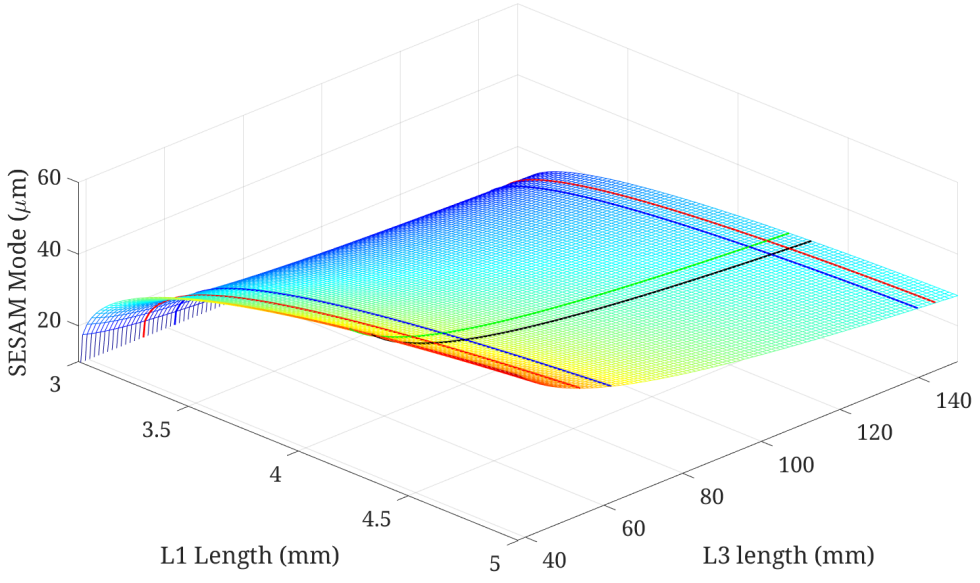

Figure B.2: *tZ-cavity SESAM-mode radius as a function of variations in L_1 L_3 for a fixed L_2=22 mm (lengths defined in Fig.2.11).*

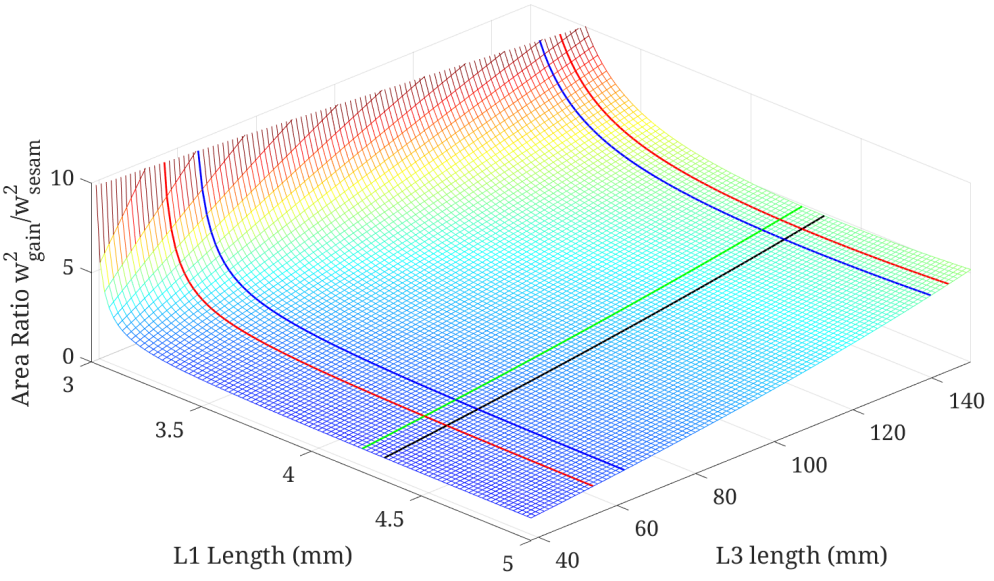

Figure B.3: *tZ-cavity area-ratio as a function of variations in L_1 L_3 for a fixed L_2=22 mm (lengths defined in Fig.2.11).*

Appendix C

V-cavity Mode Calculations

Cavity mode calculations for the V-cavity VECSEL described in Sec.2.2.1. These calculations were performed using a similar method to that shown in Appendix.B but for a V-cavity round-trip matrix. The cavity lengths selected for experimentation, L_1= 68.8 mm and L_2= 5.8 mm, are displayed on the figures Fig.C.1, Fig.C.2(a) and Fig.C.2(b). As shown in Fig.C.1, the gain mode variation is saddle shaped meaning that simultaneous changes in L_1 and L_2 may be required to optimise the laser cavity power. As shown

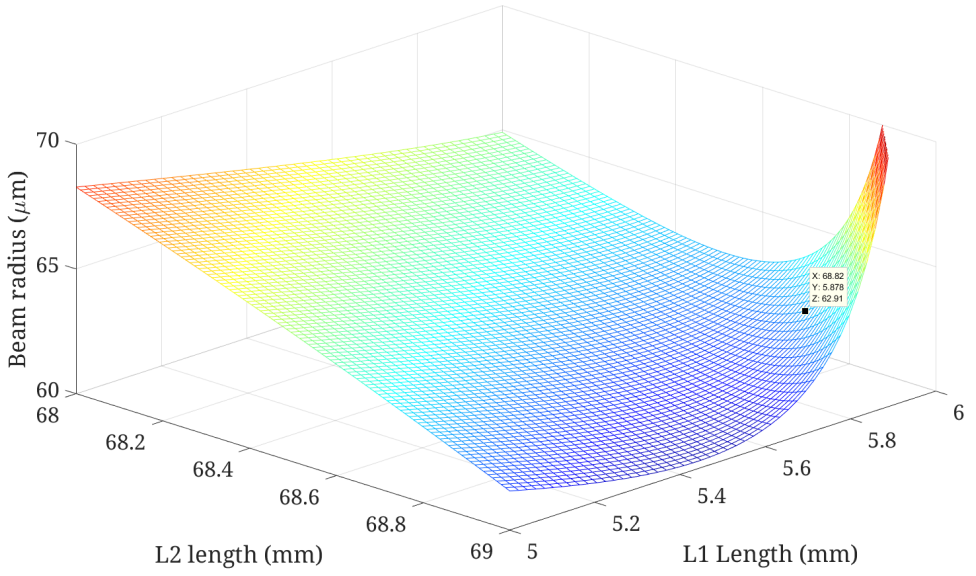

Figure C.1: *V-cavity gain-mode radius as a function of variations in L_1 L_2 for the closest integer length in mm to the lengths defined in Fig.2.9. Marker displays the selected lengths and resulting w_{gain} = 63 μm.*

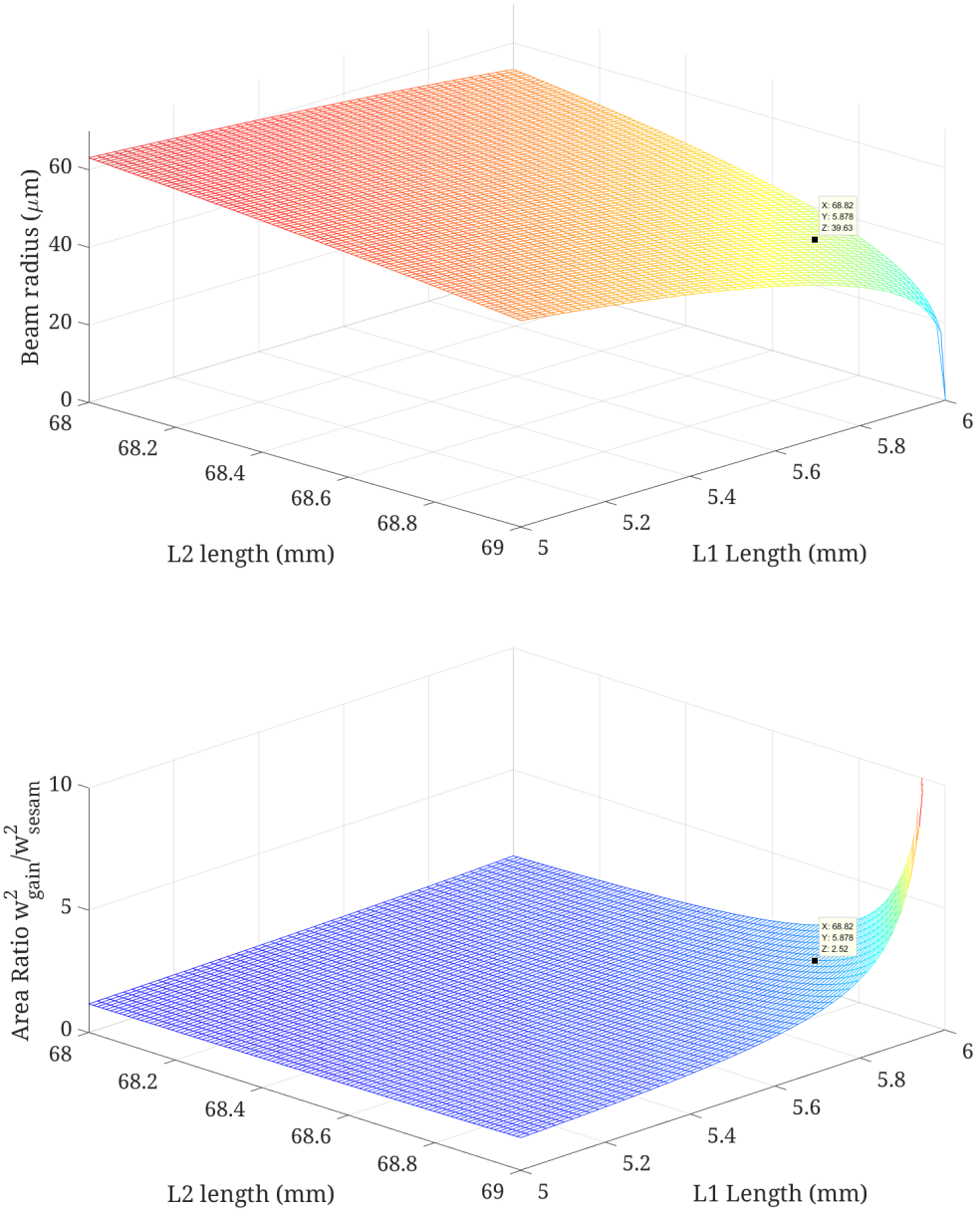

Figure C.2: *(a) V-cavity SESAM-mode as a function of variations in L_1 L_2 for the closest integer length in mm to the lengths defined in Fig.2.9. Marker displays the selected lengths and resulting $w_{SESAM} = 40$ μm. (b) V-cavity area-ratio as a function of variations in L_1 L_2 for the closest integer length in mm to the lengths defined in Fig.2.9. Marker displays the selected lengths and resulting area-ratio = 2.5.*

in figures Fig.C.2(a) and Fig.C.2(b) the area-ratio strongly depends on the SESAM-mode radius, which decreases mode uniformly toward larger values of both L_1 and L_2.

Appendix D

SEM Record

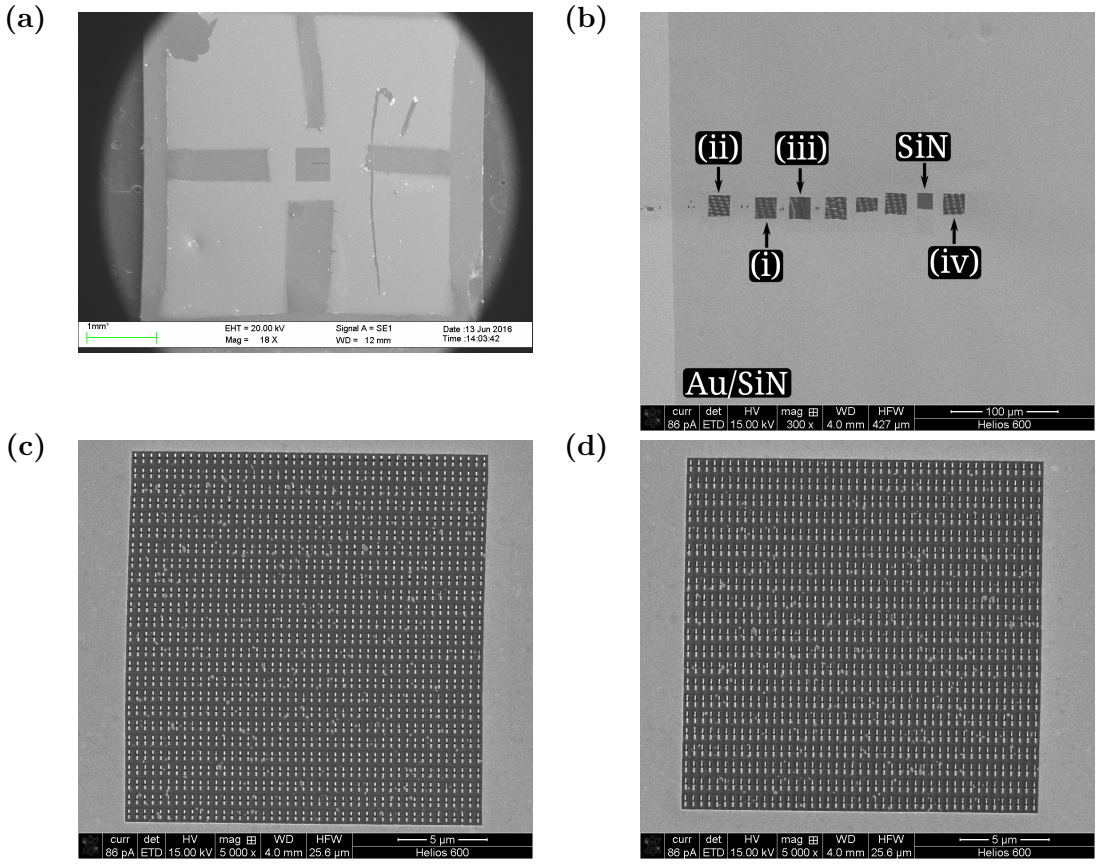

Figure D.1: *SEM of the SiN/ Au nanoantenna cantilevers. (a) Full sample displaying the membrane, dark square in the middle, with the sample sites to the right of the membrane. (b) Locations of sample sites i-iv and SiN. (c) Sample site (iii) and (d) (iv), displaying 25x25 dimers.*

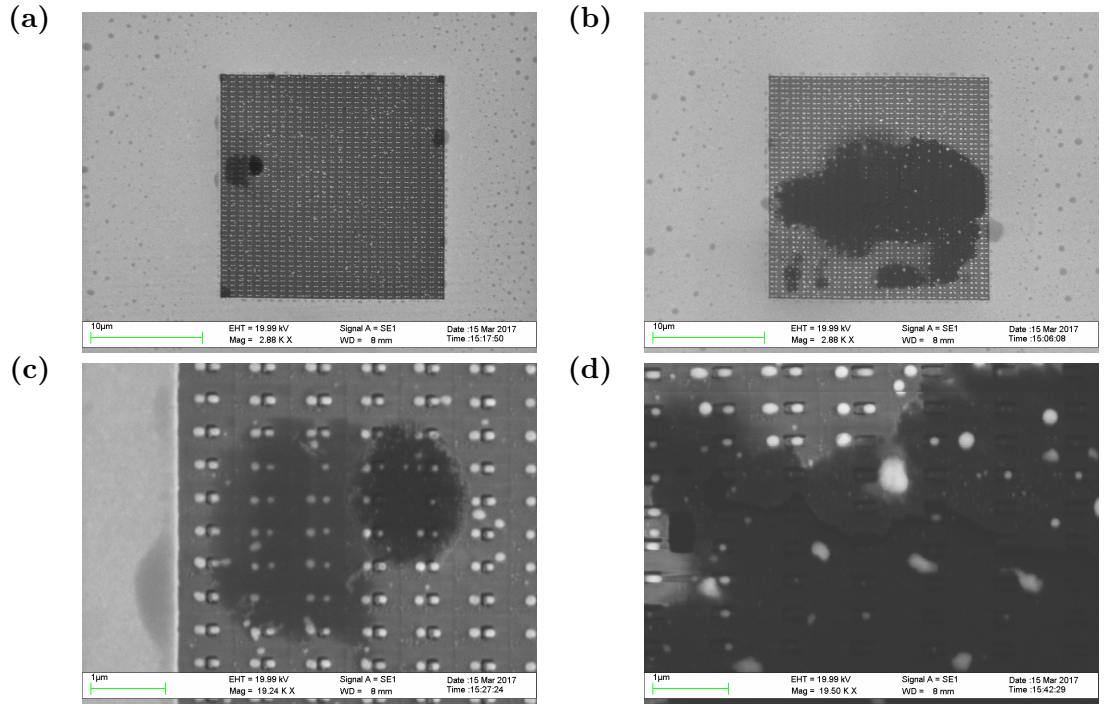

Figure D.2: SEM of metamaterial on SiN/Au nanomembrane laser damage. (a and b) coarse detail and (c and d) fine detail, of damage sites on sample sites iii and iv respectively.

Appendix E

Periodic Impact Excitation of a Classical Oscillator

Considering a damped driven classical oscillator with displacement $y(t)$:

$$\frac{d^2y}{dt^2} + 2\gamma\frac{dy}{dt} + \omega_0^2 y = F(t)$$

,where γ is the damping constant, ω_0^2 is the spring constant, $F(t)$ is the driving force. For the case of a free running oscillator,

$$F(t) = 0 \qquad \text{and} \qquad y = y_0 e^{i\omega t}$$

,substituted into equation for a free running oscillator and using the quadratic formula,

$$\omega = \frac{2i\gamma + \pm\sqrt{-4\gamma^2 + 4\omega_0^2}}{2}$$

,this can be used to show displacement has a general solution,

$$y(t) = Ae^{i\omega_1 t} + Be^{i\omega_2 t}$$

$$y(t) = Ae^{(-\gamma+i\sqrt{\omega_0^2-\gamma^2})t} + B^{(-\gamma-i\sqrt{\omega_0^2-\gamma^2})t}$$

$$y(t) = [y_{phase}\sin(t\sqrt{\omega_0^2-\gamma^2}) + y_{quad}\sin(t\sqrt{\omega_0^2-\gamma^2})]e^{-\gamma t}$$

,where it is assumed that $\omega_0^2 > y^2$, otherwise the oscillator is over-damped,

$$Q = \frac{\text{stored energy}}{\text{energy dissipated/radian}} = \frac{\omega_0}{2\gamma}$$

Now consider for an impulse driven oscillator - impulse I [Ns] at time $t = 0$, where $\delta(t)$ is the Dirac delta function:

$$F(t) = I\delta(t) \qquad \text{and} \qquad \left.\frac{dy}{dt}\right|_{t-0} = \frac{I}{m}$$

$$y(t) = \frac{I}{m\omega}\sin(\omega t)e^{\gamma t} \qquad \text{where:} \qquad \omega = \sqrt{\omega_0^2-\gamma^2}$$

The impulse response leads to a formal solution to the general driven oscillator problem. Response to a unit impulse at time t', $\delta(t-t')$, is the Green function:

$$G(t-t') = \frac{1}{m\omega}\sin(\omega(t-t'))e^{-\gamma(t-t')}$$

where for causality: $t > t'$, and $G(t-t') = 0$ if $t \leq t'$. The general form of the driving force is:

$$F(t) = \int F(t')\delta(t-t')dt'$$

Because the equation of motion is linear we can use superposition,

$$y(t) = \frac{1}{m\omega} \int F(t') \sin(\omega(t-t')) e^{-\gamma(t-t')} dt'$$

For the case of periodic impulse impact excitation we consider unit impulses separated in time by $T_0 = \frac{2\pi}{\omega} = \frac{2\pi}{\sqrt{\omega_0^2 - \gamma^2}}$. We are not interested in transient build-up, only in the steady state of the forced oscillator after an infinite number of impulses, i.e. a number large compared to:

$$\frac{\text{oscillator decay time}}{\text{time between pulses}} = \frac{\frac{1}{\gamma}}{\frac{2\pi}{\omega}}$$

Considering the superposition of the relaxation of impulses for a resonant case where $\omega_0 = \omega$,

$$y(t) = \sum_{n=1}^{\infty} y_n(t) = \frac{1}{m\omega} \sum_{n=0}^{\infty} \sin(\omega[t + n\frac{2\pi}{\omega}]) e^{-\gamma(t+n\frac{2\pi}{\omega})}$$

,where,

$$\gamma T_0 \ll 1 \qquad \therefore \qquad e^{-\gamma T_0} \approx 1 - \gamma T_0$$

$$y(t) = \frac{1}{m\omega} \sin(\omega t) e^{-\gamma t} \sum_{n=0}^{\infty} e^{-n\gamma T_0}$$

,where the sum is approximated by,

$$S_N = \frac{1 - a^{N+1}}{1 - a} \qquad \text{for:} |a| < 1 \qquad S_N \approx \frac{1}{1 - a}$$

$$y(t) = \frac{1}{m\omega} \sin(\omega t) e^{-\gamma t} \frac{1}{1 - e^{-\gamma T_0}}$$

Now to estimate the response use $\gamma = \frac{\omega_0}{2Q}$, $\omega = \sqrt{\omega_0^2 - \frac{\omega_0^2}{4Q^2}} = \omega_0 \sqrt{1 - \frac{1}{4Q^2}}$

For a $Q \geq 5$, ω is at least 99% of ω_0, therefore we will approximate them as the same,

$$\gamma T_0 = \frac{\omega_0}{2Q}\frac{2\pi}{\omega} = \frac{\pi}{Q}\frac{\omega_0}{\omega} \approx \frac{\pi}{Q}$$

$$\therefore if \qquad \frac{T_0}{T}\frac{Q}{\pi} > 1,$$

then periodic impact excitation will induce a larger amplitude of vibration than can be achieved by a low repetition-rate laser of the same average power.

References

Martina Abb, Yudong Wang, Nikitas Papasimakis, C. H. De Groot, and Otto L. Muskens. Surface-enhanced infrared spectroscopy using metal oxide plasmonic antenna arrays. *Nano Letters*, 14(1):346–352, 2014. ISSN 15306984. doi: 10.1021/nl404115g. URL http://pubs.acs.org/doi/abs/10.1021/nl404115g.

J. Aizpurua, Garnett W. Bryant, Lee J. Richter, F. J. García De Abajo, Brian K. Kelley, and T. Mallouk. Optical properties of coupled metallic nanorods for field-enhanced spectroscopy. *Physical Review B - Condensed Matter and Materials Physics*, 71(23): 1–13, 2005. ISSN 10980121. doi: 10.1103/PhysRevB.71.235420.

A. Arbouet, N. Del Fatti, and F. Vallee. Optical control of the coherent acoustic vibration of metal nanoparticles. *Journal of Chemical Physics*, 124(14), 2006. ISSN 00219606. doi: 10.1063/1.2185631. URL http://aip.scitation.org/doi/10.1063/1.2185631.

D. H. Auston, K. P. Cheung, and P. R. Smith. Picosecond photoconducting Hertzian dipoles. *Applied Physics Letters*, 45(3):284–286, 1984. ISSN 00036951. doi: 10.1063/1.95174.

K. Babaei Gavan. *Dynamic Characterization of Silicon Nitride Cantilevers*. PhD thesis, Kavli Institute of Nanoscience, 2009. URL http://repository.tudelft.nl/islandora/object/uuid:f204c1de-bb92-4689-853d-71183b86a340?collection=research.

K Babaei Gavan, E W J M van der Drift, W J Venstra, M R Zuiddam, and H S J van der Zant. Effect of undercut on the resonant behaviour of silicon nitride cantilevers.

Journal of Micromechanics and Microengineering, 19(3):035003, 2009. ISSN 0960-1317. doi: 10.1088/0960-1317/19/3/035003.

Matthew C. Beard, Gordon M. Turner, and Charles A. Schmuttenmaer. Terahertz spectroscopy. *Journal of Physical Chemistry B*, 106(29):7146–7159, 2002. ISSN 10895647. doi: 10.1021/jp020579i.

Jean-charles Beugnot and Vincent Laude. Electrostriction and guidance of sound by light in optical fibers. (4), 2012.

Palash Bharadwaj, Bradley Deutsch, and Lukas Novotny. Optical Antennas. *Advances in Optics and Photonics*, 1(3):438, 2009. ISSN 1943-8206. doi: 10.1364/AOP.1.000438. URL https://www.osapublishing.org/aop/abstract.cfm?uri=aop-1-3-438.

P. G. Datskos, N. V. Lavrik, and S. Rajic. Performance of uncooled microcantilever thermal detectors. *Review of Scientific Instruments*, 75(4):1134–1148, 2004. ISSN 00346748. doi: 10.1063/1.1667257.

T. Dekorsy, R. Taubert, F. Hudert, a. Bartels, a. Habenicht, F. Merkt, P. Leiderer, K. Köhler, J. Schmitz, and J. Wagner. Coherent acoustic phonons in nanostructures. *Proceedings of SPIE*, 6892:68920E–68920E–8, 2008. ISSN 0277786X. doi: 10.1117/12.760395. URL http://link.aip.org/link/PSISDG/v6892/i1/p68920E/s1{&}Agg=doi.

N. Del Fatti, C. Voisin, F. Chevy, F. Vallee, and C. Flytzanis. Coherent acoustic mode oscillation and damping in silver nanoparticles. *The Journal of Chemical Physics*, 110 (23):11484, 1999. ISSN 00219606. doi: 10.1063/1.479089. URL http://scitation.aip.org/content/aip/journal/jcp/110/23/10.1063/1.479089.

S L Dexheimer. *Terahertz Spectroscopy: Principles and Applications*. CRC Press, 2008. URL https://books.google.co.uk/books?id=6cl3EXZ6x{_}wC{&}pg=PP8{&}source=gbs{_}selected{_}pages{&}cad=3{#}v=onepage{&}q{&}f=false.

L. Ding, C. Baker, P. Senellart, A. Lemaitre, S. Ducci, G. Leo, and I. Favero. Wavelength-sized GaAs optomechanical resonators with gigahertz frequency. *Applied Physics Letters*, 98(11), 2011. ISSN 00036951. doi: 10.1063/1.3563711.

K. L. Ekinci and M. L. Roukes. Nanoelectromechanical systems. *Review of Scientific Instruments*, 76(6):1–12, 2005. ISSN 00346748. doi: 10.1063/1.1927327.

Bradley Ferguson and Xi-Cheng Zhang. Materials for terahertz science and technology. *Nature Materials*, 1(1):26–33, 2002. ISSN 14761122. doi: 10.1038/nmat708. URL http://www.nature.com/doifinder/10.1038/nmat708.

Martin E. Fermann, Galvanauskas Almantas, and Gregg Sucha. *Ultrafast Lasers*. Taylor & Francis e-Library, isbn: 0-82 edition, 2005. URL https://books.google.co.uk/books?hl=en{&}lr={&}id=i8NvQbG5t{_}8C{&}oi=fnd{&}pg=PP1{&}dq=review+of+commercial+ultrafast+lasers{&}ots=T6nfqsCYNR{&}sig=mumM984LYWU{_}XB2j5EyjhWPPpOQ{#}v=onepage{&}q=reviewofcommercialultrafastlasers{&}f=false.

Fitriani, R. Ovik, B. D. Long, M. C. Barma, M. Riaz, M. F M Sabri, S. M. Said, and R. Saidur. A review on nanostructures of high-temperature thermoelectric materials for waste heat recovery. *Renewable and Sustainable Energy Reviews*, 64:635–659, 2016. ISSN 18790690. doi: 10.1016/j.rser.2016.06.035. URL http://dx.doi.org/10.1016/j.rser.2016.06.035.

Z Q Gao, A Agarwal, A D Trigg, N Singh, C Fang, C H Tung, Y Fan, K D Buddharaju, and J M Kong. Silicon nanowire arrays for label-free detection of DNA. *Analytical Chemistry*, 79(9):3291–3297, 2007. ISSN 0003-2700. doi: 10.1021/ac061808q.

A. Garnache, S. Hoogland, A. C. Tropper, I. Sagnes, G. Saint-Girons, and J. S. Roberts. Sub-500-fs soliton-like pulse in a passively mode-locked broadband surface-emitting laser with 100 mW average power. *Applied Physics Letters*, 80(21):3892–3894, 2002. ISSN 00036951. doi: 10.1063/1.1482143.

Wb Gauster and Dh Habing. Electronic volume effect in silicon. *Physical Review Letters*, 18:1058–1061, 1967. URL http://prl.aps.org/abstract/PRL/v18/i24/p1058{_}1.

Yannick Guillet, Bertrand Audoin, Mélanie Ferrié, and Serge Ravaine. All-optical ultrafast spectroscopy of a single nanoparticle-substrate contact. *Physical Review B*

- *Condensed Matter and Materials Physics*, 86(3):1–5, 2012. ISSN 10980121. doi: 10.1103/PhysRevB.86.035456.

Gregory V. Hartland. Coherent vibrational motion in metal particles: Determination of the vibrational amplitude and excitation mechanism. *The Journal of Chemical Physics*, 116(18):8048, 2002. ISSN 00219606. doi: 10.1063/1.1469021. URL http://scitation.aip.org/content/aip/journal/jcp/116/18/10.1063/1.1469021.

Gregory V Hartland. Coherent excitation of vibrational modes in metallic nanoparticles. *Annual review of physical chemistry*, 57(13):403–430, 2006. ISSN 0066-426X. doi: 10.1146/annurev.physchem.57.032905.104533.

Seyyed M. Hasheminejad and Behnam Gheshlaghi. Dissipative surface stress effects on free vibrations of nanowires. *Applied Physics Letters*, 97(25), 2010. ISSN 00036951. doi: 10.1063/1.3528212.

C. R. Head, Alexander Hein, Andrew P. Turnbull, Markus Polanik, Edward A. Shaw, Theo Chen Sverre, Peter Unger, and Anne C. Tropper. High-order dispersion in sub-200-fs pulsed VECSELs. 9734(973408):1–10, 2016. doi: 10.1117/12.2212690. URL http://proceedings.spiedigitallibrary.org/proceeding.aspx?doi=10.1117/12.2212690.

B. Heinen, T.-L. Wang, M. Sparenberg, a. Weber, B. Kunert, J. Hader, S.W. Koch, J.V. Moloney, M. Koch, and W. Stolz. 106 W continuous-wave output power from vertical-external-cavity surface-emitting laser. *Electronics Letters*, 48(9):516, 2012. ISSN 00135194. doi: 10.1049/el.2012.0531. URL http://digital-library.theiet.org/content/journals/10.1049/el.2012.0531.

K Imura, T Nagahara, and H Okamoto. Imaging of surface plasmon and ultrafast dynamics in gold nanorods by near-field microscopy. *J. Phys. Chem. B*, 108(42): 16344–16347, 2004. ISSN 1520-6106. doi: 10.1021/jp047950h.

Hermann Kahle, Cherry M. N. Mateo, Uwe Brauch, Roman Bek, Thomas Schwarzbäck, Michael Jetter, Thomas Graf, and Peter Michler. Gain chip design, power scaling and intra-cavity frequency doubling with LBO of optically pumped red-emitting AlGaInP-VECSELs. *Proc. SPIE 9734*, 9734

(0):97340T–97340T–6, 2016. ISSN 1996756X. doi: 10.1117/12.2209305. URL http://dx.doi.org/10.1117/12.2209305{%}5Cnhttp://proceedings.spiedigitallibrary.org/proceeding.aspx?doi=10.1117/12.2209305.

M. S. Kang, a. Nazarkin, a. Brenn, and P. St. J. Russell. Tightly trapped acoustic phonons in photonic crystal fibres as highly nonlinear artificial Ramanoscillators. *Nature Physics*, 5(4):276–280, mar 2009. ISSN 1745-2473. doi: 10.1038/nphys1217. URL http://www.nature.com/doifinder/10.1038/nphys1217.

Artemios Karvounis, Jun-Yu Ou, Weiping Wu, Kevin F. MacDonald, and Nikolay I. Zheludev. Nano-optomechanical nonlinear dielectric metamaterials. *Applied Physics Letters*, 107(19):191110, 2015. ISSN 0003-6951. doi: 10.1063/1.4935795. URL http://scitation.aip.org/content/aip/journal/apl/107/19/10.1063/1.4935795.

U. Keller. Ultrafast solid-state laser oscillators: A success story for the last 20 years with no end in sight. *Applied Physics B: Lasers and Optics*, 100(1):15–28, 2010. ISSN 09462171. doi: 10.1007/s00340-010-4045-3.

Ursula Keller and Anne C. Tropper. Passively modelocked surface-emitting semiconductor lasers. *Physics Reports*, 429(2):67–120, jun 2006. ISSN 03701573. doi: 10.1016/j.physrep.2006.03.004. URL http://linkinghub.elsevier.com/retrieve/pii/S037015730600127X.

P. Klopp, U. Griebner, M. Zorn, and M. Weyers. Pulse repetition rate up to 92 GHz or pulse duration shorter than 110 fs from a mode-locked semiconductor disk laser. *Applied Physics Letters*, 98(7):071103, 2011. ISSN 00036951. doi: 10.1063/1.3554751. URL http://scitation.aip.org/content/aip/journal/apl/98/7/10.1063/1.3554751.

Alexandre a Kolomenskii, Sergey N Jerebtsov, Haidong Liu, Hong Zhang, Zuxin Ye, Zhiping Luo, Wenhao Wu, and Hans a Schuessler. Dynamics of coherent acoustic and optical phonon oscillations in nanostructures studied by a femtosecond pump-probe technique. *Journal of Physics: Conference Series*, 214:012012, 2010. ISSN 17426588. doi: 10.1088/1742-6596/214/1/012012. URL http://iopscience.iop.org/1742-6596/214/1/012012.

Jörg P. Kottmann and Olivier J.F. Martin. Plasmon resonant coupling in metallic nanowires. *Optics Express*, 8(12):655, 2001. ISSN 1094-4087. doi: 10.1364/OE.8.000655. URL https://www.osapublishing.org/abstract.cfm?URI=oe-8-12-655.

Tevye Kuykendall, Peter J Pauzauskie, Yanfeng Zhang, Joshua Goldberger, Donald Sirbuly, Jonathan Denlinger, and Peidong Yang. Crystallographic alignment of high-density gallium nitride nanowire arrays. *Nature materials*, 3(August):524–528, 2004. ISSN 1476-1122. doi: 10.1038/nmat1177. URL http://www.nature.com/nmat/journal/v3/n8/full/nmat1177.html.

Mark Kuznetsov, Farhad Hakimi, Robert Sprague, and A Mooradian. Design and Characteristics of High-Power (0 . 5-W Surface-Emitting Semiconductor Lasers with Circular TEM Beams. 5(3):561–573, 1999.

R A Lewis. A review of terahertz sources. *Journal of Physics D: Applied Physics*, 47(37):374001, 2014. ISSN 0022-3727. doi: 10.1088/0022-3727/47/37/374001. URL http://stacks.iop.org/0022-3727/47/i=37/a=374001?key=crossref.1e26aa2d9d47555077630d2f1255f62e.

Pierre-Adrien Mante, Cheng-Ying Ho, Li-Wei Tu, and Chi-Kuang Sun. Interferometric detection of extensional modes of GaN nanorods array. *Optics Express*, 20(17):18717, 2012. ISSN 1094-4087. doi: 10.1364/OE.20.018717. URL http://pubs.acs.org/doi/abs/10.1021/nl100798y.

Simon O. Mariager, Dmitry Khakhulin, Henrik T. Lemke, Kasper S. Kjær, Laurent Guerin, Laura Nuccio, Claus B. Sørensen, Martin M. Nielsen, and Robert Feidenhans'L. Direct observation of acoustic oscillations in InAs nanowires. *Nano Letters*, 10:2461–2465, 2010. ISSN 15306984. doi: 10.1021/nl100798y. URL http://pubs.acs.org/doi/abs/10.1021/nl100798y.

Zakaria Mihoubi, Keith G Wilcox, Stephen Elsmere, Adrian Quarterman, Rakchanok Rungsawang, Ian Farrer, Harvey E Beere, David a Ritchie, Anne Tropper, and Vasileios Apostolopoulos. All-semiconductor room-temperature terahertz time domain spectrometer. *Optics letters*, 33(18):2125–2127, 2008. ISSN 0146-9592. doi: 10.1364/OL.33.002125.

P. Muhlschlegel. Resonant Optical Antennas. *Science*, 308(5728):1607–1609, 2005. ISSN 0036-8075. doi: 10.1126/science.1111886. URL http://www.sciencemag.org/cgi/doi/10.1126/science.1111886.

O. L. Muskens, J. Gomez Rivas, V. Giannini, and J. A. Sanchez-Gil. Optical scattering resonances of single plasmonic nanoantennas. 15(26):17736–17746, 2006. ISSN 1094-4087. doi: 10.1364/OE.15.017736. URL http://arxiv.org/abs/cond-mat/0612689{%}0Ahttp://dx.doi.org/10.1364/OE.15.017736.

Otto L. Muskens, Silke L. Diedenhofen, Maarten H M Van Weert, Magnus T. Borgström, Erik P a M Bakkers, and Jaime Gómez Rivas. Epitaxial growth of aligned semiconductor nanowire metamaterials for photonic applications. *Advanced Functional Materials*, 18(7):1039–1046, 2008. ISSN 1616301X. doi: 10.1002/adfm.200701337.

Otto L. Muskens, Silke L. Diedenhofen, Bernard C. Kaas, Rienk E. Algra, E. P a M Bakkers, J. G. Rivas, and Ad Lagendijk. Large Photonic Strength of Highly Tunable Resonant Nanowire Materials. *Nano Letters*, 9(3):930–934, 2009. ISSN 15306984. doi: 10.1021/nl802580r.

Chang-Yong Nam, Papot Jaroenapibal, Douglas Tham, David E Luzzi, Stephane Evoy, and John E Fischer. Diameter-dependent electromechanical properties of GaN nanowires. *Nano letters*, 6(2):153–158, 2006. ISSN 1530-6984. doi: 10.1021/nl051860m.

Kevin O'Brien, N D Lanzillotti-Kimura, Junsuk Rho, Haim Suchowski, Xiaobo Yin, and Xiang Zhang. Ultrafast acousto-plasmonic control and sensing in complex nanostructures. *Nature communications*, 5(May):4042, 2014. ISSN 2041-1723. doi: 10.1038/ncomms5042. URL http://www.ncbi.nlm.nih.gov/pubmed/24893773.

Matthew Pelton, John E Sader, Julien Burgin, Mingzhao Liu, Philippe Guyot-Sionnest, and David Gosztola. Damping of acoustic vibrations in gold nanoparticles. *Nature nanotechnology*, 4(8):492–5, aug 2009. ISSN 1748-3395. doi: 10.1038/nnano.2009.192. URL http://www.ncbi.nlm.nih.gov/pubmed/19662009.

Stephen E. Ralph and D. Grischkowsky. Trap-enhanced fields in semi-insulators: The role of electrical and optical carrier injection. *Appl. Phys. Lett.*, 59(16):1972–1974, 1991.

Hamed Sadeghian, Chung-Kai Yang, Khashayar Babaei Gavan, Johannes F L Goosen, Emile W J M van der Drift, Herre S J van der Zant, Andre Bossche, Paddy J French, and Fred van Keulen. Some considerations of effects-induced errors in resonant cantilevers with the laser deflection method. *Journal of Micromechanics and Microengineering*, 20(10):105027, 2010. ISSN 0960-1317. doi: 10.1088/0960-1317/20/10/105027. URL http://www.scopus.com/inward/record.url?eid=2-s2.0-78049397775{&}partnerID=tZOtx3y1.

M. Scheller, T.-L. Wang, B. Kunert, W. Stolz, S.W. Koch, and J.V. Moloney. Passively modelocked VECSEL emitting 682 fs pulses with 5.1 W of average output power. *Electronics Letters*, 48(10):588, 2012. ISSN 00135194. doi: 10.1049/el.2012.0749. URL http://ieeexplore.ieee.org/stamp/stamp.jsp?arnumber=6198537.

O. D. Sieber, V. J. Wittwer, M. Mangold, M. Hoffmann, T. Südmeyer, and U. Keller. Femtosecond VECSEL with tunable multi-gigahertz repetition rate. 19 (23):23538–23543, 2011. URL http://www.opticsinfobase.org/oe/fulltext.cfm?uri=oe-19-23-23538{&}id=224142.

G Steinmeyer, Dh Sutter, L Gallmann, N Matuschek, and U Keller. Frontiers in Ultrashort Pulse Generation: Pushing the Limits in Linear and Nonlinear Optics. *Science (New York, N.Y.)*, 286(November):1507–1512, 1999. ISSN 1095-9203. doi: 10.1126/science.286.5444.1507. URL http://www.ncbi.nlm.nih.gov/pubmed/10567248.

B. Stiller. *Thèse de Doctorat Birgit Stiller Brillouin scattering in photonic crystal fiber : from fundamentals to fiber optic sensors.* PhD thesis, Universit e de Franche-Comt, 2011. URL http://tel.archives-ouvertes.fr/docs/00/69/06/40/PDF/ThesisBirgitStiller.pdf.

Xiankai Sun, Xufeng Zhang, and Hong X. Tang. High-Q silicon optomechanical microdisk resonators at gigahertz frequencies. *Applied Physics Letters*, 100(17), 2012. ISSN 00036951. doi: 10.1063/1.4709416.

Takehiro Tachizaki, Osamu Matsuda, Alex a. Maznev, and Oliver B. Wright. Acoustic whispering-gallery modes generated and dynamically imaged with ultrashort optical pulses. *Physical Review B*, 81(16):165434, apr 2010. ISSN 1098-0121. doi: 10.1103/PhysRevB.81.165434. URL http://link.aps.org/doi/10.1103/PhysRevB.81.165434.

Masahiko Tani, Shuji Matsuura, Kiyomi Sakai, and Shin-ichi Nakashima. Emission characteristics of photoconductive antennas based on low-temperature-grown GaAs and semi-insulating GaAs. *Applied Optics*, 36(30):7853, 1997. ISSN 0003-6935. doi: 10.1364/AO.36.007853. URL https://www.osapublishing.org/abstract.cfm?URI=ao-36-30-7853.

Andrew P. Turnbull. *Design and Characterisation of Ultrafast Semiconductor Disk Lasers*. PhD thesis, University of Southampton, 2015. URL https://uk.sitestat.com/bl/ethos/s?clickout.ethos.UniversityofSouthampton.667509{&}ns{_}type=clickout{&}bl{_}ethosid=667509{&}ns{_}url=http://eprints.soton.ac.uk/381283/.

D. Waldburger, C. G. E. Alfieri, S. M. Link, E. Gini, M. Golling, M. Mangold, B. W. Tilma, and U. Keller. Pulse shortening of an ultrafast VECSEL. *Spie Lase*, 9734: 973409, 2016. ISSN 1996756X. doi: 10.1117/12.2209251. URL http://proceedings.spiedigitallibrary.org/proceeding.aspx?doi=10.1117/12.2209251.

Jean-Claude Weeber, Alain Dereux, Christian Girard, Joachim R. Krenn, and Jean-Pierre Goudonnet. Plasmon polaritons of metallic nanowires for controlling submicron propagation of light. *Physical Review B*, 60(12):9061–9068, 1999. ISSN 0163-1829. doi: 10.1103/PhysRevB.60.9061. URL http://link.aps.org/doi/10.1103/PhysRevB.60.9061.

G S Wiederhecker, a Brenn, H L Fragnito, and P St J Russell. Coherent control of ultrahigh-frequency acoustic resonances in photonic crystal fibers. *Physical review letters*, 100(20):203903, may 2008. ISSN 0031-9007. doi: 10.1103/PhysRevLett.100.203903. URL http://link.aps.org/doi/10.1103/PhysRevLett.100.203903.

K. G. Wilcox and A. H. Quarterman. Variable repetition frequency femtosecond-pulse surface emitting semiconductor laser. *Applied Physics ...*, 99(13):131107, 2011. ISSN 00036951. doi: 10.1063/1.3644162. URL http://scitation.aip.org/content/aip/journal/apl/99/13/10.1063/1.3644162.

Keith G Wilcox, Adrian H Quarterman, Harvey E Beere, David A Ritchie, and Anne C Tropper. Repetition-frequency-tunable mode-locked surface emitting semiconductor laser between 2.78 and 7.87 GHz. 19(23):23453–23459, 2011. URL http://eprints.soton.ac.uk/339031/.

Rafał Wilk, Thomas Hochrein, Martin Koch, Michael Mei, and Ronald Holzwarth. OSCAT: Novel technique for time-resolved experiments without moveable optical delay lines. *Journal of Infrared, Millimeter, and Terahertz Waves*, 32(5):596–602, 2011. ISSN 18666892. doi: 10.1007/s10762-010-9670-8.

E. W. Wong. Nanobeam Mechanics: Elasticity, Strength, and Toughness of Nanorods and Nanotubes. *Science*, 277(5334):1971–1975, 1997. ISSN 00368075. doi: 10.1126/science.277.5334.1971. URL http://www.sciencemag.org/cgi/doi/10.1126/science.277.5334.1971.